

Modeling and Linearization of MIMO RF Transmitters

Sara Hesami



Department of Electronic Engineering
Maynooth University
Ireland

Supervisors of the Research: John Dooley, Ronan Farrell

Head of the Department: Ronan Farrell

This dissertation is submitted for the degree of
Doctor of Philosophy

I would like to dedicate this thesis to the ones who motivated me through my life
and my research.

Declaration

I have read and understood the Departmental policy on plagiarism.

I declare that this thesis is my own work and has not been submitted in any form for another degree or diploma at any university or other institution of tertiary education.

Information derived from the published or unpublished work of others has been acknowledged in the text and a list of references is given.

Signed:

Sara Hesami

Sara Hesami
September 2020

Abstract

Multiple-input multiple-output (MIMO) technology will continue to play a vital role in next-generation wireless systems, e.g., the fifth-generation wireless networks (5G). Large-scale antenna arrays (also called massive MIMO) seem to be the most promising physical layer solution for meeting the ever-growing demand for high spectral efficiency. Large-scale MIMO arrays are typically deployed with high integration and using low-cost components. Hence, they are prone to different hardware impairments such as crosstalk between the transmit antennas and power amplifier (PA) nonlinearities, which distort the transmitted signal. To avert the performance degradation due to these impairments, it is essential to have mechanisms for predicting the output of the MIMO arrays. Such prediction mechanisms are mandatory for performance evaluation and, more importantly, for the adoption of proper compensation techniques such as digital predistortion (DPD) schemes. This has stirred a considerable amount of interest among researchers to develop new hardware and signal processing solutions to address the requirements of large-scale MIMO systems.

In the context of MIMO systems, one particular problem is that the hardware cost and complexity scale up with the increase of the size of the MIMO system. As a result, the MIMO systems tend to be implemented on a chip and are very compact. Reduction of the cost by reducing the bill of material is possible when several components are eliminated. The reuse of already existing hardware is an alternative solution. As a result, such systems are prone to excessive sources of distortion, such as crosstalk. Accordingly, crosstalk in MIMO systems in its simplest form can affect the DPD coefficient estimation scheme. In this thesis, the effect of

crosstalk on two main DPD estimation techniques, known as direct learning algorithm (DLA) and indirect learning algorithm (ILA), is studied.

The PA behavioral modeling and DPD scheme face several challenges that seek cost-efficient and flexible solutions too. These techniques require constant capture of the PA output feedback signal, which ultimately requires the implementation of a complete transmitter observation receiver (TOR) chain for the individual transmit path. In this thesis, a technique to reuse the receiver path of the MIMO TDD transceiver as a TOR is developed, which is based on over-the-air (OTA) measurements. With these techniques, individual PA behavioral modeling and DPD can be done by utilizing a few receivers of the MIMO TDD system. To use OTA measurements, an on-site antenna calibration scheme is developed to individually estimate the coupling between the transmitter and the receiver antennas.

Furthermore, a digital predistortion technique for compensating the nonlinearity of several PAs in phased arrays is presented. The phased array can be a subset of massive MIMO systems, and it uses several antennas to steer the transmitted signal in a particular direction by appropriately assigning the magnitude and the phase of the transmitted signal from each antenna. The particular structure of phased arrays requires the linearization of several PAs with a single DPD. By increasing the number of RF branches and consequently increasing the number of PAs in the phased array, the linearization task becomes challenging. The DPD must be optimized to result in the best overall linear performance of the phased array in the field. The problem of optimized DPD for phased array has not been addressed appropriately in the literature.

In this thesis, a DPD technique is developed based on an optimization problem to address the linearization of PAs with high variations. The technique continuously optimizes the DPD coefficients through several iterations considering the effect of each PA simultaneously. Therefore, it results in the best optimized DPD performance for several PAs.

Extensive analysis, simulations, and measurement evaluation is carried out as a proof of concept. The different proposed techniques are compared with conven-

tional approaches, and the results are presented. The techniques proposed in this thesis enable cost-efficient and flexible signal processing approaches to facilitate the development of future wireless communication systems.

Acknowledgements

I want to express my gratitude to everyone who has supported me for my graduate studies. First, I would like to thank my team of supervisors at Maynooth University. Dr. John Dooley, thank you for your encouragement and optimism in the hard times of my research. Prof. Ronan Farrell, thank you for your constant support throughout my work. I would also like to express my gratitude toward Prof. Tomas Eriksson and Prof. Christian Fager at the Chalmers University of Technology for believing in me and for their unfailing support and guidance.

I would like to thank colleagues and friends for their contribution and support, Dr. Prasidh Ramabadran, Pavel Afanasyev, Dr. Sina Rezaei Aghdam, Dr. Katharina Hausmair, and Dr. John Conlan.

Last, but by no means least, I would like to extend my warmest thanks to all my family members who have motivated me throughout my graduate studies and research.

Table of contents

List of figures	xvii
List of tables	xxiii
1 Introduction	1
1.1 Major Contributions	5
1.2 Thesis Outline	6
1.3 Publications record	7
1.3.1 Peer-Reviewed Journal Papers	7
1.3.2 Papers in Refereed Conference Proceedings	7
2 Background	9
2.1 Power Amplifier Efficiency	12
2.2 Power Amplifier Linearity	13
2.3 Power Amplifier Operational Bandwidth	14
2.4 Power Amplifier Dynamic Range	15
2.5 Power Amplifier Classes	16
2.5.1 Continuous Mode Amplifiers	16
2.5.2 Switched Mode Amplifiers	17
2.5.3 Advanced Designs of Amplifiers	18
2.6 Figures of Merit	18
2.6.1 Power Amplifier Nonlinearity and Distortion	21
2.7 Amplifier Behavioral Modeling	24

Table of contents

2.7.1	Memory Polynomial Model	26
2.7.2	Model Identification	27
2.7.3	Model Accuracy Evaluation	27
2.8	Digital Predistortion	28
2.8.1	DPD Model and Identification Techniques	29
2.8.1.1	Indirect Learning Technique	30
2.8.1.2	Direct Learning Technique	31
2.8.2	DPD Performance Evaluation	32
3	MIMO Transmitters- Introduction and Review	35
3.1	MIMO System and Phased Array Challenges	36
3.2	MIMO TDD System Models	40
3.2.1	Intra-Array System Models Without Crosstalk	41
3.2.2	Intra-Array System Models With Crosstalk	42
3.3	Phased Array System Models	45
3.4	Contributions	48
4	Digital Predistortion Training for Systems with Antenna Crosstalk	51
4.1	MIMO System Models With Antenna Crosstalk	52
4.2	PA Behavioral Modeling and DPD with Antenna Crosstalk	54
4.2.1	DPD Learning Algorithm with Antenna Crosstalk	55
4.3	A Comparative Study of DLA and ILA with Antenna Crosstalk	56
4.4	Conclusion	59
5	Intra Array Coupling Estimation	61
5.1	Proposed Effective Coupling Estimation	62
5.1.1	Single Estimation	65
5.1.1.1	Reference Coupling Estimation	65
5.1.1.2	Intra-Array Coupling Estimation	66
5.1.2	Joint Estimation	67
5.1.2.1	Joint Reference Coupling Estimation	68

5.1.2.2	Intra-Array Coupling Estimation	68
5.1.3	Clustering	70
5.1.4	Complexity Analysis	72
5.1.5	Performance Assessment	72
5.1.5.1	Simulation Setup for the Effective Coupling Estima- tion and Results	73
5.2	Experimental Validation	74
5.2.1	Measurement Setup for Effective Coupling Estimation	75
5.3	Results	77
5.3.1	Evaluation of Coupling Estimation	78
5.3.2	Impact of Different Transmitter Configurations on Coupling Estimation	79
5.3.3	Impact of Receiver Characteristic Dissimilarity on Coupling Estimation	81
5.4	Conclusion	83
6	OTA-based MIMO Transceiver Linearization	85
6.1	PA Modeling and Identification for OTA-MIMO Systems	87
6.2	Performance Assessment	92
6.2.1	Simulation Setup for PA Modeling	93
6.3	Predistortion	93
6.4	Experimental Validation	94
6.4.1	Measurement Setup for PA modeling and DPD technique using OTA Measurements	95
6.5	Results	97
6.5.1	Evaluation of PA model identification with OTA measurements	97
6.5.2	Evaluation of Dual-Input DPD with OTA measurements . . .	101
6.6	Conclusion	102
7	Digital Predistortion for Phased Arrays	111
7.1	Single DPD System Model	113

Table of contents

7.2	Beamforming DPD with MinMax	116
7.3	Simulation Results	118
7.4	Measurement Results Under PA Amplitude Variations	121
7.4.1	Measurement Setup	122
7.4.2	Measurement Results	124
7.5	Conclusion	125
8	Conclusion	127
8.1	Conclusions	127
8.2	Future Work	130
Appendix A Matrix Representation of Ψ for Effective Coupling Single Estimation		133
Appendix B Matrix Representation of Ψ for Effective Coupling Joint Estimation		135
References		137

List of figures

2.1	Block diagram of an RF wireless system.	10
2.2	A typical power amplifier response.	11
2.3	Illustration of 1 dB compression point and dynamic range of a power amplifier.	15
2.4	Graphical representation of error vector magnitude.	18
2.5	Graphical representation of ACPR.	20
2.6	Sample AM/AM characteristic of a power amplifier.	21
2.7	Sample AM/PM characteristic of a power amplifier.	22
2.8	Layout of a power amplifier with the matching networks.	23
2.9	Digital predistortion operation principle.	29
2.10	Block diagram of an RF transmitter with DPD based on ILA.	30
2.11	Block diagram of an RF transmitter with DPD based on DLA.	31
3.1	A general power amplifier response.	36
3.2	Block diagram of a MIMO system with K transceivers with one transceiver in transmit mode while the rest of the array elements are receiving.	41
3.3	Block diagram of a MIMO system with K transceivers with one transceiver in transmit mode while the rest of the array elements are receiving in presence of crosstalk.	43
3.4	Block diagram of a phased array.	47
4.1	Antenna crosstalk in MIMO transmitter.	54

List of figures

4.2	MIMO transmitter and DPD block diagram in presence of antenna crosstalk.	56
4.3	PA output spectrum when no linearization was applied, PA output with linearization in presence of no crosstalk and -6 dB crosstalk. . .	57
4.4	Coefficients Divergence in DLA and ILA in presence of no crosstalk, -10 dB antenna crosstalk and -6 dB antenna crosstalk.	58
5.1	Block diagram of a MIMO system with K transceivers with one transceiver in transmit mode while the rest of the array elements are receiving in presence of crosstalk.	63
5.2	Identifying the reference coupling based on the reference transceiver position within the array. The gray circle indicates the reference antenna.	68
5.3	Clustering technique. Two clusters are identified where each cluster contains four antenna elements. The broken blue line indicates the active cluster. The gray circle indicates the reference (R) antenna in the first cluster. The green circle indicates the common transmitter (CT).	71
5.4	The layout of the 4×4 array is given in (a), the dimensions of a single patch antenna are given in (b).	73
5.5	NMSE of the estimated $\lambda_{i,j}$ versus SNR in a 4×4 array.	74
5.6	Antenna array measured S-parameters versus frequency for antenna 1. The S-parameters for rest of the array are similar for self reflection (S11), adjacent element reflection (S14), opposite element reflection (S12) and diagonal reflection (S13).	75
5.7	Block diagram of experimental measurement setup for OTA coupling estimation when antenna 4 acts as a common transmitter.	76
5.8	Experimental measurement setup for OTA linearization of the MIMO system.	77

5.9	Magnitude (dB) and Phase (degree) of the coupling coefficients corresponding to <i>Single Estimation</i> , <i>Joint Estimation</i> and S-parameters. . .	78
5.10	Magnitude (dB) and Phase (degree) of the coupling coefficients corresponding to different transmitter configurations.	80
5.11	NMSE of estimated couplings vs. SNR for different levels of receiver similarities.	81
5.12	Magnitude (dB) and Phase (degree) of the coupling coefficients to <i>Direct Measurement 1</i> and <i>Direct Measurement 2</i>	83
6.1	Block diagram of a MIMO system with K transceivers with one transceiver in receive mode while the rest of the array elements are transmitting in presence of crosstalk.	87
6.2	The layout of the 4×4 array is given in (a), the dimensions of a single patch antenna are given in (b).	91
6.3	NMSE of estimated PA models per iteration of Algorithm 1	92
6.4	Block diagram of experimental measurement setup for DPD implementation with OTA measurements. Antenna 1 and 2 are in receive mode and antenna 3 and 4 are in transmit mode.	95
6.5	Experimental measurement setup for OTA linearization of the MIMO system.	96
6.6	Spectra of received signals at Rx1 and Rx2 from measurement (Meas), simulation (Sim), and the spectra of error (Err) in simulation, when the couplings between the antenna elements are replaced by single frequency S-parameters.	104
6.7	Spectra of received signals at Rx1 and Rx2 from measurement (Meas), simulation (Sim), and the spectra of error (Err) in simulation, when the couplings between the antenna elements are replaced by estimated couplings.	105

List of figures

6.8	Spectra of measured PA outputs (Meas) from couplers coupled line, and the simulated PA outputs (Sim). The error spectra (Err) shows the error in simulation when the couplings between the antenna elements are replaced by single frequency S-parameters.	106
6.9	Spectra of measured PA outputs (Meas) from couplers coupled line, and the simulated PA outputs (Sim). The error spectra (Err) shows the error in simulation when the couplings between the antenna elements are replaced by estimated couplings.	107
6.10	Spectra of the linearized PAs. The figure shows the results without DPD, with the single frequency S-parameters DPD (SP DPD) and with the estimated coupling technique DPD (EC DPD).	108
6.11	Spectra of the linearized received signals. The figure shows the results without DPD, with the single frequency S-parameters DPD (SP DPD) and with the estimated coupling technique DPD (EC DPD).	109
7.1	Block diagram of a phased array.	113
7.2	Block diagram of a sub-array to access each PA units output with shared feedback.	115
7.3	Spectra of the combined array response in the far-field for different DPD methods with PA model of 3rd order polynomial.	119
7.4	Spectra of the combined array response in the far-field for different DPD methods with PA model of 5th order polynomial.	120
7.5	AM/AM plots for combined array far-field responses without DPD and with three different DPD methods with 3rd order PA models. . .	121
7.6	PA input power weights of a 8-element uniform linear array to achieve SLL = -13.4 dBc, -15 dBc, -20 dBc and -30 dBc. The simulated power distributions are presented in blue and the actual power distribution in measurement test bench are presented in red.	122
7.7	Photograph of the test setup.	123

7.8 Channel power and ACP of combined feedback (Comb DPD), joint optimization (MinMax DPD), and sum of the errors (SumErr DPD) for: (a) uniform power distribution, (b) SLL = -15 dBc, (c) SLL = -20 dBc, (d) SLL = -30 dBc. 125

List of tables

4.1	NMSE [dB] for different antenna crosstalk in a 2×2 MIMO transmitter using DLA and ILA techniques.	58
6.1	ACLR and NMSE for Different Coupling Coefficients for OTA DPD Technique	100
7.1	ACLR (dB) evaluation of three different DPD methods for different PA models.	118

Notations and Abbreviations

Throughout the thesis, matrices, vectors and scalar quantities are denoted by boldface uppercase, boldface lowercase and normal letters, respectively.

Notations

j	Unit imaginary number $\sqrt{-1}$
$[\mathbf{A}]^{m \times n}$	The element in the m^{th} row and n^{th} column of matrix \mathbf{A}
\mathbf{A}^{-1}	The inverse of matrix \mathbf{A}
$(\cdot)^{\text{T}}$	Transpose of a matrix
$(\cdot)^{\text{H}}$	Conjugate transpose of a matrix
$(\cdot)^*$	Conjugate
$ \cdot $	Absolute value operator
$\ \cdot\ $	Norm operator

Acronyms / Abbreviations

3GPP	3rd Generation Partnership Project
5G	Fifth generation of wireless communication systems
ACEPR	Adjacent Channel Error Power Ratio
ACLR	Adjacent Channel Leakage Ratio

Notations and Abbreviations

ACP	Adjacent Channel Power
ACPR	Adjacent Channel Power Ratio
ADC	Analog-to-Digital Converter
AGC	Automatic Gain Control
AM/AM	Amplitude-to-Amplitude
AM/PM	Amplitude-to-Phase
BER	Bit Error Rate
CT	Common Transmitter
CTMM	Crosstalk and Mismatch Model
DAC	Digital-to-Analog Converter
dB	Decibels
DC	Direct Current
DE	Drain Efficiency
DLA	Direct Learning Algorithm
DL	Downlink
DPD	Digital Predistortion
EVM	Error Vector Magnitude
FDD	Frequency-Division Duplex
FPGA	Field-Programmable Gate
GHz	Gigahertz
GMP	Generalized Memory Polynomial

GMPLC	Generalized Memory Polynomial for linear crosstalk
IBW	Integration Bandwidth
IF	Intermediate Frequency
I	In-phase
ILA	Indirect Learning Algorithm
L	Lower
LNA	Low-Noise Amplifier
LO	Local Oscillator
LS	Least Square
LTE)	Long Term Evolution
LTE	Long Term Evolution
MF	Match Filter
MHz	Megahertz
MILA	Model-based Indirect Learning Algorithm
MIMO	Multiple Input Multiple Output
MPLC	Memory Polynomial for linear crosstalk
MP	Memory Polynomial
MRF	Maximum Ratio Transmission
NMSE	Normalized Mean Square Error
OFDM	Orthogonal Frequency Division Multiplexing
OTA	Over The Air

Notations and Abbreviations

PAE)	Power Added Efficiency
PA	Power Amplifier
PAPR	Peak to Average Power Ratio
QAM	Quadrature Amplitude Modulation
Q	Quadrature-phase
RBS	Radio Base Station
RF	Radio Frequency
Rx	Receiver
RZF	Regularized Zero Forcing
SISO	Single-Input Single-Output
SNR	Signal-to-Noise Ratio
TDD	Time Division Duplex
TOR	Transmitter Observation Receiver
TRx	Transceiver
Tx	Transmitter
UE	User Equipment
ULA	Uniform Linear Array
U	Upper
VNA	Vector Network Analyzer
WCDMA	Wide Code Division Multiple Access
ZF	Zero Forcing

Chapter 1

Introduction

Today's modern society has become highly reliant upon the development of wireless communication systems to facilitate different forms of communication and encourage different applications of these systems. As a result, it is easy to envision the emergence of an ever-growing demand for higher data rates and the need for increased capacity of wireless communication systems. Therefore, a more efficient use of the limited spectrum is necessary [1]. High-order digital modulation schemes such as quadrature amplitude modulation (QAM) allows a higher number of bits to be transmitted for each modulation symbol and increases the spectral efficiency. In wideband digital communication, the encoding technique of orthogonal frequency division multiplexing (OFDM) utilizes several orthogonal overlapping carrier frequencies, thereby improving the limited spectrum resource at the cost of increased the peak rate. Other advanced wireless communication techniques to improve the spectral efficiency are wideband code division multiple access (WCDMA) and long term evolution (LTE) standard with envelope varying signals. The signals in these techniques are characterized by not only wide bandwidth but also a large peak-to-average power ratio (PAPR). The modern communication signals with high PAPR are more susceptible to distortion due to the transmitter imperfection.

Other approaches to improve the efficiency of wireless networks are made as, deploying small cells, increased spectrum and increased spectral efficiency. Improve

Introduction

of spectral efficiency means conveying more bits of information per units of frequency band in a second. The use of multiple-input multiple-output (MIMO) systems have emerged as the most favorable physical-layer solution for achieving high data rates, connection reliability, and high spectral efficiency in 5G and beyond communication systems [2]. The directive beam pattern achieved by deploying an array of antenna in MIMO systems, allow for use of millimeter wave (mm-Wave) bands. Different categories of MIMO systems are: point-to-point MIMO, multiuser MIMO, massive MIMO. The point-to point MIMO consists of a radio base station with an antenna array and a user equipment with an antenna array. In this scheme, only the receiver must acquire the channel state information (CSI). In point-to-pint MIMO, the link spectral efficiency can be improved by utilizing large arrays as transmitter and receiver. Nonetheless, this scheme is limited by the increasing hardware complexity of the transmitters. Each antenna must be equipped with a separate RF chain. Furthermore, complex signal processing techniques must be employ to separate different data streams. Another limitation of point-to-point MIMO is due to the propagation environment which must support number of data streams as large as the number of antennas. This is particularly difficult for higher frequencies where the antenna arrays become more compact. furthermore, at the edge of the cells, the improvement of spectral efficiency is somewhat limited as the signal-to-noise ratio (SNR) is low [3].

The idea of multiuser MIMO is developed, simply, by splitting the users antenna array into several separate user equipment. In its conventional form the users have a single antennas. As a result, the user hardware is less complex. Unlike, pint-to-point MIMO, the multiuser MIMO requires the knowledge of CSI for bot transmitter and the receiver. On the contrary, the multiuser MIMO is less sensitive to the propagation conditions compared to the point-to-point MIMO. However, the multiuser MIMO system requires complex signal processing resources at both transmitter and the receiver [3].

Massive MIMO is a scalable version of multiuser MIMO transmitter with some distinctions. In massive MIMO, only the base station knows the CSI and, typically,

the number of antennas at the base station is much larger than the number of user antennas. Moreover, only a simple linear signal processing is used both the the transmitter and the receiver. The base station aims to create a narrow beam for each user terminals, under line-of-sight (LoS) propagation assumption. By increasing the number of the antennas the beam becomes narrower and the power is concentrated at one point. As a result the CSI must be known accurately by the base station. In time-division-duplex (TDD) mode, the base station exploits the reciprocity of the channel and receive the pilots transmitted by the users to estimate the CSI. This makes TDD an attractive option for massive MIMO implementation.

The MIMO communication system requires a transceiver (TRx) employing several independent RF chains to stimulate an antenna array; for individual RF transmitters, each contains a power amplifier (PA) that drives a distinct antenna element. A PA is an indispensable constituent of radio frequency (RF) transmitter. This power-hungry component of the RF transmitter is the most significant source of energy dissipation. To achieve high efficiency, it has been suggested to drive the PAs in their peak power. The nonlinear behavior of the PAs is the most detrimental aspect of the wireless transmitter when signals with high PAPR are transmitted. An amplifier that compresses its input or has a nonlinear input/output relationship causes the output signal to splatter onto adjacent radio frequency bands and introduce interference with neighboring RF equipment [4, 5]. It also causes in-band distortion, which can damage the signal integrity and results in communication failure. The interference and distortion introduced by amplifiers can violated the regulations set by the authorities. Such regulations are set by 3rd Generation Partnership Project (3GPP) and they requirement must be met by the operators [6].

The conventional solution to tackle the nonlinearity is to operate the PA with back-off from the peak power point [7]. The backed-off PA operates in its linear region but compromises the power efficiency. Despite the linearity provided by this approach, the back-off solution is not very attractive as it results in a bulky and inefficient power design of power amplifiers operating with low power signals.

Therefore, there is always a linearity/efficiency trade-off in the PA operation point if no other solution is adopted.

In order to maintain PA power efficiency while reserving the PA linearity, two categories of solutions have been developed. One category focuses on the PA circuit design modification, and the other category focuses on the signal level modification to achieve an overall linear response of the transmitter.

For PA design alternatives exist, such as Doherty PAs that increases the efficiency by load modulation when it combines the output of two or more linear PAs at back-off [8–11], envelope tracking PA by applying amplitude modulation of the drain voltage at linear operation of the PA [12–14], and outphasing PA by converting the amplitude modulated signal into a pair of phase modulated signals with constant amplitudes and feed them to a linear PA or a switched-mode PA [15, 16]. However, these techniques are costly, resulting in bulky PAs, and for wideband signals, the linearity of PAs is not sufficient.

Alternatively, signal processing approaches for linearization became very attractive for their cost and power efficiency and flexibility. In these techniques, PA is operating efficiently near saturation and its nonlinearity is improved by approaches such as feedback [17–19], feed-forward [20–23] and digital predistortion (DPD) [24–29]. Among the proposed linearization techniques, DPD offers higher efficiency and flexibility and an improved degree of linearization while being cost-efficient. It is approximated that the power consumption of the DPD implemented in the field-programmable gate arrays (FPGAs) does not exceed 1 W considering the fact that the DPD is active only when the signal is transmitted [30]. These margins are acceptable considering the fact that the radio base stations (RBSs) are typically consuming 1.5 kW power [31] and that the PA distortion is mitigated by utilizing DPD. Therefore, DPD has become the most popular linearization approach and plays an essential role today and in the next generation of wireless communication systems, i.e., fifth-generation (5G). DPD mechanism incorporates a nonlinear block that predistorts the input signal to the PA in such a manner that the overall performance of the system becomes linear. There are mainly two different structures of DPD,

closed-loop, or direct learning algorithm (DLA) and indirect learning algorithm (ILA) [32]. In both approaches, DPD incorporates a nonlinear dynamic function estimated based on the behavioral model of the PA. Accordingly, PA behavioral modeling is an essential step in the DPD linearization process.

In massive MIMO systems, the physical size and the cost of the transceiver and array scale up as the number of transceiver paths increases. Therefore, simplified hardware is desired, where the removal of hardware components reduces the cost and complexity. Furthermore, to reduce the size of the system, it is favorable to have highly integrated RF transceivers. As a result, such systems are prone to new sources of distortion, such as crosstalk and antenna mismatch. Consequently, new hardware architectures, together with more sophisticated signal processing approaches, must be adopted to address the new challenges and reduce distortion.

1.1 Major Contributions

In this thesis, several novel MIMO system linearization techniques are presented. Implementation of conventional DPD techniques in MIMO systems quickly experiences limitations as the number of parallel paths increase.

Since the implementation of DPD in physical hardware is a complicated technique, the effectiveness of conventional DPD techniques in MIMO systems that suffer from crosstalk is studied. Furthermore, a novel compensation technique is developed by using preexisting MIMO TDD systems with reduced hardware complexity. The technique is based on the over-the-air (OTA) measurement technique, which reuses few transceivers in a MIMO TDD system as an OTA receiver. To enable the OTA based MIMO DPD, the channels between the transmitter and the receiver antennas must be identified. Failure to estimate the channels results in linearization, which is only valid at the position of the receiver antennas.

In this thesis, we developed a technique where the channels between antenna elements in an array are identified in a TDD MIMO system via consecutive intra-array transmission. Furthermore, we enable modeling and linearization of individual

PAs in a MIMO transmitter by utilizing the estimated channels. We follow a model-based linearization approach where, through a few iterations, the PA models can be identified and used to perform the linearization. Measurement results are provided to experimentally validate the proposed channel estimation and linearization of the MIMO system with OTA measurements.

Hybrid beamforming as an inevitable part of future massive MIMO implementation added more challenges in the linearization of MIMO systems. In this thesis, we looked at state of the art in phased array linearization. Such systems require the linearization of several PAs with only a few DPDs. When the PA behaviors are similar, the linearization can be performed by considering an average nonlinear model of the array. However, the technical gap in the linearization of large phased-arrays is manifested when the PA behaviors across the array are diverse.

In this thesis, state of the art in phased array linearization has been explored and examined. We introduced a novel DPD technique for phased arrays based on an optimization technique. The results show that the proposed technique is superior to those of existing techniques when the PAs Characteristics across the array are divers.

1.2 Thesis Outline

The remainder of this thesis is organized as follows: Chapter 2 serves as an introduction to PA RF distortion and linearization. The chapter begins with RF transmitter basic building blocks. Then, different sources of distortions due to hardware imperfection, mainly in RF PAs, are discussed. In this regard, alternative PA classes are introduced, and their efficiency and linearity are explained. Conventional PA behavioral modeling and DPD as a linearization technique are explained. Chapter 3 describes the challenges in MIMO transceivers, including the increased complexity of the linearization technique in large MIMO systems. A literature review present preexisting alternative solutions to reduce the complexity of DPD systems are visited to give a clear view of the contribution of the work proposed in this thesis. Chapter 4 is dedicated to the study of two different DPD learning algorithms when the MIMO

system suffers from antenna crosstalk while the isolators protect the DPD output. In Chapter 5, a framework for intra-array coupling estimation, is introduced to enable the OTA linearization with reduced hardware complexity. The proposed coupling estimation technique is used in Chapter 6 to develop a PA modeling technique with OTA measurements. This technique provides individual PA model identification, which enables linearization per transmit branch. In Chapter 7, the linearization problem in phased arrays is visited as a sub-block of hybrid MIMO systems. A new technique is presented to improve the linearization of several PAs in phased arrays by incorporating only one DPD, where the PA behaviors can vary drastically across the array. Finally, Chapter 8 concludes the work by giving a summary of the contributions of this thesis and provides possible avenue for future works.

1.3 Publications record

The following publications relate directly to this thesis:

1.3.1 Peer-Reviewed Journal Papers

1. S. Hesami, P. Ramabadran, S. Rezaei Aghdam, K. Hausmair, C. Fager, T. Eriksson, R. Farrell, J. Dooley, “OTA-based MIMO Transceiver Modeling and Linearization using Effective Coupling Estimation,” *Submitted to IEEE Transaction on Microwave Theory and Techniques*, March 2020

1.3.2 Papers in Refereed Conference Proceedings

1. S. Hesami, S. Rezaei Aghdam, J. Dooley, T. Eriksson, C. Fager “Amplitude Varying Phased Array Linearization,” *European Microwave Conference, Jaarbeurs Utrecht, Netherlands*, 2020
2. S. Hesami, S. Rezaei Aghdam, C. Fager, T. Eriksson, R. Farrell, J. Dooley, “Intra-Array Coupling Estimation for MIMO Transceivers Utilizing Blind Over-

Introduction

- The-Air Measurements,” *IEEE MTT International Microwave Symposium*, Boston, MA, USA, 2019
3. S. Hesami, S. Rezaei Aghdam, C. Fager, T. Eriksson, R. Farrell, J. Dooley, “Single Digital Predistortion Technique for Phased Array Linearization,” *IEEE International Symposium on circuits and Systems*, Sapporo, Japan, 2019
 4. S. Hesami, Z. Wang, J. Dooley, R. Farrell, “Digital predistorter in crosstalk compensation of MIMO transmitters,” *Irish Signals and Systems Conference*, Londonderry, UK, 2016

Chapter 2

Background

Wireless radios are an essential part of the wireless communication systems. Fig. 2.1 shows a general wireless radio system. The main building blocks of the wireless radio system are the transmitter, the receiver, and the channel between the transmitter and the receiver that the transmitted signal experience it by traveling through the air.

The receiver building blocks are as follows:

- The main receiver's sub-blocks starts with the antenna that receives the transmitted signal.
- A band-selective filter is implemented to reject signals at unwanted frequencies in adjacent channels and harmonics.
- The filtered signal goes through a low-noise amplifier (LNA) to amplify the received signal with very low power and maintain the signal-to-noise ratio (SNR) for demodulation.
- The amplified signal, which is still at RF frequency, then goes through a mixer, which brings the signal of interest into a fixed intermediate frequency (IF).
- The next component, which is the demodulator, can be optimized to operate at the fixed frequency independent of the RF frequency that the signal is captured at.

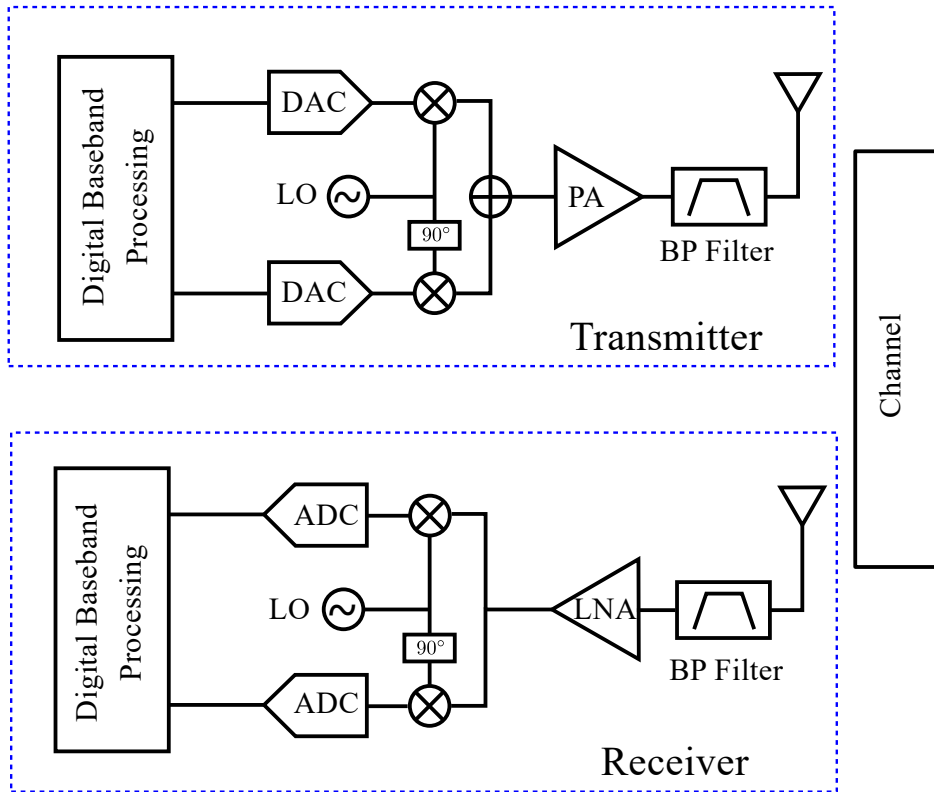


Fig. 2.1 Block diagram of an RF wireless system.

- By mixing the signal with the local oscillator (LO) provided frequency, the RF signal can be split into in-phase (I) and quadrature-phase (Q) baseband signals. In this step, the signal is sampled by an analog-to-digital converter (ADC). In the final stage, the signal goes through the baseband processing for detection.

The transmitter building blocks are in the reverse order compared to the receiver chain.

- The main sub-blocks of the transmitter start with baseband processing.
- Afterward, the signal goes through the digital-to-analog converter (DAC).
- Next, the modulator combines the I and Q data by an up-converter, which is tuned at the carrier frequency (f_c). The up-converter again performed by mixers, which are fed by LO at the carrier frequency. The signal to be transmitted must meet the requirements in terms of its power level to be qualified for

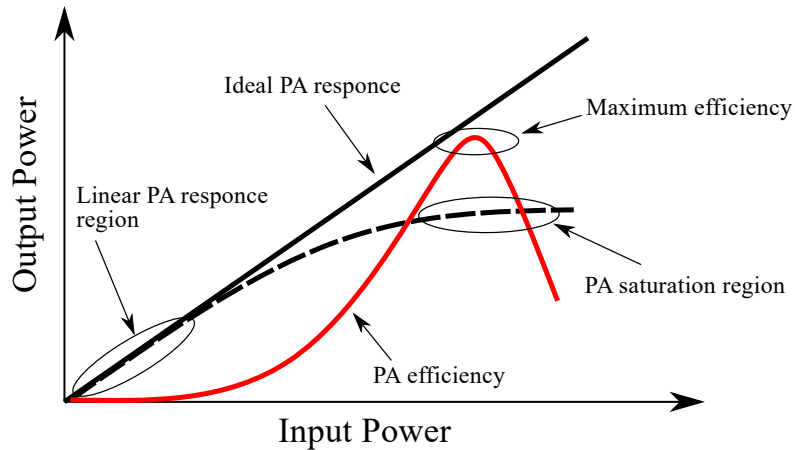


Fig. 2.2 A general power amplifier response.

transmission through the air. This is due to the inherent properties of the medium in which the signal is transmitted through it, such as air. The inherent property of radio waves results in the expansion of the wave in the space. As a result, the transmitted signal will be attenuated and cannot reach the receiver antenna, which is typically placed in the far-field of the transmitting antennas. This phenomenon is called propagation loss.

- In the next step, the signal will be amplified by passing through the power amplifiers operating at RF frequency. The signal will be amplified up to a certain level, which is specified by regulations.
- The amplified signal is filtered.
- Finally the filtered signal is fed to the transmitting antenna.

The transmitters regularly introduce distortions that, if not mitigated correctly, can violate spectrum regulations. Power amplifiers are a major source of distortions and are the most power-hungry component of the transmitters. In order to increase the efficiency of the amplifiers, it is desired to operate the amplifiers close to saturation [33], where the amplifier behavior is nonlinear. A general amplifier response is shown in Fig.2.2 . As can be seen, the maximum efficiency is achieved at the highest nonlinear response of the power amplifier. As a result, the response of the power

amplifier can introduce intermodulation distortion [5]. The signal integrity can be affected as a result of passing the signal through a nonlinear power amplifier.

This is due to the inherent nonlinearity of the power amplifiers, which can result in inband and out-of-band distortion. Therefore, there is a trade-off between power amplifier linearity and efficiency. In order to analyze a power amplifier, the linearity and efficiency of the amplifier are evaluated. Other factors which are contributing to the performance of power amplifiers are the operational bandwidth and the power gain of the amplifier. In this thesis, our focus is on the linearity of the power amplifier, and two other factors of operational bandwidth and the power gain are visited briefly.

2.1 Power Amplifier Efficiency

The efficiency of the power amplifier is characterized as the ratio of the input power consumed to generate an output power of the RF signal. The consumed input power can be provided from DC and RF sources. Often this ratio is presented in the form of a percentage. There are two different figure of merits to present the efficiency of power amplifier:

- Drain Efficiency (DE): This figure represents the amount of DC drain power, which is consumed to generate an RF signal with a certain amount of power. The formula in (2.1) represents the calculation of DE.

$$\eta = 100 \times \frac{P_{out}}{P_{DC}} \quad (2.1)$$

where P_{out} represents the total RF signal output power, and P_{DC} is the DC power contributed to the drain of the amplifier. The measure of DE can reveal the efficiency of the amplifier at its final stage as well as the precision in load matching at the output of the amplifier.

- Power Added Efficiency (PAE): Unlike the drain efficiency, for power added efficiency, the RF signal input power to the amplifier is subtracted from the

RF signal output power. The equation for PAE is presented in (2.2)

$$PAE = \frac{P_{out} - P_{in}}{P_{DC}} = \eta \left(1 - \frac{1}{G}\right) \quad (2.2)$$

where P_{in} represents the RF input power of the amplifier, and G is the gain of the amplifier. Therefore, this figure takes into account the gain of the amplifier. For amplifiers with larger gains, PAE is similar to the DE. However, for small gain amplifiers, the amount of input power which is needed to drive the amplifier must be taken into account.

In Fig. 2.2 the DE and gain of the power amplifier are presented versus the input power of the amplifier. In the same figure, the efficiency of the amplifier is plotted in red. As the input power back-off increases, the amplifier shows a more linear response. However, the efficiency is close to 0%. By increasing the efficiency of the amplifier, i.e., the high input power region, the output signal gain shifts from the linear gain of the amplifier [33].

2.2 Power Amplifier Linearity

One of the significant sources of distortion in wireless transmitters occurs at the RF front end, due to the nonlinear characteristics of amplifiers. However, not all amplifiers show the same level of nonlinearity. Therefore, the topology and class of the amplifier have a significant role in the degree of nonlinearity introduced by them. The nonlinear relation of PA input/output can result in inband and out-of-band distortion. As a result, the signal fidelity may be affected with inband distortion by introducing the bit error rate and limits the data rate. As for out-of-band distortion, the spectrum of the transmitted signal may grow and therefore can violate the 3GPP regulations [34].

The response of the PA can be categorized to a linear region and nonlinear region. For an ideal linear PA response, the output is mapped linearly to the input signal as

it is depicted in Fig. 2.2. However, for a typical PA, the response can be divided to pseudo-linear and nonlinear regions (See Fig. 2.2).

One way to illustrate such response is in the form of high-order polynomial

$$y = \sum_{p=1}^{\text{inf}} \alpha_p x^p, \quad (2.3)$$

where nonlinearity orders of p are associated with coefficients α_p . In frequency domain, this high orders introduces harmonics above and bellow the fundamental frequencies. For largely enough coefficients of α_p , those harmonics can greatly results in spectral regrowth.

2.3 Power Amplifier Operational Bandwidth

Any power amplifier has a bandwidth that is adjusted to a span of frequencies of signals to be amplified. If the specifications of the amplifier's bandwidth are not met, the amplifier's output signal can lose some of its frequencies, or it can generate signals with the unwanted frequency range. Within the operational bandwidth, the power amplifier must have a flat frequency response and a sharp roll off outside its operational bandwidth.

The operational bandwidth are set by 3GPP for each designated communication standards. For LTE, the operational bandwidth can vary in the range of 5 – 200 MHz [35]. In the fifth generation wireless technology (5G), the frequency spectrum is divided into low-band, mid-band and millimeter-waves, where the operational bandwidth can range up to 2 GHz. As the operational bandwidth increases, challenging side effects are introduced by the power amplifier, which result in distortions. Memory effects are well known to be introduced in wideband power amplifiers, where the amplifiers does not behave in similar manner to the different frequencies of the input signal [36].

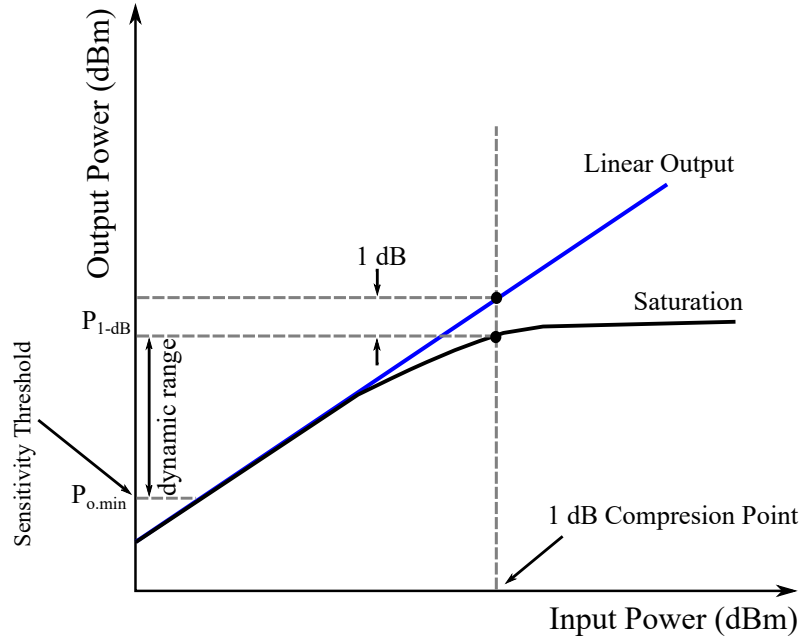


Fig. 2.3 Illustration of 1 dB compression point and dynamic range of a power amplifier.

2.4 Power Amplifier Dynamic Range

For an ideal power amplifier, the output signal is linearly mapped to the input. The plot from this ideal response can be shown as a straight line as it is depicted in Fig. However, as we discussed already, the real response of the power amplifier is distorted for some of the input signal power range. In Fig. 2.3, the linear response of an ideal amplifier is presented, where the linear gain is constant. The real output of the amplifier follows the linear gain for the input power. However, the gain gradually deviate from the linear gain of the amplifier and eventually goes to the saturation region. This phenomena is known as compression. The point where the real output of amplifier deviates from its linear gain for 1 dB, the amplifier is in its 1-dB compression point.

The lower delectable power of amplifier output is restricted by the input noise and it is usually measured at 3 dB above the noise level and it is noted by $P_{o,min}$ (See Fig. 2.3). The dynamic range of the amplifier is defined as

$$d_R = P_{1-dB} - P_{o,min}, \quad (2.4)$$

where the dynamic range identifies the region where the amplifier has a linear gain. In dynamic range, the amplifier preserve the signals gain and phase balance. Hence, for the signals with varying amplitude it is important to operate the amplifier in its dynamic range. Such signal schemes which depends on the amplifier constant gain are QAM, QPSK and OFDM signals. For signals with constant envelope scheme such as CW, FSK and GSM, there is no requirement to operate the PA within its dynamic range.

2.5 Power Amplifier Classes

Amplifiers are classified into two major groups. First group are the classical classes of amplifiers based on the conduction angle 2θ of the drain current or controlled conduction angle amplifiers such that the output stage transistor is between the region of ON and OFF. The amplifiers in this group are mainly linear mode amplifiers. The second group, is the classes of switch mode amplifiers, operating in either saturation or cut-off region.

2.5.1 Continuous Mode Amplifiers

Amplifiers with different linear classes of operation belong to this category and they can be categorized as:

- Class A: The mostly linear classes of amplifiers is the Class A where the conduction angle of the drain current is 360° . The linear operation region of this class of amplifiers can achieve the highest input power but in terms of efficiency its performance is poor around 50%, where the power is dissipated in the form of heat [37].
- Class B: To address the high dissipation of power in the form of heat in Class A amplifiers, Class B is introduced with no DC base bias current. Therefore, the efficiency increases at the cost of linearity [38]. The efficiency of Class B

amplifiers at its maximum can reach to 78.5%. The conduction angle of the drain or collector current in Class B amplifiers is 180° .

- Class AB: This class is one of the popular classes of amplifiers, providing moderate efficiency together with linearity. As a result, it can be considered an amplifier class between Class A and Class B [39]. The conduction angle of the drain current in Class AB amplifiers is reduced to $80^\circ \sim 120^\circ$. The efficiency of Class AB amplifiers can vary between 50% and 78.5%.
- Class C: In this class of amplifiers, the conduction cycle is reduced to $180^\circ \sim 360^\circ$. As a result, it can in theory achieve an efficiency of 90%. However, the reduced conduction cycle can introduce excessive distortion [40].

2.5.2 Switched Mode Amplifiers

The efficiency of amplifier increases when it is driven close to the saturation. When the amplifier is operating under saturation, it is in switch mode. Therefore, the switched mode amplifiers are considered to be more efficient than the continuous mode amplifiers. The efficiency of these amplifiers can in theory exceed 90% and reach 100% [41–43].

several classes of amplifiers are classified as follows:

- Class D: This class of switched mode amplifiers has at least two transistors, therefore it can form a square voltage waveform. The current alternates between the transistors, resembling a switch mode operation. This class can reach theoretical efficiency of 100%. However, the losses at saturation, low switching speed and drain capacitance are problematic with the Class D amplifiers. Latest research with current switching Class D amplifiers enables the Class D amplifier operation up to 4 GHz.
- Class E: Contradictory to Class D amplifiers, the Class E amplifiers only require one transistor. The basic idea in Class E amplifiers is to alternate between the current and voltage waveforms. Therefore, the switching losses are reduced.

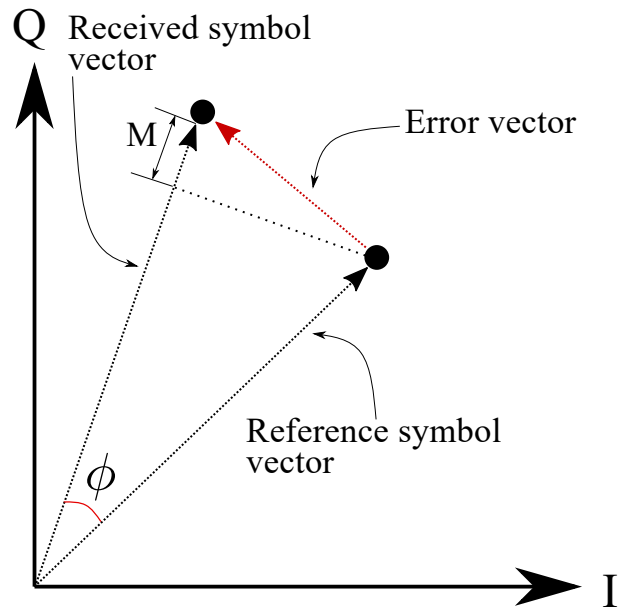


Fig. 2.4 Graphical representation of error vector magnitude.

This class can reach theoretical efficiency of 100%. This class is design for different frequency ranges up to millimeter waves.

- Class F: This class of amplifiers form the drain or collector waveforms by various harmonic resonators. By using more resonators the efficiency can be increased. the efficiency of this class when only one resonator is used is about 50%.

2.5.3 Advanced Designs of Amplifiers

In the design of power amplifiers, more sophisticated design approaches are developed to meet the linearity and efficiency. Based on this, different topology are advanced amplifiers such as Doherty [8], envelope tracking [14], and out phasing [15].

2.6 Figures of Merit

Any nonlinearity in the power amplifiers mentioned above can introduce distortion and must be studied and compensated carefully. Nonlinear characteristics of the

amplifier introduce different types of distortion, and they can generally be classified into two categories:

- In-band distortion: This group of distortion results in a degradation in bit error rate (BER) and data throughput.
- Out-of-band distortion: This group of distortion results in spectral regrowth and can violate the regulations.

To evaluate the amount of in-band distortion, error vector magnitude (EVM) is used as a figure of merit. The EVM measures the amount of deviation of the received demodulated signal constellation compared to the reference constellation points. The distortion due to the amplitude and/or phase. The amplitude distortion results in the magnitude error between the reference constellation and the received signal constellation. The phase distortion, on the other hand, results in a rotated constellation. Subsequently, a phase and amplitude distortion result in deviation in the magnitude and phase error. Therefore, EVM represents the error in the form of a vector. The EVM is calculated as

$$\text{EVM} = \sqrt{\frac{\frac{1}{N} \sum_{i=1}^N |e_i|^2}{\frac{1}{N} \sum_{i=1}^N |S_{ref,i}|^2}} \times 100\% \quad (2.5)$$

where e_i is the error vector for the i th demodulated symbol, $S_{ref,i}$ is the i th reference symbol vector in the constellation, and N is the total number of samples and presented in percentage form. The error vector e_i is visualized in Fig. 2.4, where the error vector is shown in red. This vector has both magnitude and phase distortion information. The angle ϕ represents the deviation in the phase of the received symbol, and M represents the magnitude of the distortion. Therefore, the received symbol in Fig. 2.4 shows both phase and magnitude distortion. The received signal must satisfy some threshold level of EVM for different standards. This is expressed in the specifications, and as the size of the constellation increases, the

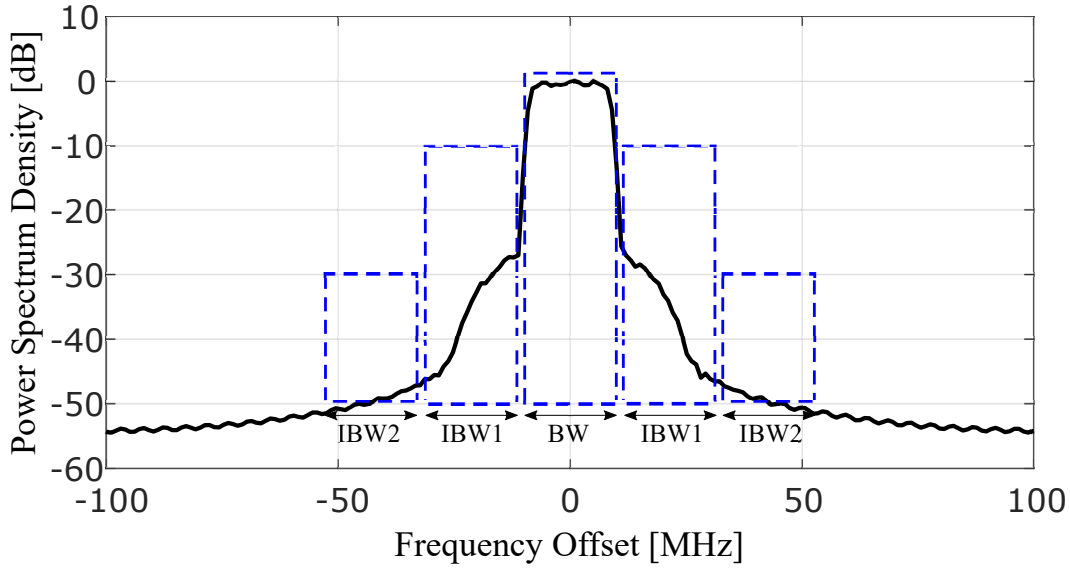


Fig. 2.5 Graphical representation of ACPR.

threshold becomes more conservative. Another figure of merit which is widely used to evaluate the linearity of the transmitter is the adjacent channel power ratio (ACPR). This figure evaluates the nonlinearity of the amplifier in the frequency domain when a modulated signal stimulates the amplifier. It is represented by the ratio of signal power in the main frequency band to the signal power in adjacent frequency bands. When the amplifier presents nonlinear characteristics, the modulated signal splatters into the adjacent channel and can interfere with the operation of the neighboring device in the adjacent bands. Therefore, it is crucial to monitor the ACPR for unwanted emissions to comply with the specifications. The ACPR should be limited to the threshold level in the technical specifications.

The graphical representation of the ACPR is presented in Fig. 2.5. In this figure, the in-band signal power at the bandwidth of interest is highlighted with BW. The integration bandwidth (IBW), i.e., IBW1 and IBW2, are representing the frequencies in lower and upper adjacent channels that the ACPR will be calculated for them. The ACPR is calculated as follows:

$$ACLR = \max_{m=L,U} \left\{ \frac{\sum_{f(adj)_m} |X(f)|^2}{\sum_{f.ch.} |X(f)|^2} \right\} \quad (2.6)$$

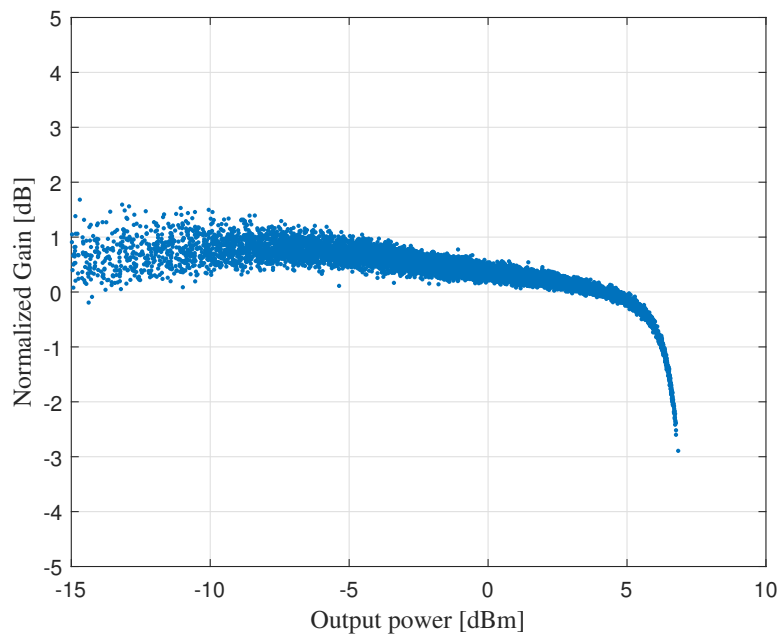


Fig. 2.6 Sample AM/AM characteristic of a power amplifier.

where $X(f)$ denotes the power spectrum of signal $x(n)$ for inband frequencies, i.e., f_{ch} and the frequencies in lower (L) and upper (U) adjacent channels $f(adj)_m$.

2.6.1 Power Amplifier Nonlinearity and Distortion

A power amplifier stimulated by a modulated signal exhibits different types of distortion. These types of distortions can be examined with different input signals.

- An ideal amplifier is expected to have a fixed gain. However, in reality, the amplifiers are showing distortion in output signal amplitude. Therefore, the amplitude of the output RF signal becomes a function of input signal amplitude. As a result, the amplifier can be characterized by its amplitude-to-amplitude distortion or AM/AM characteristics. An example of AM/AM distortion is depicted in Fig. 2.6.

For the input signal $x(t)$, the AM/AM can be defined as

$$y(t) = f(|x(t)|)x(t) \quad (2.7)$$

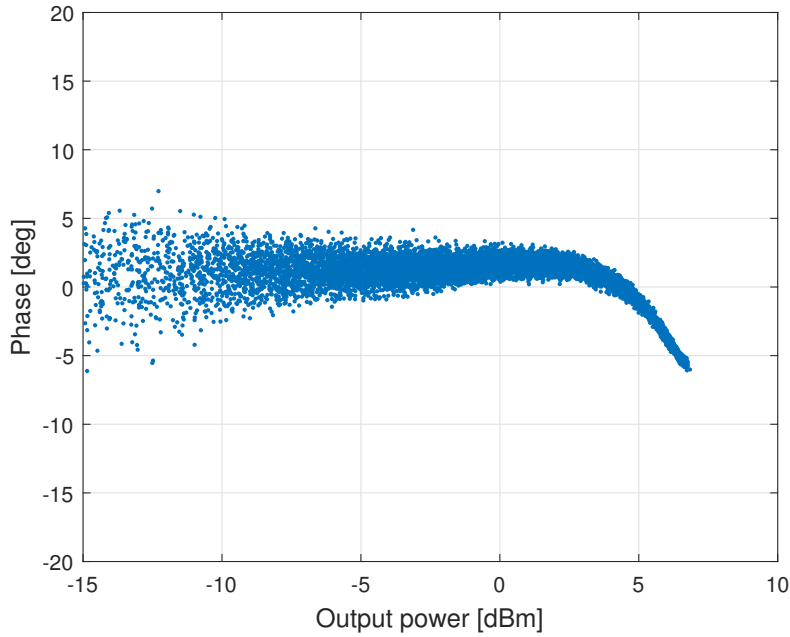


Fig. 2.7 Sample AM/PM characteristic of a power amplifier.

therefore the output signal $y(t)$ is an amplified version of the input signal where the gain of the output signal is a function of the input signal magnitude.

- Another type of distortion, which is often introduced at amplitude-to-phase distortion, i.e., AM/PM, characterizes the phase modulation distortion of the amplifier. An example of AM/PM distortion is depicted in Fig. 2.7.

The AM/PM distortion can be represented as

$$\angle y(t) - \angle x(t) = f(|x(t)|) \quad (2.8)$$

Subsequently, the amplifier exhibits both AM/AM and AM/PM distortion.

- The AM/AM and AM/PM distortions by the amplifier can be independent of frequency [44, 45]. It means that those characteristics of an amplifier do not depend on the operation frequency. Thus, the amplifier remains envelop-dependent. This can be due to a very narrow band modulated input signal to the power amplifier. These types of distortions are identified as static. However, as

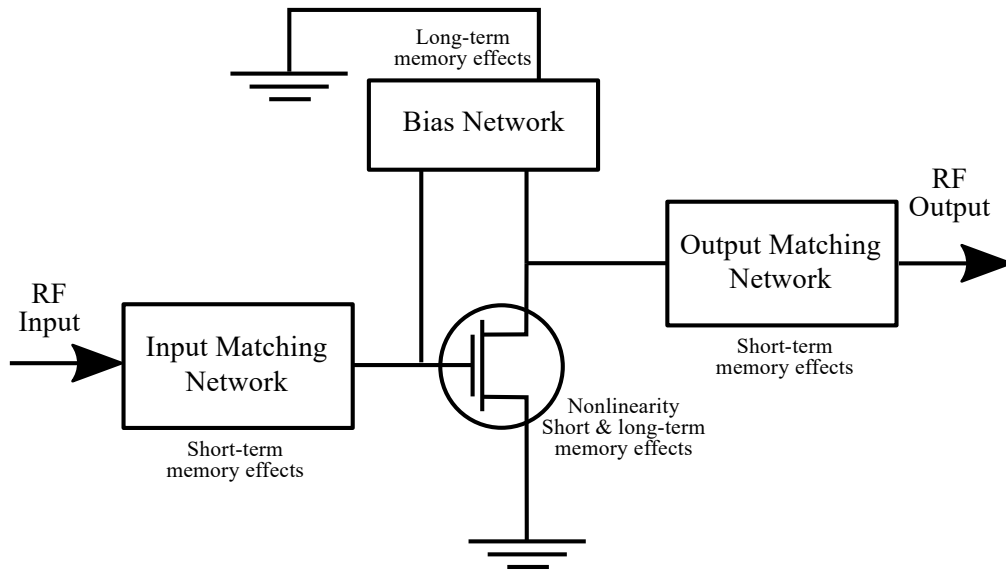


Fig. 2.8 Layout of power amplifier with the matching networks.

the bandwidth of the modulated signal increases, the amplifier shows frequency-dependent distortion. Therefore, this category represents AM/AM and AM/PM distortion, which are frequency dependent. This category is mostly regarded as nonlinearity with memory distortions and referred to as a dynamic model. The memory distortions do not introduce new spectra distortions. However, each sample point of AM/AM and AM/PM characteristics proliferates such that AM/AM and AM/PM characteristics are no more one-to-one. As it was shown in [46] the PA memory distortion can be modeled with a finite memory dependent model.

To identify the source of different distortions, the circuit level characterization of the amplifier can help. As it is depicted in Fig. 2.8, the transistor in the center of the amplifier has a nonlinear response. The nonlinear response of the transistor is mainly represented in the static type of distortions. On the other hand, the networks for biasing, input, and output matching contribute to the memory effects of amplifiers. The memory distortion can have different periods. Therefore they are generally categorized as short term and long term. To decide that the memory effects are falling into which category they are compared to the signal bandwidth. In the frequency domain, if the memory effects are small compared to the signal bandwidth,

they are considered as long term memory effects. On the contrary, the memory effects, which are in the frequency domain comparable with the center frequency of the transmitted signal, are categorized as short term memory effects [47]. The short term memory effects generally vary from nanoseconds to microseconds, and long term memory effects are on the order of milliseconds.

Short term memory effects are mainly contributed to the reactive components of the input-output matching network and the transistor, such as capacitors and inductors. Therefore, they are closely related to the bandwidth of the signal. When the bandwidth increases, these terms have a stronger effect. On the other hand, the long term memory effects are mainly contributed to temperature and aging of the PCB boards and DC self-bias.

In the time domain, the memory effects can be identified from the AM/AM and AM/PM plots. The spread in these two graphs indicates the presence of memory effects. However, in the frequency domain, they cause an imbalance of the upper and lower adjacent channel of power spectra [47].

In order to identify and mitigate the distortion of the amplifier, an accurate model of the amplifier must be identified. Circuit-level modeling is a complicated approach. However, an alternative approach is to perform behavioral modeling. This technique is the basis for one of the efficient and widely used amplifier linearization techniques, i.e., digital predistortion (DPD). In Section 2.7, the behavioral modeling for amplifier is presented. Next, in Section 2.8, the DPD technique basics are presented.

2.7 Amplifier Behavioral Modeling

In order to model the static and dynamic nonlinearities of amplifiers, a model that can present the nonlinearity and memory effects of the amplifier must be chosen. It is important to select the right model to have a precise representation of the system [48]. Therefore, the amplifier output can be modeled as:

$$y(n) = f(x(n)) \tag{2.9}$$

where the function $f(\cdot)$ represents a nonlinear relationship such as

$$y(n) = \sum_{p=1}^P \alpha_p x^p(n) \quad (2.10)$$

where P is the maximum nonlinearity order in this model. However, as the bandwidth of transmitted signal increases, an alternative model must be implemented, which takes into account for memory effects. Among the available models, approaches like the Volterra series are the most popular ones to model the nonlinearity as well as the memory effects [49, 50]. The Volterra series model is formulated in [51] as follows:

$$y(n) = \sum_{p=1}^P \sum_{m_1=0}^M \dots \sum_{m_k=0}^M h_p(m_1, \dots, m_k) \prod_{j=1}^p x(n - m_j) \quad (2.11)$$

where P is the nonlinearity order and M is the memory order of the system, and parameters $h_p(m_1, \dots, m_k)$ are the model Kernels which must be estimated. The interesting property of the Volterra series is that the model basis contains all variations and combinations of different memory depths. When the model is used to express the signals in baseband, the Volterra model is in this form:

$$y(n) = \sum_{p=1}^P \sum_{m_1=0}^M \dots \sum_{m_k=0}^M h_p(m_1, \dots, m_k) \prod_{j=1}^{(p+1)} x(n - m_j) \prod_{l=p+2}^{(2p+1)} x^*(n - m_l) \quad (2.12)$$

In this form, the combinations of signal x and its conjugate, i.e., x^* , are in the form that the conjugate signal always has one order less than its non-conjugate counterpart. By this means, the signals are granted to represent only the harmonics in the vicinity of baseband [52].

Introducing the memory effect with the full-Volterra series leads to highly complex models. The results are not always efficient in terms of complexity analysis. Considering the fact and the measurements which are used as model signals are limited to the noise floor of the measurement equipment. Therefore, even with increases the size of the model orders, no improvement can be obtained.

Other simpler models have been introduced to model the memory effects such as memory polynomial [36] and generalized memory polynomial [52]. The memory polynomials based models are the most widely used ones with excellent precision. Subsequently, in this thesis, the models are mainly based on the MP model.

2.7.1 Memory Polynomial Model

The memory polynomial model is a simplified version of the Volterra series-based model where the cross terms between the signal and its different lagging or leading terms are avoided [36]. Therefore, the complexity of the model is significantly reduced. Still, this model can achieve sufficient accuracy in modeling the amplifier nonlinearity and its memory effects. The baseband complex envelope representation of the output signal is generally represented as follows:

$$y(n) = \sum_{p=1}^P \sum_{m=0}^M \alpha_{mp} x(n-m) |x(n-m)|^{2p} \quad (2.13)$$

where $|\cdot|$ denotes the absolute value of signal $x(n)$ and α_{mp} is the model coefficient related to nonlinearity order of p and memory depth of m . Since the model is linear with respect to the model parameters, the model can be represented in this alternative form:

$$\mathbf{y} = \Phi(\mathbf{x})\boldsymbol{\alpha} \quad (2.14)$$

where \mathbf{y} is a vector of the captured output signal, \mathbf{x} is the vector of the input signal to the system and $\boldsymbol{\alpha}$ is a vector which contains the model parameters, i.e., $\boldsymbol{\alpha} = [\alpha_{10}, \dots, \alpha_{PM}]^T$. The matrix $\Phi(\mathbf{x})$ is formed from the basis functions of the memory polynomial model, i.e., $\Phi(\mathbf{x}) = [\mathbf{x}(n), \mathbf{x}(n-1), \dots, \mathbf{x}(n-M)|\mathbf{x}(n-M)|^{2P}]$ and vector $\mathbf{x}(n) = [x(n), x(n-1), \dots, x(n-N)]^T$ contains N samples of the input signal and $(\cdot)^T$ denotes transpose.

2.7.2 Model Identification

Once the model is selected, its coefficients must be identified. The identification procedure can be performed for a set of measured input and output signals to the system, which we want to model and in this case, the amplifier. For this, a large vector of a signal is sent to the device under test, and the output is captured. As it is defined in (2.14), the model is linear with respect to the coefficients $\boldsymbol{\alpha}$. The linear models can be solved with different estimation techniques such as least mean squares (LMS) [53, 54], linear least-squares (LS) [55–57], and recursive least squares (RLS) [19, 58]. Among other techniques, linear least-squares shows stability and is used in this thesis. Subsequently, the least-squares can be solved as

$$\boldsymbol{\alpha} = \Phi(\mathbf{x})^+ \mathbf{y} \quad (2.15)$$

where $(\cdot)^+$ is the Moore-Penrose pseudoinverse function [59–61] such that

$$\mathbf{X}^+ = (\mathbf{X}^H \mathbf{X})^{-1} \mathbf{X}^H \quad (2.16)$$

where $(\cdot)^H$ denotes the matrix Hermitian transpose and $(\cdot)^{-1}$ denotes the matrix inversion. Therefore, the model parameters can be extracted for a large batch of input and output signal samples. The size of the batch impacts the accuracy of the least-squares estimation technique, and it must be large enough.

2.7.3 Model Accuracy Evaluation

In order to evaluate the precision of the estimated model, different metrics can be used. The most common ones are the normalized mean square error (NMSE), the adjacent channel error power ratio (ACEPR). The NMSE measures the accuracy of estimated time samples one by one, and it is closely related to the EVM measurements. If translated to the frequency domain, it mainly measures the accuracy of the inband

output signal. The NMSE is defined as

$$\text{NMSE} = \frac{\sum_{n=1}^N |y(n) - \tilde{y}(n)|^2}{\sum_{i=1}^N |y(n)|^2}, \quad (2.17)$$

and it is mainly represented in the form of dB. The achievable accuracy of NMSE is limited to the level of noise in measured signal $y(n)$ and cannot be improved further.

The ACEPR is defined in [62] and it measures the accuracy of the model output in frequency domain and for the adjacent channels can be calculated as follows

$$\text{ACEPR} = \max_{m=L,U} \left\{ \frac{\sum_{f(adj)_m} |Y(f) - \tilde{Y}(f)|^2}{\sum_{fch.} |Y(f)|^2} \right\} \quad (2.18)$$

where $Y(f)$ denotes the power spectrum of the measured output signal $y(n)$ for inband frequencies, i.e., fch and the frequencies in lower (L) and upper (U) adjacent channels $f(adj)_m$ and $\tilde{Y}(f)$ denotes the power spectrum of the model output signal $\tilde{y}(n)$.

2.8 Digital Predistortion

DPD is an amplifier linearization technique based on the principle of intentionally predistorting the input signal such that the overall performance of the transmitter becomes linear. The procedure of predistorting the signal is implemented in digital baseband; therefore, the technique is called digital predistortion. The DPD is a nonlinear system with a transfer function that mimics the inverse behavior of the power amplifier. Accordingly, the distorted signal from DPD has the same magnitude and is out of phase from those generated by the power amplifier, and they cancel each other out. A simple block diagram of a transmitter utilizing a DPD is depicted in Fig. 2.9.

The central aspect of DPD is its stable and straightforward principle. Moreover, the technique implementation does not increase the power consumption compared

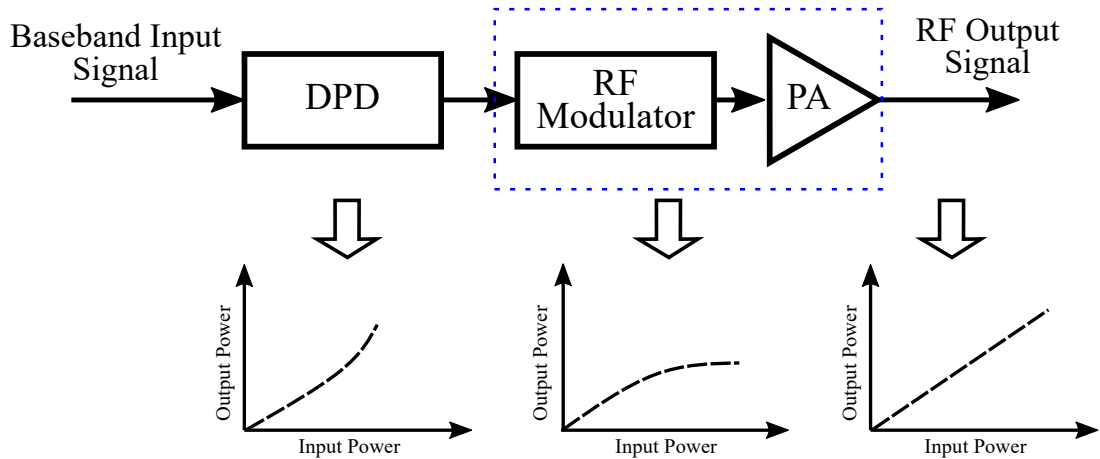


Fig. 2.9 Digital predistortion operation principle.

to the power amplifier. The accuracy of the DPD performance is closely related to the signal characteristics, e.g., bandwidth, peak average power ratio (PAPR), modulation, and power. Therefore, the DPD must be adopted for the operating specifications based on the properties of the signal. Therefore, mainly, adaptive signal processing techniques are related to the performance of DPD.

2.8.1 DPD Model and Identification Techniques

The first step in the implementation of a DPD is to present a nonlinear model. This model must comply with the model, which is used to present the power amplifier in terms of nonlinearity order and the memory depth. Similar models represented in Section 2.7 can be utilized for DPD application. To estimate the DPD model parameters or coefficients, different approaches have been proposed. The most well-known ones are listed as indirect learning (ILA) [63–66] and direct learning or closed-loop (DLA) [32, 67–70]. In this thesis, both of these techniques have been used for different applications. The operation of these two techniques are explained as follows.

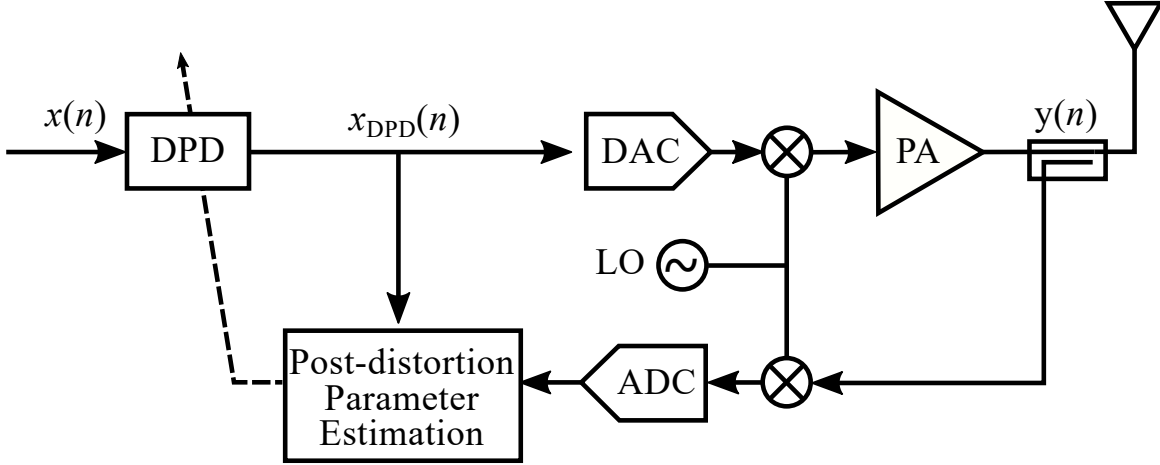


Fig. 2.10 Block diagram of an RF transmitter with DPD based on ILA.

2.8.1.1 Indirect Learning Technique

The indirect learning algorithm principle is depicted in Fig. 2.10. This learning algorithm is based on the estimation of the DPD parameters from the inverse model of the power amplifier such that the amplifier output signal $y(n)$ is used to form the basis functions of the nonlinear model. Therefore, the cost function to be minimized is

$$J_{\text{ILA}} = \| \mathbf{e} \|_F^2 \quad (2.19)$$

where \mathbf{e} is a vector of error signal such that $e(n) = x_{\text{DPD}}(n) - y(n)$, and $\| \cdot \|_F$ represents the Frobenius norm.

The estimation of the inverse amplifier model is called post-distortion. The post-distortion takes the amplifier's output signal, i.e., $y(n)$, as the input to the model when the amplifier is excited with the signal x_{DPD} . Thus we have

$$\mathbf{x}_{\text{DPD}} = \Phi(\mathbf{y})\boldsymbol{\theta}_{\text{ILA}} \quad (2.20)$$

where $\Phi(\mathbf{y}) = [\mathbf{y}(n), \mathbf{y}(n-1), \dots, \mathbf{y}(n-M)|\mathbf{y}(n-M)|^{2P}]$, for a memory polynomial model with nonlinearity order of P and memory depth of M . The model parameters to be estimated are stored in vector $\boldsymbol{\theta}_{\text{ILA}}$. Similar to the previous approach of model

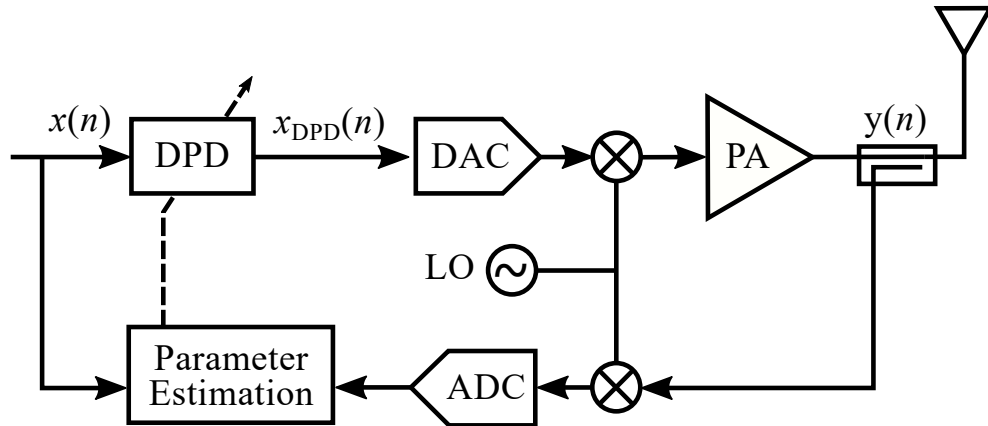


Fig. 2.11 Block diagram of an RF transmitter with DPD based on DLA.

estimation in Section 2.7.2, by least-squares approach the parameters $\boldsymbol{\theta}_{\text{ILA}}$ are given by

$$\boldsymbol{\theta}_{\text{ILA}} = \Phi(\mathbf{y})^+ \mathbf{x}_{\text{DPD}} \quad (2.21)$$

The ILA technique is susceptible to noise [71]. The reason is the construction of basis functions, $\Phi(\mathbf{y})$, based on the measured amplifier output signal, \mathbf{y} . The measurement noise can propagate throughout the estimation and results in biased parameter estimation. In order to reduce the dependency of basis functions on the measured signal $\Phi(\mathbf{y})$, a model-based ILA (MILA) technique has been introduced [72]. In this technique, first, the amplifier model is extracted, and substitutes for actual PA in the linearization process. The technique is further explained in Section 4.2.1.

2.8.1.2 Direct Learning Technique

The DLA technique is robust against the measurement noise. Unlike ILA, in this technique, the DPD is placed within the linearization loop; therefore, DLA is called closed-loop as well. A simple block diagram of a DLA technique is depicted in Fig. 2.11. In this technique, the error between the input to the DPD and the output of

Background

the amplifier is minimized. Therefore, the cost function to be minimized is

$$J_{\text{DLA}} = \| e - \Phi(\mathbf{x})^T \Delta \theta \|_F^2 \quad (2.22)$$

where $\Delta\theta$ is the vector of the residual model parameters and $\Phi(\mathbf{x}) = [\mathbf{x}(n), \mathbf{x}(n-1), \dots, \mathbf{x}(n-M)|\mathbf{x}(n-M)|^{2P}]$. Through a few iterations the DPD parameters can be updated. First, by utilizing the least-squares, the estimation of coefficient residual is obtained as

$$\Delta\theta = \Phi(\mathbf{x})^+ \mathbf{e} \quad (2.23)$$

Then, the DPD parameters are updated as

$$\theta^{i+1} = \theta^i + \Delta\theta \quad (2.24)$$

where $\theta^i = [1, 0, \dots, 0]$. Since, the basis functions $\Phi(\mathbf{x})$ are built based on the input signal \mathbf{x} , this technique is less sensitive to the measurement noise.

2.8.2 DPD Performance Evaluation

For evaluation of the DPD performance, the linearity of the transmitter must be measured. Same as the amplifier model evaluation, the NMSE can be used for performance evaluation of the DPD. The NMSE for DPD is measured as the difference of the input signal to the DPD and gain-normalized amplifier output signal as

$$\text{NMSE} = \frac{\sum_{n=1}^N |x(n) - \tilde{y}(n)|^2}{\sum_{i=1}^N |x(n)|^2} \quad (2.25)$$

where $\tilde{y}(n)$ is the gain-normalized output of the amplifier such that

$$\tilde{y}(n) = \frac{y(n)}{G} \quad (2.26)$$

where G is the linear gain of the amplifier. Different gain-normalization techniques have been proposed based on maximum gain, gain at the maximum targeted power level, and variable gains [73]. In this thesis, the normalization is performed based on the maximum gain of the amplifier.

Another critical parameter to evaluate the performance of DPD, and consequently, the linearity of the transmitter, is the adjacent channel power ratio (ACPR). The ACPR represents the distortion reduction in adjacent channels, and it is calculated by

$$\text{ACPR} = \max_{m=L,U} \left\{ \frac{\sum_{f(adj)_m} |Y(f)|^2}{\sum_{fch.} |Y(f)|^2} \right\} \quad (2.27)$$

where $Y(f)$ denotes the power spectrum of PA output signal $y(n)$ for inband frequencies, i.e., fch and the frequencies in lower (L) and upper (U) adjacent channels $f(adj)_m$.

Chapter 3

MIMO Transmitters- Introduction and Review

The increasing demand for high data rates has motivated the development of techniques to increase the channel capacity by optimizing the spectral efficiency of future wireless communication networks. Massive multiple-input multiple-output (MIMO) systems have emerged as the most favorable physical-layer solution for achieving high data rates, connection reliability, and high spectral efficiency in fifth-generation (5G) and beyond communication systems [2].

The MIMO communication system is a scalable transceiver employing several independent radio frequency (RF) chains to stimulate an antenna array; individual RF transmitters contain a power amplifier (PA) that drives a distinct antenna element. The major blemish of the ever growing large MIMO transmitter is its cost, size, and complexity. Therefore, compact and simplified techniques for linearization are desired, where the removal of several hardware components reduces the complexity. Therefore, new hardware architecture, together with more sophisticated signal processing approaches, must be adopted. To further increase the spectrum efficiency by exploiting the millimeter wave (mmWave) bands with extremely short wavelengths, it is possible to shrink the size of the transceivers. The spectrum efficiency of massive MIMO systems can be achieved by performing beamforming techniques in a rich

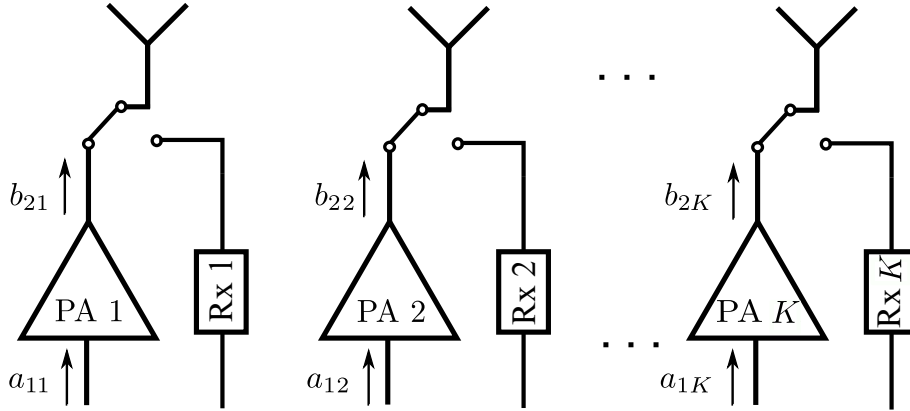


Fig. 3.1 MIMO TDD system model in absence of crosstalk.

scattering environment [74]. Phased arrays are widely used to perform beamforming; therefore, they are another part of this study.

Recent studies show the benefits of implementing 5G technologies such as Massive MIMO in time-division duplex (TDD) since the pilot overhead is prohibited in frequency-division duplex (FDD) [75, 76]. In particular, the physical propagation channels for TDD systems are reciprocal since the uplink receiver and downlink transmitter, i.e., the transceivers, are sharing the same antenna by exploiting a switch as depicted in Fig 3.1.

In this chapter, first, the challenges for MIMO TDD systems and phased array's system linearization are visited. Then, the system model for MIMO systems and phased arrays suffering from impairments are explained. The previous works which addressed the new issues raised from the MIMO and phased array hardware architectures are explained, and the technology gap, which is studied in this thesis, is briefly visited. Therefore, in this chapter, the contribution of this thesis in relation to the already published works has been identified.

3.1 MIMO System and Phased Array Challenges

The MIMO system considered in this thesis is built from several transmit and receive paths. Each transmit path has its digital baseband, a digital-to-analog converter (DAC), and an RF path with PA, which is connected to an antenna

element. Each receive path contains an antenna element, typically, a low noise amplifier (LNA), a down-converter and an analog-to-digital converter (ADC). The antenna elements collectively form an antenna array. By increasing the number of transceiver paths in MIMO systems, the physical size and the cost of the transceiver and array play a critical role. Therefore, very compact and simplified techniques for linearization are desired, where the removal of several hardware components reduces the complexity. Therefore, new hardware architecture, together with more sophisticated signal processing approaches, must be adopted. However, the feasibility of the new analog and digital solutions must be evaluated carefully. The conventional linearization techniques which have been used previously for single path transmitters can no longer be used in the new architectures.

The large MIMO systems are especially vulnerable to crosstalk and coupling effects when implemented on a single chipset [77] due to the proximity of transmit paths. As a result, the linearization can suffer from additive linear or nonlinear distortion. The linear crosstalk or antenna crosstalk [78] can affect the output of PA and does not couple into the incident wave into the PA. Nonlinear crosstalk is the coupled signal which becomes an incident wave to the PA input or output, and therefore, will contribute to an excessive nonlinear distortion in PA output signal. One of the instances of nonlinear crosstalk occurs in MIMO systems where the transmitters share a local oscillator (LO) to save area and cost of it by reducing the power consumption of the synthesizer [79, 80]. Another case of nonlinear crosstalk occurs when the isolators between the PA output and the antennas are avoided. The isolators are two-port components that transmit the signal in one direction only. Therefore, it prevents any wave from being incident to the PA output, which can protect the PA. By eliminating the isolators, the PA behavior can change accordingly [81].

Both linear and nonlinear crosstalk are sources of excessive distortion. Therefore, the conventional way to model the PA and compensate for its distortions cannot be used to compensate for the PA distortion together with crosstalk distortion fully.

Another challenge to face in large size MIMO systems is related to the increased number of the transmitter observation receivers (TORs), which are an inevitable part of the linearization feedback loop. These TORs must be implemented for each transmit path, and they must be synchronized, and when the number of the transmitters increase, it might be even impossible to capture the signal and process them via separate TORs. TOR, which is built from a complete receiver chain, must be implemented for each transmit path. An essential component of every TOR is an analog-to-digital converter (ADC), and for most ADCs, the power consumption scales with the sampling rate. By reducing the number of TORs, the cost and the size of the MIMO systems can be kept low. However, alternative solutions must be sought to provide the necessary feedback signals to perform the linearization.

Several studies have tried to reduce the number of TOR paths. The authors in [82] and [83] propose the use of a shared feedback receiver chain, where the individual PA outputs were sensed with separate couplers, and the signals were collected with a switch through a time-sharing technique. In another study, Prata *et al.* [84] investigates the training of a MIMO DPD with multi-sines with different frequency placements of each tone and capture the combined signal of PA outputs with a shared feedback receiver. The implementation of a shared TOR in the above techniques relies on the feedback signal captured by the couplers. However, in millimeter-wave (mm-wave) frequency bands, the coupler's insertion loss becomes more significant and problematic.

Recently, over-the-air (OTA) measurements to provide the TOR feedback signal have been proposed for phased arrays as an alternative solution where a limited number of receive antennas capture the transmitted signals[85–87]. The structure of a phased array is such that one baseband data stream to be directed to a specific direction is split and fed to several RF transmitter chains with separate dedicated PAs. Therefore, only one DPD can be trained to linearize the radiated field in the direction of the user. This single DPD is expected to linearize several PAs, each of which can have different characteristics [88]. As the size of the array increases, this can result in a drastic increase in the difference in PA performance. Therefore,

an optimized model must be used for analysis, modeling, and predistortion with possibly low power consumption and computational complexity.

However, a fully digital MIMO system with a digital path per RF PA requires a DPD per transmit path and is therefore not suitable for MIMO systems. This makes OTA-based modeling and linearization of the MIMO system a more complex task.

In [89], Hausmair *et al.* propose to use a few dispersed receiver antennas to collect the combined transmitted signals with OTA measurements. The received signals are used to identify individual PA models, and accordingly, performing the linearization for each PA. Nonetheless, it is based on the assumption that the coupling coefficients between the transmitter and the receiver antennas are known and assuming that the transmitting antennas are isolated.

As already discussed in this section, a typical implementation of the DPD technique is done in digital baseband and requires as many feedback paths and predistorders as the number of power amplifiers. However, for phased array systems where one digital baseband branch is connected to several analog transmission paths in RF, only a single DPD can be implemented per sub-array. This single DPD is expected to linearize several PAs, each of which can have different characteristics. Different strategies can be applied to optimize single DPD performance. In [90], the authors propose a single DPD technique to linearize multiple PAs in a phased array. Their proposed solution relies on minimizing the sum of the least squared errors of the different branches. A beam-oriented single DPD is introduced in [91], where a single DPD is employed to linearize the primary beam signal. The proposed DPD is based on minimization of the least square error of the superposition of the PA outputs after the effect of analog beamformers are removed. An array DPD was introduced by [92], where the combined error in the far-field is minimized. The combined error is estimated by taking the feedback from all PAs. Then, the combined response of the array in the far-field is estimated and comparing it with the input signal to the PAs. The work in [93] is using the same approach by canceling the beamforming weights before combining it via an anti-beamforming module. Further, the effect of phase and amplitude mismatch of feedback signals on the DPD learning algorithm has been

investigated. In [94], a single DPD is trained to linearize the sub-array by modeling the primary beam signal and comparing it with the input signal and observe the signal linearity in the far-field. The previous studies mainly focus on the array response rather than the individual PA output. Hence, the linearization technique fails when the PAs in the different branches possess considerably different characteristics. As it was discussed in [92], the linearization of the phased array, results in a more linear behavior of those PAs with the initial nonlinear response, while those PA with initial linear behavior is experiencing a nonlinear behavior after linearization. In [92], the linear PA behavior is related to those PAs with excitation signals at lower input power. Therefore, after linearization, their nonlinear characteristics are not dominating. However, if all the PAs are excited by the input signal with the same power level, this effect can reduce the desired level of linearization at the position of user. This improved performance is especially notable when the PAs in the different branches possess considerably different characteristics. The DPD learning utilizes a closed-loop estimation technique which is not sensitive to the PA output noisy measurements.

3.2 MIMO TDD System Models

Similar to the single path transmitters, the MIMO systems suffer from distortion. The primary source of distortion is the PA. Furthermore, the additional sources of distortion must be taken into account when the transceivers are designed on a single chipset. In such a system, the effect of antenna coupling and impedance mismatch must be carefully studied and specified in PA modeling and identification [95]. The detrimental effect of coupling between antenna elements in a MIMO TDD system can be useful as we show it later in this thesis, where we develop an OTA approach as a substitute for conventional TOR circuitry. We first develop the system model for intra-array transmission of a MIMO TDD transceiver. Two different models can be studied based on the presence or absence of crosstalk in the form of antenna coupling and impedance mismatch.

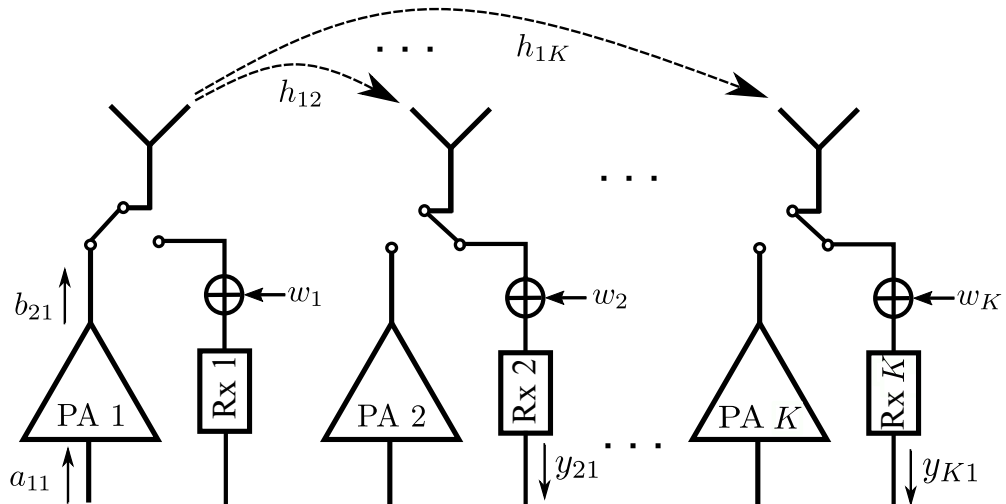


Fig. 3.2 Block diagram of a MIMO system with K transceivers with one transceiver in transmit mode while the rest of the array elements are receiving.

3.2.1 Intra-Array System Models Without Crosstalk

In this section, we present the system model of a TDD MIMO system when no crosstalk presents. For the sake of readability, the time dependence is not included, such that, for example, $a_1(n)$ is written as a_1 .

Each transceiver consists of a transmitter chain (Tx) and a receiver chain (Rx), which utilizes a switch to alternate between transmit and receive mode. The operating frequency band is identical for all transceivers.

A block diagram of a TDD MIMO with K transceivers is shown in Fig. 3.2, where, in this case, the first transceiver is in transmit mode, while the rest of the transceivers are listening in receive mode. Each Tx contains a digital-to-analog converter (DAC) and an RF PA connected to an antenna element. When no I/Q imbalance is present, the PA model may fully represent a transmit path from a digital-to-analog converter (DAC) to the RF PA. In receive mode, the Rx shares the same antenna with the transmit chain and contains, typically, a low noise amplifier (LNA), a down-converter and the analog-to-digital converters (ADCs).

As it is depicted in Fig. 3.2, when the j th transmitter sends a vector of pilot signal $\mathbf{a}_{1j} \in \mathbb{C}^{N \times 1}$, it follows that the received signal at the i th transceiver, y_{ij} , can be modeled with the transmitter block, the propagation channel, and the receiver

block as follows

$$\begin{aligned} \mathbf{y}_{ij} &= r_i h_{ij} \mathbf{b}_{2j} + \mathbf{w}_{ij} \\ &= r_i h_{ij} f_j(\mathbf{a}_{1j}) + \mathbf{w}_{ij}, \end{aligned} \tag{3.1}$$

where r_i is the complex gain of the Rx in the i th receive chain from RF-to-baseband. The function f_j is the PA response in the j th Tx path. The elements of vector $\mathbf{w}_{ij} \sim \mathcal{CN}(0, N_0)$ are the additive complex Gaussian noise at the receiver with variance N_0 . The complex term h_{ij} stands for the reciprocal propagation channel between the i th receiver antenna and the j th transmit antenna due to the mutual coupling. The hardware responses of r_i and f_j are dynamic and can vary with changes in temperature, voltage variation, etc. Nonetheless, in the rest of this thesis, we consider the hardware responses of r_i and f_j to be constant with respect to the symbol duration.

As it was already discussed in Section 2.7 different Volterra series based modeling techniques can be used to present the PA behavioral model.

3.2.2 Intra-Array System Models With Crosstalk

For MIMO systems implemented on a single chipset, the electromagnetic coupling between the antenna array elements forms the crosstalk. Furthermore, the impedance mismatch between the PA output and antenna introduces a reflection signal which elaborates in the formation of a crosstalk signal. When no isolator is used between the PA and antenna, the crosstalk can be modeled. In [96], the authors provide a dual-input PA model that is capable of modeling the reflection signal at PA input and output while taking care of the dynamic effects of the PA. Therefore the technique is capable of modeling the wideband signals too. In smart antenna transmitters with several transmit paths and the presence of antenna coupling, the PA behavior is studied in [95] and [97]. The work by Fager *et al.* [97] presents a technique to estimate the PA behavior in a two-branch smart antennas transmitter. The results are presented in terms of spectrum measurements and showed a satisfactory level

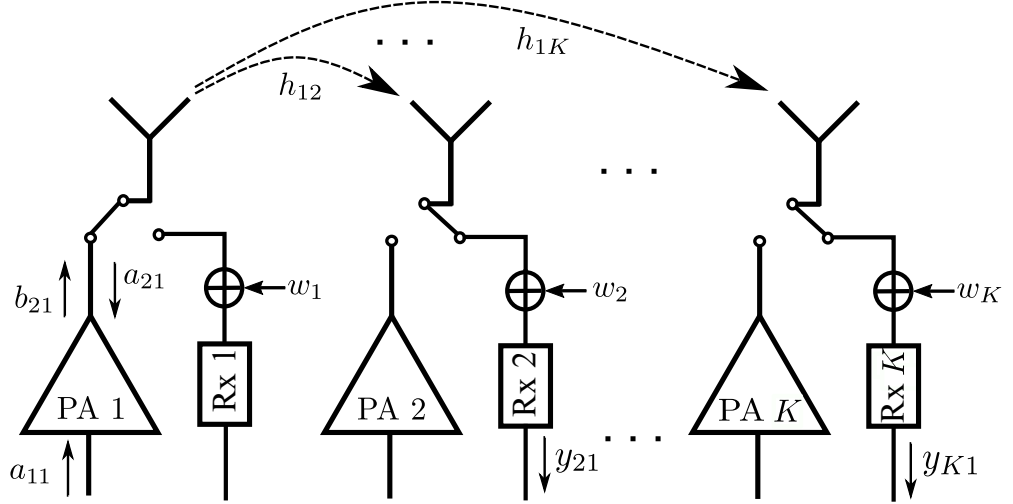


Fig. 3.3 Block diagram of a MIMO system with K transceivers with one transceiver in transmit mode while the rest of the array elements are receiving in presence of crosstalk.

of accuracy in the predicted PA behavior. The technique was expanded in [95] to account for the dynamic effects of the PA. Therefore, extended the application of it for wideband excitation.

In our study, we adopt the dual-input PA model, which benefits from the ability to represent the frequency-dependence, i.e., dynamic effects of the PA. A block diagram of such a system is depicted in Fig. 3.3. By exploiting the aforementioned dual-input PA modeling technique, the intra-array signal transmission can be modeled as follows

$$\begin{aligned} \mathbf{y}_{ij} &= r_i h_{ij} \mathbf{b}_{2j} + \mathbf{w}_{ij} \\ &= r_i h_{ij} f_j(\mathbf{a}_{1j}, \mathbf{a}_{2j}) + \mathbf{w}_{ij}, \end{aligned} \quad (3.2)$$

where the signal \mathbf{a}_{2j} is the incident wave toward PA output. This signal represents the crosstalk due to the antenna coupling and mismatch. When the antenna is wideband compared to the bandwidth of the transmitted signal, the incident signal a_{2j} can be express as a linear combination of b_2 signals as follows [95, 97]

$$a_{2j} = \sum_{k=1}^K b_{2k} \lambda_{kj}. \quad (3.3)$$

It worth noticing that when the reference plane is well defined, the scattering parameters (S-parameters) obtained at the antenna terminals can partially describe the effective coupling, i.e., the S-parameters only reflects the h_{ij} and eliminates the r_i . Hence, for wideband antennas, the S-parameters at the center the frequency may be equivalent to the λ_{ki} up to a point.

In order to accommodate the linear and nonlinear dynamic effects of PA with fading memory into this model, the excessive terms are introduced. By taking into account the memory effects, the accuracy of the model for wideband signals increases. As a result, the Volterra series based model with memory effects become extremely high in the order, makes it infeasible to implement such a model in digital baseband processing. Therefore, depending on the available baseband processing resources, the pruned approaches are adopted to substitute for the Volterra series model. As we already discussed in Section 2.7, memory polynomial (MP) is a popular, reduced form which is exploited frequently as a PA modeling methodology. A dual-input model based on MP approach can represent the PA behavior, when the PA output is a function of a signal at its in- and outputs, i.e., $f(a_{1j}, a_{2j})$ [98]. A dual-input dual-output PA model was presented in [96], which incorporates the reflection signal toward the PA input and output. Then, a double-input single-output model has been adopted in [95] and [99] where the PA output in multi-antenna systems is affected by impedance mismatch and crosstalk. Instead of pursuing crosstalk and mismatch model (CTMM) approach in [99] to model the effect of coupling and load mismatch, our modeling approach uses the estimated couplings explored in the previous section.

Accordingly, the baseband description of $f(a_{1j}, a_{2j})$ can be adopted with an equivalent memory polynomial structure where the dynamic effects of hardware are taken into account especially when wideband signals are transmitted [100]. Hence,

$b_{2j}(n)$ can be written as

$$b_{2j}(n) = \sum_{m_1=0}^M \sum_{p=0}^{(P-1)/2} \alpha_{jpm_1} a_{1j}(n - m_1) \quad (3.4a)$$

$$\begin{aligned} & \times |a_{1j}(n - m_1)|^{2p} \\ & + \sum_{m_2=0}^M \beta_{j0m_2} a_{2j}(n - m_2) \\ & + \sum_{m_1=0}^M \sum_{m_2=0}^M \sum_{p=1}^{(P-1)/2} \beta_{jpm_1m_2} \end{aligned} \quad (3.4b)$$

$$\begin{aligned} & a_{2j}(n - m_2) \times |a_{1j}(n - m_1)|^{2p} \\ & + \sum_{m_1=0}^M \sum_{m_2=0}^M \sum_{p=1}^{(P-1)/2} \gamma_{jpm_1m_2} a_{2j}^*(n - m_2) \\ & \times (a_{1j}(n - m_1))^{p+1} (a_{1j}^*(n - m_1))^{p-1}, \end{aligned} \quad (3.4c)$$

where M represents the memory depth and P are the degree of nonlinearity order.

The cross terms in (3.4b) and (3.4c) only contain the linear representation of a_{2j} and a_{2j}^* . This is due to the fact that the incident wave a_{2j} is considered to have lower power [101]. However, for signals with a significant power level, a higher order of the a_{2j} must be considered.

3.3 Phased Array System Models

In this section, the system model of a phased array with K transmit antennas is presented. This system model represents a $K \times 1$ precoded single-user MIMO downlink (DL) transmission, with K transmit antennas at the base station and a single antenna UE. An assumption has been made that the channel is known; therefore, the precoding in the base station is carried out by knowing the channel. Here, $a_1 = [a_{11}, a_{12}, \dots, a_{1K}]$ is the pre-coded transmitted data vector and s is the single-stream of transmitted data symbol which satisfies $\mathbb{E}[|s|^2] = 1$. The precoded

data vector thus is represented as

$$\mathbf{a}_1 = \eta \mathbf{w} s, \quad (3.5)$$

where \mathbf{w} is the pre-coding vector, which relies on the knowledge on the channel available at the base station. the constant η is a normalization constant in the form of

$$\eta = \sqrt{\frac{1}{\|\mathbf{w}\|^2}}. \quad (3.6)$$

This constant ensures a constant level of energy. Commonly used precoders are the maximum ratio or match filter (MF), the zero-forcing (ZF) and the regularized zero-forcing (RZF) principle. By order, they are as below

$$\mathbf{w}_{\text{MF}} = \eta \mathbf{H}^H, \quad (3.7)$$

$$\mathbf{w}_{\text{ZF}} = \eta \mathbf{H}^H (\mathbf{H} \mathbf{H}^H)^{-1}, \quad (3.8)$$

$$\mathbf{w}_{\text{RZF}} = \eta \mathbf{H}^H (\mathbf{H} \mathbf{H}^H + \alpha \mathbf{I})^{-1}, \quad (3.9)$$

where matrix \mathbf{H} is the complex channel matrix and $\alpha > 0$ is a regularizer factor.

Throughout this work, we chose the maximum ratio transmission (MRF) or MF as the precoder [102]. As it can be noticed in (3.7), through MF precoding, the data symbol s is pre-multiplied by the Hermitian of the channel matrix of the user. MF precoding is robust and has a very low computational complexity and offers high asymptotic performance when it is used in MIMO systems [103], [104].

The basic block chart of the RF beamforming system is presented in Fig. 3.4. The phase of individual antennas is controlled to steer the beam in the direction of UE. For the uniform linear arrays (ULA), the precoded data is implemented by the use of phase shifters. For identical PA behavior across the array, the PA output at the j th transmit antennas, when no crosstalk exists, can be modeled by the Volterra

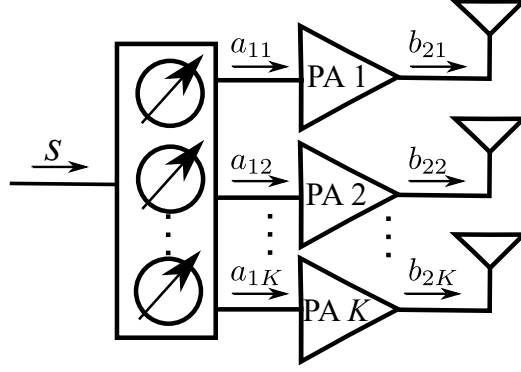


Fig. 3.4 Block diagram of a phased array.

series based model such as the MP model. Therefore, we have

$$b_{2j} = f(a_{1j}), \quad (3.10)$$

where $j = 1, \dots, K$, and $f(\cdot)$ represents the possible nonlinear behavior of each PA in the array. This can be further modeled by an MP model such that

$$b_{2j}(n) = \sum_{m=0}^M \sum_{p=0}^{(P-1)/2} \alpha_{pm} a_{1j}(n-m) \times |a_{1j}(n-m)|^{2p} \quad (3.11)$$

As it is presented in this PA model, each PA output b_{2j} depends solely on its excitation signal a_{1j} , and the model coefficients do not become dependent on the transmitter branch. Therefore, α_{pm} subscript only represents the nonlinearity and memory orders. However, considering the deviation in physical PAs, which can be caused due to the production deviation, aging, and temperature across the array, PAs across the array can have different characteristics. Therefore, a better approach is to assign different models for individual PAs across the array. Subsequently, we have

$$b_{2j} = f_j(a_{1j}). \quad (3.12)$$

By exploiting a MP model we have

$$\begin{aligned}
b_{2j}(n) &= \sum_{m=0}^M \sum_{p=0}^{(P-1)/2} \alpha_{jpm} a_{1j}(n-m) \\
&\times |a_{1j}(n-m)|^{2p}
\end{aligned} \tag{3.13}$$

Here in contrast to the previously explained system model, $f_j(\cdot)$ is a nonlinear function that describes solely the effect of amplification on the PA in the j th transmit path. The $f_j(\cdot)$ can have varying levels of dissimilarity between the branches. Therefore, α_{jpm} subscript represents not only the nonlinearity and memory orders but also the transmitter branch index j .

3.4 Contributions

As can be seen from the literature review, there is an open issue in terms of linearization of the large MIMO systems where the implementation of TOR in each transmit path is cumbersome. A DPD technique is proposed in Chapter 6, which utilizes a few of the embedded receivers of the MIMO TDD transceiver to serve as the OTA-TORs by adopting the intra-transmission model in (3.2). The approach exploits the preexisting hardware in the MIMO TDD system and dispenses the need for TOR per transmitter, therefore reduces the hardware cost and complexity significantly.

We develop this DPD technique in three steps: an OTA effective coupling factor estimation scheme that models the propagation channel and receiver gain, a PA model identification for each transmit paths, and a nonlinear DPD block in every transmit path.

The implementation of TDD transceivers with alternating switches hinders the use of isolators at the antenna since it can block the reception of the signal in receive mode. Hence, the excessive nonlinearity and distortion from crosstalk due to antenna coupling and impedance mismatch must be mitigated. We adopt the dual-input PA model with a linear array model in [97] to compensate for these excessive distortions.

The proposed OTA DPD is evaluated through the measurement of a four-element antenna array. The results are compared to the case when S-parameter measurements replaced the estimated effective coupling within the array, and OTA DPD performs linearization based on the measured S-parameters of the array. To the best of the author's knowledge, this is the first time that measurement results of an OTA DPD are presented for linearization of the individual transmit paths in a TDD MIMO system by exploiting the embedded receiver.

As can be seen from the literature review, there are open issues in the linearization of PAs in phased arrays when the PAs in the different branches possess considerably different characteristics. This issue has been investigated for the work in this thesis. This work is presented based on the system model given in (3.12) and (3.13). In Chapter 7, a comparative study among different single DPD solutions for phased array systems with combined feedback response and with individual PA feedback responses are presented. By proposing a novel single DPD method, a convex optimization problem is formulated, which relies upon on joint minimization of the cost functions from all transmission branches. The simulation results demonstrate that the proposed solution outperforms the ones in [90–94]. This improved performance is especially notable when the PAs in the different branches possess considerably different characteristics. DPD learning technique utilizes a closed-loop estimation technique that is not sensitive to the PA output noisy measurements.

Chapter 4

Digital Predistortion Training for Systems with Antenna Crosstalk

The work presented in this chapter relates to the conference proceeding [105].

In MIMO systems, crosstalk mainly occurs due to coupling effects of signals between the transmission branches [77]. Two main types of crosstalk have been identified based on whether the crosstalk occurs before or after the power amplifiers (PA) in Section 3.1. Crosstalk which occurs before the PAs is subject to the nonlinearity of the PA and therefore is called nonlinear crosstalk. In this chapter, we will focus on the crosstalk which occurs after the PAs, which is known as linear or antenna crosstalk [78]. The fundamental issue with antenna crosstalk is that the distortion caused by this effect occurs in-band. A number of crosstalk cancellation techniques for chip design have been proposed [106] at the cost of current consumption. In other cases the crosstalk is avoided by spacing the channels, isolation between the physical signal paths and differential I/Os which can be used at the expense of increased power consumption and lower data rate [106]. All of these solutions mentioned above also introduce added HW design complexity. It is therefore advantageous if it is possible to compensate for crosstalk effects in the digital hardware already used in the RBS. For this reason, in high power MIMO base stations crosstalk cancellation using digital predistortion (DPD) has become

popular. Crosstalk can be treated as a source of nonlinearity and the existing DPD stage can therefore be adapted to compensate for its effects also.

The memory polynomial (MP) model is widely used for single-input single-output (SISO) PAs. The generalized memory polynomial (GMP) behavioral model introduced in [52], shows excellent accuracy at the cost of additional complexity [29]. A SISO GMP model was adapted in [107] to compensate the linear and nonlinear crosstalk effects in 2×2 MIMO system. The adapted behavioral model for antenna crosstalk was named generalized memory polynomial for linear crosstalk (GMPLC). A similar model to the GMP is the memory polynomial (MP). In this paper a memory polynomial is used to model the distortion of a set of nonlinear PAs combined with antenna crosstalk effects, namely memory polynomial for linear crosstalk (MPLC). The memory polynomial can achieve comparable accuracy, using fewer coefficients compared to the GMP approach. In this way a more computationally efficient approach can be achieved. This is directly beneficial in both the case of modeling MIMO and in particular massive MIMO systems. The same benefits for the MP structure used to model these systems will also apply in its application to DPD.

As explained in Section 2.8.1.2, in calculating the DPD coefficients, two main strategies can be employed, namely direct or indirect learning. Previous studies such as [71, 108] have used the indirect learning architecture to calculate DPD coefficients for a set of nonlinear PAs with crosstalk. Recent studies have shown that direct learning has advantages over the indirect learning architecture when applied to DPD [32, 109]. Therefore, in this section, a comparative study over the DLA and ILA techniques are presented when the system suffers from the antenna crosstalk, and the PA outputs are protected from the incident wave by using isolators.

4.1 MIMO System Models With Antenna Crosstalk

Antenna crosstalk or linear crosstalk is the effect of signal coupling which occurs between the antennas in the array. When the isolators are placed between the PA output and the antenna, the effect of crosstalk does not directly affect the

PA behaviors individually. Because the crosstalk terms after the PA do not pass through a nonlinear component in the RF front-end, this type of coupling effect is considered antenna crosstalk. As a result, the impairment effects will appear as in-band distortion [77] and as a result, will increase the NMSE of the signal, which is fed to the antenna. In Fig. 4.1 the mechanism by which antenna crosstalk occurs is shown. The effect of antenna crosstalk is depicted in this figure where ξ and ϱ are impulse responses of the linear filters, and specify the strength of the crosstalk. It can be seen that some proportion of the signal in each path is transferred to the adjacent signal path. Not only will there be antenna crosstalk between the transmitter paths, but there is also crosstalk in the channel and crosstalk between the receiver antennas. Compensation of all of these crosstalk effects can be compensated for in the receiver. However, if the transmitter antenna crosstalk can be compensated prior to signal transmission, the overall performance of the MIMO system will be improved [110]. Considering this fact, it is advantageous to compensate for the linear or antenna crosstalk in the transmitter DPD prior to transmission.

It is worth noticing that unlike effective coupling, the antenna crosstalk does not exhibit reciprocal characteristics. Therefore, the antenna crosstalk is indicated with different symbols from the first transmit path, and the second transmit path toward the victim transmit branches. Similar to the antenna crosstalk model presented in [77] and [107], the antenna crosstalk can be formulated as follows

$$b_{21}(n) = f_1(a_{11}(n)) + \xi * f_2(a_{12}(n)) \quad (4.1a)$$

$$b_{22}(n) = f_1(a_{11}(n)) + \varrho * f_2(a_{12}(n)). \quad (4.1b)$$

When ξ and ϱ are set to zero, the 2×2 MIMO system can be modeled as a single-input single-output (SISO) system.

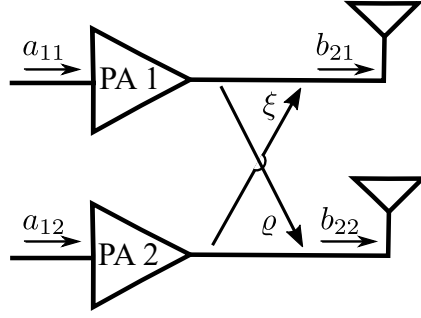


Fig. 4.1 Antenna crosstalk in MIMO transmitter.

In this model, $f_1(\cdot)$ is a function representing the nonlinearity effects in branch one, and $f_2(\cdot)$ is the function representing the nonlinearity effects in the second branch. By modeling the crosstalk effect in this way, the output of the antenna will be a linear combination of the nonlinear effects from its reference branch and a factor of nonlinear effects from the second branch. Accordingly, no cross-terms are needed to model the coupling effect of antenna crosstalk. The nonlinearities are modeled separately. Therefore, any conventional SISO model can be used to replace each of f_1 and f_2 functions.

4.2 PA Behavioral Modeling and DPD with Antenna Crosstalk

When the crosstalk is memoryless, i.e., frequency-independent, by adopting the MP model to represent the PA SISO model, (4.1) can be represented as

$$\begin{aligned}
 b_{21}(n) = & \sum_{m_1=0}^{M_1} \sum_{p_1=0}^{(P_1-1)/2} \alpha_{1p_1m_1} a_{11}(n-m_1) \times |a_{11}(n-m_1)|^{2p_1} \\
 & + \xi \sum_{m_2=0}^{M_2} \sum_{p_2=0}^{(P_2-1)/2} \alpha_{2p_2m_2} a_{12}(n-m_2) \times |a_{12}(n-m_2)|^{2p_2}
 \end{aligned} \tag{4.2a}$$

$$\begin{aligned}
 b_{22}(n) = & \rho \sum_{m_1=0}^{M_1} \sum_{p_1=0}^{(P_1-1)/2} \alpha_{1p_1m_1} a_{11}(n-m_1) \times |a_{11}(n-m_1)|^{2p_1} \\
 & + \sum_{m_2=0}^{M_2} \sum_{p_2=0}^{(P_2-1)/2} \alpha_{2p_2m_2} a_{12}(n-m_2) \times |a_{12}(n-m_2)|^{2p_2},
 \end{aligned} \tag{4.2b}$$

4.2 PA Behavioral Modeling and DPD with Antenna Crosstalk

where the vectors $\boldsymbol{\alpha}_1$ and $\boldsymbol{\alpha}_2$ contain all the instances of $\alpha_{1p_1m_1}$ and $\alpha_{2p_2m_2}$, respectively. It is assumed that the two input signals, a_{11} and a_{12} , have the same center frequency. Because crosstalk is memoryless, by distributive law, the equations in (4.2) are transformed to

$$b_{21}(n) = \sum_{m_1=0}^{M_1} \sum_{p_1=0}^{(P_1-1)/2} \alpha_{1p_1m_1} a_{11}(n-m_1) \times |a_{11}(n-m_1)|^{2p_1} \\ + \xi \sum_{m_2=0}^{M_2} \sum_{p_2=0}^{(P_2-1)/2} \tilde{\alpha}_{2p_2m_2} a_{12}(n-m_2) \times |a_{12}(n-m_2)|^{2p_2} \quad (4.3a)$$

$$b_{22}(n) = \varrho \sum_{m_1=0}^{M_1} \sum_{p_1=0}^{(P_1-1)/2} \tilde{\alpha}_{1p_1m_1} a_{11}(n-m_1) \times |a_{11}(n-m_1)|^{2p_1} \\ + \sum_{m_2=0}^{M_2} \sum_{p_2=0}^{(P_2-1)/2} \alpha_{2p_2m_2} a_{12}(n-m_2) \times |a_{12}(n-m_2)|^{2p_2}, \quad (4.3b)$$

where the vector $\tilde{\boldsymbol{\alpha}}_1$ is the combination of memory less antenna crosstalk ϱ and the vector $\boldsymbol{\alpha}_1$. In the same manner, the vector $\tilde{\boldsymbol{\alpha}}_2$ is the combination of memory less antenna crosstalk ξ and the vector $\boldsymbol{\alpha}_2$. Therefore, to identify the PA model, the parameters $\boldsymbol{\alpha}_1$, $\boldsymbol{\alpha}_2$, ξ and ϱ are redundant and no need to estimate them separately [107].

4.2.1 DPD Learning Algorithm with Antenna Crosstalk

In Section 2.8.1, two DPD identification techniques were presented, i.e., ILA and DLA. In ILA technique, the DPD coefficients to be estimated are

$$\tilde{\boldsymbol{\alpha}}_{j(\text{ILA})} = \Phi(\mathbf{b}_{2j})^\dagger \mathbf{a}_{1j}. \quad (4.4)$$

Formation of the basis functions based on the measured PA output, $b_{2j}(n)$ in the DPD coefficient estimation, is a primary source of instability in using the ILA method. The inherent noisy measure of PA output signal, results in the uncertainty

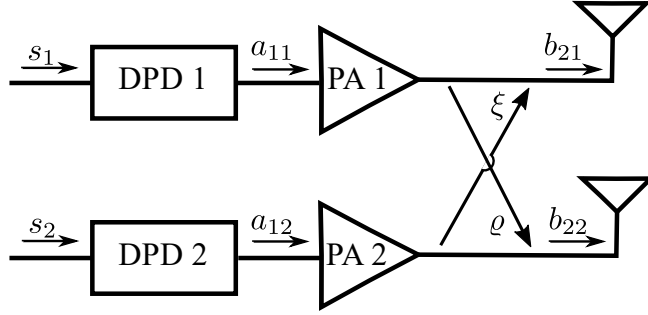


Fig. 4.2 MIMO transmitter and DPD block diagram in presence of antenna crosstalk.

in the estimated values of the DPD coefficients. In contrast, the DLA method directly uses the input and output signals in the approximation of the coefficients.

$$\Delta \tilde{\alpha}_{j(\text{DLA})} = \Phi(\mathbf{s}_{1j})^+ \mathbf{e}_j, \quad (4.5)$$

where $\mathbf{e}_j = \mathbf{s}_{1j} - \mathbf{b}_{2j}$. Then, the DPD parameters are updated as

$$\tilde{\alpha}_{j(\text{DLA})}^{i+1} = \tilde{\alpha}_{j(\text{DLA})}^i + \Delta \tilde{\alpha}_{j(\text{DLA})} \quad (4.6)$$

where $\tilde{\alpha}_{j(\text{DLA})}^i = [1, 0, \dots, 0]$. Since, the basis functions $\Phi(\mathbf{x})$ are formed based on the input signal \mathbf{s}_j , this technique is less sensitive to measurement noise.

In the presence of antenna crosstalk, the PA output signal b_{2j} will be distorted by the antenna crosstalk effect from the adjacent branch PA output. This additional component will serve to create another degree of uncertainty in the estimation of the DPD coefficients with the ILA technique.

4.3 A Comparative Study of DLA and ILA with Antenna Crosstalk

In order to compare the performance of DLA and ILA coefficient estimation in the presence of antenna crosstalk, a simulation is carried out over a 2×2 MIMO model where two branches have two identical PAs. A long-term evolution (LTE) single-carrier signal with the bandwidth of 20 MHz is used with the number of samples for

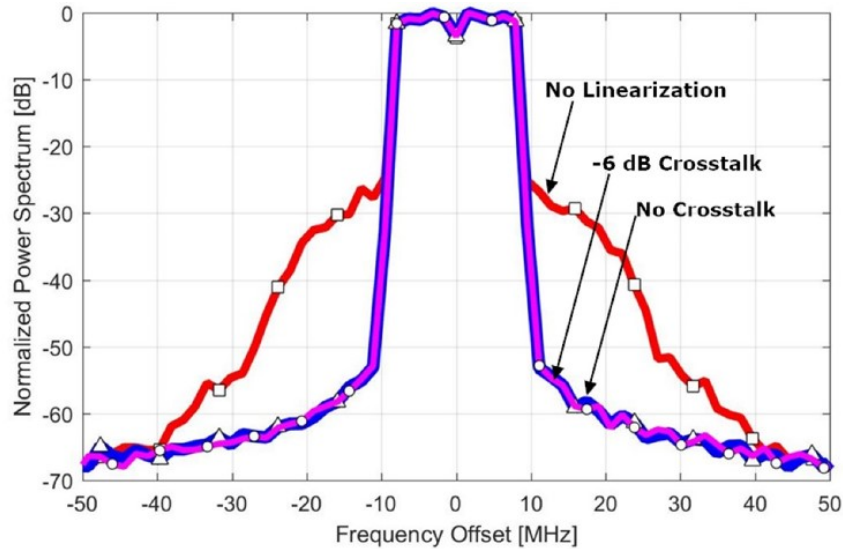


Fig. 4.3 PA output spectrum when no linearization was applied, PA output with linearization in presence of no crosstalk and -6 dB crosstalk.

each signal sets to 100000 samples and the signals sampled by the sampling rate of = 208 MHz. An additive white Gaussian noise is added at the output of the PA, which leads to a signal to SNR of 65 dB. Both PAs are set to have similar nonlinearity order and memory depth of $P = 4$ and $M = 9$. For the above signals, this model gives an NMSE equal to -48 dB and an ACPR of -57.73 dB.

Fig. 4.3 shows the spectrum of PA output without any linearization technique be implemented. Then the spectrum of PA output with linearization technique presented when a) there is no crosstalk and b) in the presence of -10 and -6 dB antenna crosstalk. When the linearization technique is used, the out-of-band characteristics of spectrum in case a and b are very similar. To compare the relative performance of the ILA and DLA, the antenna crosstalk figures of -6 dB and -10 dB are considered in this work. In Table. I, the NMSE, provided in the presence of no crosstalk, -6 dB antenna crosstalk, and -10 dB antenna crosstalk when the DLA and ILA used for DPD coefficient estimation. In the absence of antenna crosstalk, the NMSE obtained using the ILA method, which is comparable to that achieved using the DLA method.

By adding the effect of crosstalk, the DLA method maintained the same NMSE performance, which it achieved without crosstalk. However, repeating the same procedure for the ILA method, the NMSE increased considerably, first to -37.7 dB

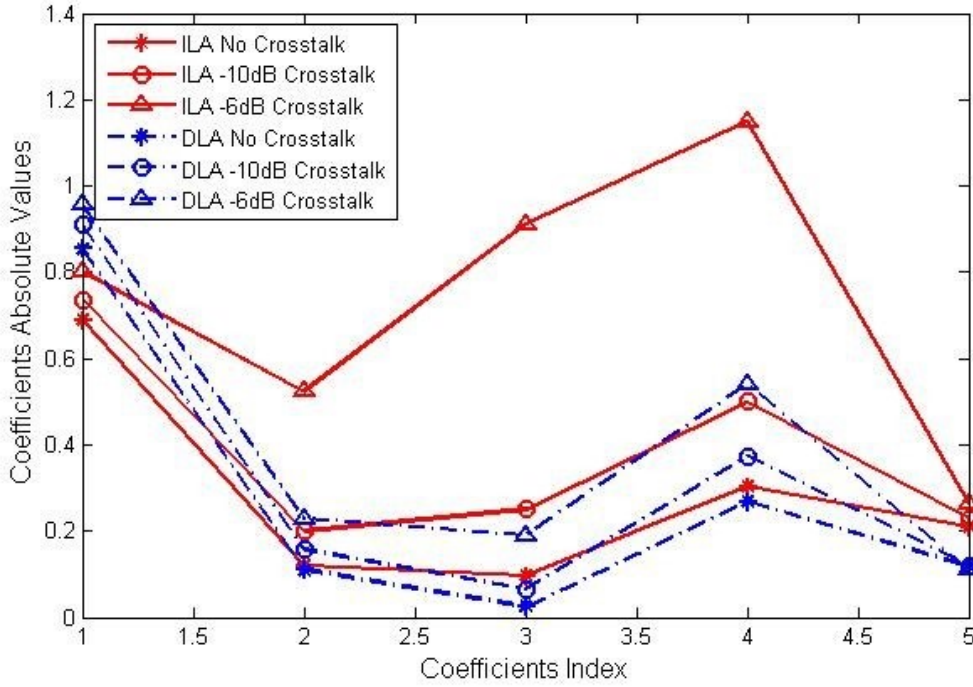


Fig. 4.4 Coefficients Divergence in DLA and ILA in presence of no crosstalk, -10 dB antenna crosstalk and -6 dB antenna crosstalk.

and then to -22.2 for -6 dB and -10 dB crosstalk. In all three cases, by using the DLA method to estimate the DPD coefficients, a lower NMSE was obtained.

As discussed in Section 4.2.1, the ILA method uses two signals, which are themselves estimations of the desired predistorted signal and post-distorted signals. DLA, on the other hand, uses the original input signal and the measured output signal directly to calculate the predistorter coefficients. In Fig. 4.4, a random selection of the DPD coefficients are presented for both DLA and ILA methods in the presence of different amounts of antenna crosstalk.

Table 4.1 NMSE [dB] for different antenna crosstalk in a 2×2 MIMO transmitter using DLA and ILA techniques.

Learning Algorithm	No Crosstalk	Antenna Crosstalk -10 dB	Antenna Crosstalk -6 dB
DLA	-45.6	-45.6	-42.0
ILA	-43.2	-37.7	-22.2

It can be seen from Fig. 4.4 that by the separation of the lines that the coefficients calculated with the ILA method fluctuate more than those calculated using the DLA method. These observations closely resemble the improved NMSE performance of DLA in comparison to the ILA.

The measured results demonstrate the improved performance of DLA estimation in comparison to ILA estimation. In the presence of crosstalk, the DLA method can maintain excellent NMSE performance. In contrast to the ILA method where it can be seen the NMSE performance degrades considerably in the presence of antenna crosstalk.

4.4 Conclusion

In this chapter, two different estimation methods were evaluated for the calculation of DPD coefficients for systems that include crosstalk. These methods were applied to a antenna crosstalk cancellation of a 2×2 MIMO transmitter. The MPLC was used to model the nonlinearity in the transmitter and used in the DPD implementation. NMSE is used to present the relative performance of the two methods. The measured results demonstrate the improved performance of DLA estimation in comparison to ILA estimation. In the presence of crosstalk the DLA method can maintain good NMSE performance. In contrast to the ILA method where it can be seen the NMSE performance degrades considerably in the presence of antenna crosstalk.

Chapter 5

Intra Array Coupling Estimation

The work presented in this chapter relates to the conference proceeding [111].

Large-scale MIMO arrays are typically deployed with high integration and using low-cost components, and hence, they are prone to different hardware impairments such as cross-talk between the transmit antennas and power amplifier (PA) nonlinearities which distort the transmitted signal. In order to avert the performance degradation due to these impairments, it is essential to have mechanisms for predicting the output of the MIMO arrays. Such prediction mechanisms are mandatory for performance evaluation and more importantly, for the adoption of proper compensation techniques such as digital predistortion (DPD) schemes [112].

In conventional MIMO systems, the prediction mentioned above is carried out with the aid of bulky couplers which feed the transmitted radio frequency (RF) signal in each branch to observation receivers [113]. However, in large-scale MIMO systems with up to several hundreds of transmission paths, employing conventional observation receivers with couplers would be overly expensive and too complicated for implementation. This has motivated attempts for alternative solutions, one of which is the use of over-the-air (OTA) observation receivers. For instance, the authors in [86] propose a DPD technique for linearizing the analog beamforming array by relating the far-field received signal at the observation receiver antenna to the input signal to the array. For general spatial multiplexing MIMO systems (i.e., where

different data streams are transmitted at different antennas), OTA measurement-based modeling of the array is a more complex task. Hausmair *et al.* [89] introduce a solution where a few observation receivers are placed at the array performing the OTA measurements whose received signals are used for extracting the PA models and accordingly, identifying the DPD coefficients. However, this solution relies on the assumption that the propagation channel between the transmitter antennas and the observation receivers are known. As an extension to the scheme proposed in [89], in this chapter, we introduce a novel intra-array coupling estimation technique. We consider an array of transceivers where at each transceiver, both the transmitter and receiver are connected to the same antenna port (see Fig.5.1). Our proposed technique relies on reciprocity of propagation channels in time-division duplex (TDD) mode where coupling coefficients are estimated via consecutively transmitting from different antennas and receiving the signals by the other antennas. We validate the effectiveness of the proposed solution experimentally by comparing the estimated coupling coefficients with antenna S-parameters. The proposed technique serves as an on-the-fly estimation approach, and since the impedance mismatch and reflection effects are taken into account, it provides a more accurate characterization of the couplings with respect to the S-parameters. As a result, the estimated intra-array couplings facilitate practical modeling and linearization of the arrays using OTA measurements.

In this chapter, a framework for estimating the effective coupling between antenna elements in a MIMO TDD system is developed. Then, the estimated couplings are used in Chapter 6 to identify the PA models and to perform the linearization using OTA measurements.

5.1 Proposed Effective Coupling Estimation

The effective coupling estimation method is based on the concept of the common transmitter when one of the transceivers in the array is set to transmit mode while

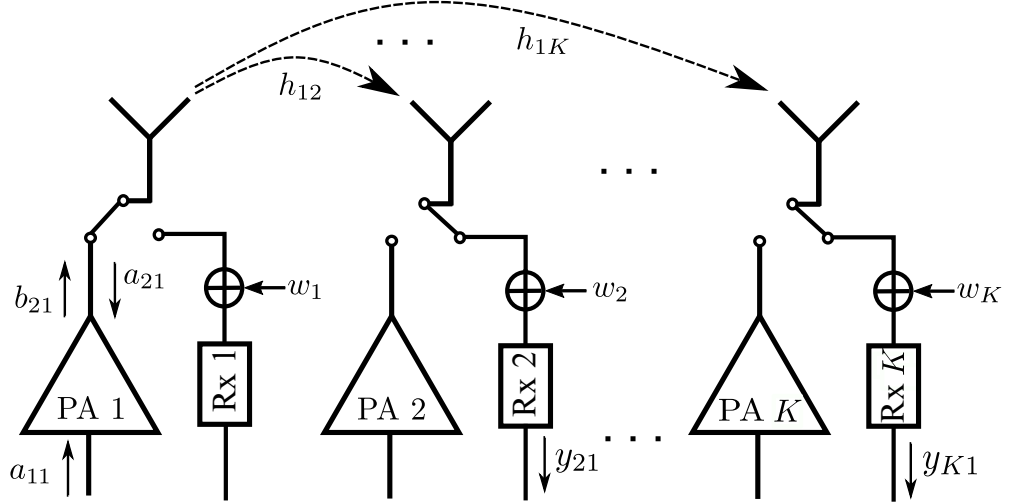


Fig. 5.1 Block diagram of a MIMO system with K transceivers with one transceiver in transmit mode while the rest of the array elements are receiving in presence of crosstalk.

the rest of the transceivers within the same array are set to operate in receive mode. This scheme is depicted in Fig. 5.1.

For a noiseless observation, when the j th antenna transmits, and i th and p th antennas receive, the following equation holds based on (3.1)

$$\mathbf{y}_{ij}c_{ij} = \mathbf{y}_{pj}c_{pj}, \quad i, p \neq j, \quad (5.1)$$

where

$$c_{ij} = 1/(r_i h_{ij}). \quad (5.2)$$

As it was stated earlier, we set the effective coupling as $\lambda_{ij} = r_i h_{ij}$. Thus, an inherent approach to estimate the λ_{ij} is to estimate c_{ij} . When the observation is noisy, a general approach is to minimize the following cost function

$$J(\mathbf{c}_j) = \sum_{i,p=1}^K \|\mathbf{y}_{ij}c_{ij} - \mathbf{y}_{pj}c_{pj}\|^2, \quad i, p \neq j, \quad (5.3)$$

for the j th transmitter, where $\mathbf{c}_j = [c_{1j}, \dots, c_{Kj}]$ excluding the term c_{jj} [114], and $\|\cdot\|$ denotes the Frobenius norm.

Intra Array Coupling Estimation

Algorithm 1 Coupling Coefficients *Single Estimation*

Require: pilot signals $\mathbf{a}_{11}, \dots, \mathbf{a}_{1K}$, measured received signals \mathbf{y}_{ij} .

Initialization: set $i = 1$, set the reference antenna as common transmitter and find c_{1r} , set $\tilde{c} = c_{1r}$.

while all the coupling coefficients are identified **do**

 set i th antenna as common transmitter

 build matrix $\Psi_{(\text{single})}^{(i)}$

 find $\hat{\mathbf{c}}_i$ from (5.7)

 set $\tilde{c} = \hat{\mathbf{c}}_i(1)$

$i = i + 1$

end while

Output: Intra-array coupling coefficients

In a TDD system, reciprocity of the propagation channel in channel coherence time, i.e., $h_{ij} = h_{ji}$, enables the estimation of an effective coupling. To further exploit the reciprocity in estimation of c_{ij} and subsequently λ_{ij} , we assume that the receiver characteristics are identical.

The key concept for the proposed reciprocity-based mutual coupling estimation in a large-scale MIMO transmitter is to ensure that the RF chain of the radio used in the hardware implementation of the receiver path does not hinder the reciprocity of coupling coefficients. The assumption for the identical characteristics of the receivers is essential since the estimated c_{ij} in each step must be used in the form of c_{ji} in the next step of our proposed estimation technique. If reciprocity of $r_i h_{ij}$ is valid, the c_{ji} is available once c_{ij} is estimated. However, in the real physical setup, the assumption of identical receivers does not hold. The effect of variation of receiver characteristics on the accuracy of estimated couplings is discussed in [111] where a model was developed to relate the non-identical receiver gains with the accuracy of the estimated couplings. The results indicate a strong correlation between the receiver non-identical gains and degradation in the accuracy of the estimated couplings. Such differences in RF receiver chain are statistical differences in the manufactured units, which result in receiver gain variations. However, the receivers across the array are supported with automatic gain controls (AGCs) to counterpoise the receiver gain variation emerging from device production processing

variation, temperature, and voltage deviations [115]. Therefore, the assumption for identical receiver characteristics is valid. In Section 6.5, we repeat a method of *Direct Measurement* to further validate this assumption in our test bench before performing the PA identification and linearization.

The solution to (5.3) is extracted up to a multiplicative constant. By utilizing a reference transceiver with measured transmit characteristics, f_r , the effect of this uncertainty can be lifted. Nonetheless, the geometry of the antenna array and the placement of the reference antenna in regard to the array elements has a direct effect on the coupling estimation precision. For those antenna elements further away from the reference antenna, the received signal from the reference antenna can get masked by the receiver noise. Hence, we propose two different methods for our estimation approach based on the configuration of the array and the placement of the reference antenna as follows.

5.1.1 Single Estimation

The first method referred to as *Single Estimation*, which provides essential communication between the reference antenna and the array in linear array structures. The number of adjacent receivers to the reference antenna is limited in the linear array due to its geometry (Fig. 5.2a). Thus, the sequential operation of the *Single Estimation* method makes it well suited for the linear antenna array structure. The *Single Estimation* method is carried out in two steps.

5.1.1.1 Reference Coupling Estimation

We introduce a reference transceiver within the array, e.g., TRX_r with known transmitter characteristic, i.e., f_r . The closest antenna element to the reference antenna, i.e., TRX₁, is set to receive mode. By listening to the transmitted signal, \mathbf{a}_{1r} from the reference transceiver, parameter c_{1r} can be estimated directly by minimizing a linear least squares (LS) cost function. Then, by reciprocity, we have $c_{1r} = c_{r1}$.

5.1.1.2 Intra-Array Coupling Estimation

Starting from TRx₁, sequentially set a common transmitter and estimate the intra-array coupling coefficients by following these steps. Having TRx₁ as a common transmitter, the rest of the transceivers listen to TRx₁, including TRx_r. Then, we form the cost function $J(\mathbf{c}_1)$ based on the definition in (5.3). The cost function $J(\mathbf{c}_j)$ is a real-valued function of parameters c_{ij} and c_{ij}^* , where $(\cdot)^*$ denotes conjugate. Thus, the optimal solution can be found by setting the partial derivative with respect to c_{ij}^* to zero and treating c_{ij} as an independent variable [116]. In other words, for the j th common transmitter, by solving

$$\frac{\partial J(\mathbf{c}_1)}{\partial c_{i1}^*} = 0, \quad \forall i = 2, \dots, K, \quad (5.4)$$

the optimal estimation of \mathbf{c}_1 is obtained, where $\mathbf{c}_1 = [c_{r1}, c_{21}, \dots, c_{K1}]^T$. In matrix form, this can be written as

$$\mathbf{\Psi}_{(\text{single})} c_1^{(1)} = 0. \quad (5.5)$$

The matrix $\mathbf{\Psi}_{(\text{single})}^{(i)} \in \mathbb{C}^{M \times M}$ ($M = K$), is presented in Appendix A.

The term c_{r1} is already estimated from step 5.1.1.1. Thus, we rewrite (5.5) in the following form

$$[\psi | \hat{\mathbf{\Psi}}] [c_{1r} | \hat{\mathbf{c}}_1]^T = 0, \quad (5.6)$$

where ψ is the first column of $\mathbf{\Psi}_{(\text{single})}^{(1)}$ and contains the multiplicatives of c_{1r} . The vector $\hat{\mathbf{c}}_1 = [c_{21}, \dots, c_{K1}]^T$, and $(\cdot)^T$ denotes transpose. The array of parameters, \mathbf{c}_1 , can be solved as a function of c_{1r} , allowing for an absolute estimation of \mathbf{c}_1 . We make a note here that, by excluding the reference transceiver, a constrained relative solution for $\hat{\mathbf{c}}_1$ can still be defined. However, for the application of estimated couplings in PA linearization in presence of signal \mathbf{a}_{2j} , the absolute estimate of $\hat{\mathbf{c}}_1$ is imperative.

Solving (5.6) for $\hat{\mathbf{c}}_1$ provides

$$\hat{\mathbf{c}}_1 = -(\hat{\Psi}^H \hat{\Psi})^{-1} \hat{\Psi}^H \psi \tilde{c}, \quad (5.7)$$

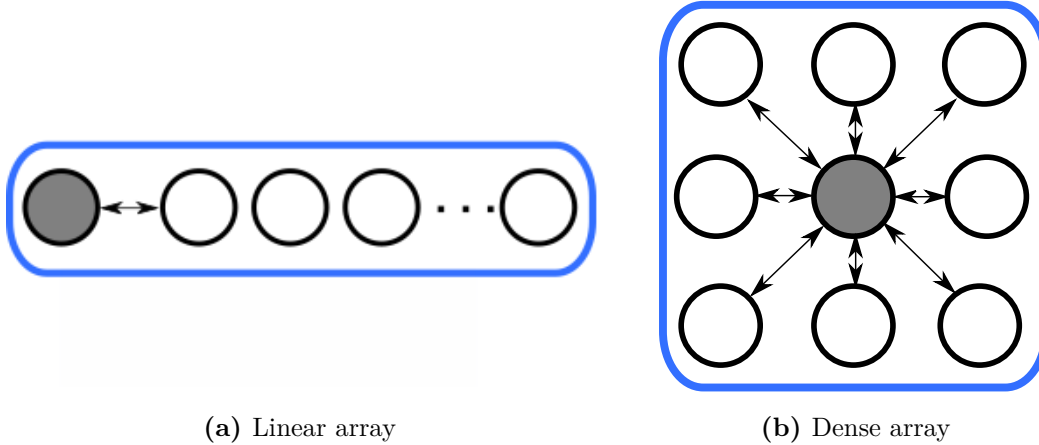
where $\tilde{c} = c_{1r}$ and $(\cdot)^H$ denotes Hermitian transpose. Through this step, the coupling coefficients between the first antenna and the rest of the antenna elements are identified and any one of the remaining antennas can be set as a common transmitter. Therefore, while the i th antenna acts as a common transmitter, the coupling coefficient c_{1i} , which is obtained in the first step, acts as the reference coupling. Since each of the solutions depend on the previous estimates, the steps must be repeated iteratively, by sequentially setting the common transmitters. This procedure is repeated until all couplings are identified. Algorithm 1 summarizes the proposed iterative *Single Estimation* method.

The size of matrix Ψ_{single} dominates the computational complexity of this method which is proportional to the size of the array. On a practical note, we remark that to have a moderate level of complexity, different methods of clustering can be used to limit the number of antenna elements in each iteration. A thorough description of the clustering technique can be found in Section 5.1.3.

The inherent problem in the calculation of c_{1r} by a LS approach is that numerical error in the calculation can propagate and add up throughout the array coupling estimation. The error can occur due to the noise in the measurements or dissimilarity among the receiver characteristics. However, the particular structure of more dense arrays such as rectangular arrays suggests that a pragmatic approach for estimating the coupling coefficients can be pursued. Thus, we propose the *Joint Estimation* technique.

5.1.2 Joint Estimation

In dense array structures, as depicted in Fig.5.2b, the reference antenna can be placed in close proximity to several antennas, the reference couplings \mathbf{c}_r for several antennas can be obtained. In this part, we provide a robust and computationally



(a) Linear array

(b) Dense array

Fig. 5.2 Identifying the reference coupling based on the reference transceiver position within the array. The gray circle indicates the reference antenna.

efficient technique to jointly find the estimation of matrix \mathbf{C} where \mathbf{C} stacks all vectors of \mathbf{c}_i into a matrix \mathbf{C} in one iteration where $\mathbf{C} = [\mathbf{c}_r^T, \mathbf{c}_1^T, \dots, \mathbf{c}_K^T]^T$.

5.1.2.1 Joint Reference Coupling Estimation

The reference couplings \mathbf{c}_r for several antennas can be obtained by having the reference antenna as the common transmitter while all other antenna elements are listening. In this way a similar strategy as Section 5.1.1.1 is used. By listening to the transmitted signal, \mathbf{a}_{1r} from the reference transceiver, parameters $\mathbf{c}_r = [c_{1r}, c_{2r}, \dots, c_{Kr}]$ can be estimated directly by minimizing a linear least squares cost function. Then, by reciprocity, we have parameters $c_{r1}, c_{r2}, \dots, c_{rK}$.

5.1.2.2 Intra-Array Coupling Estimation

In this step, we set each antenna element in the array as the common transmitter. Instead of pursuing an approach similar to the one used in the *Single Estimation* technique, the *Joint Estimation* has its roots in minimization of a superposition of individual cost functions in (5.3), formed from the collected received signals which follows

$$J_{\text{tot}}(\mathbf{C}) = \sum_{j=1}^K J(\mathbf{c}_j). \quad (5.8)$$

5.1 Proposed Effective Coupling Estimation

As for *Single Estimation*, by setting the partial derivative of $J_{\text{tot}}(\mathbf{C})$ with respect to individual c_{ij}^* to zero and treating c_{ij} as an independent variable the global optimum is obtained. In other words, by solving

$$\frac{\partial J_{\text{tot}}(\mathbf{C})}{\partial c_{ij}^*} = 0, \quad \forall i, j = r, 1, \dots, K \quad i \neq j, \quad (5.9)$$

the optimal estimation of \mathbf{C} can be found. In matrix form, this can be written as

$$\Psi_{(\text{joint})} \mathbf{C} = 0, \quad (5.10)$$

where the matrix $\Psi_{(\text{joint})} \in \mathbb{C}^{2M \times M}$ for $M = K(K-1)/2$, is presented in Appendix B. We solve

$$\hat{\mathbf{C}} = -(\hat{\Psi}_2^H \hat{\Psi}_2)^{-1} \hat{\Psi}_2^H \hat{\Psi}_1 \mathbf{c}_r, \quad (5.11)$$

where $\hat{\mathbf{C}} = [\mathbf{c}_1, \dots, \mathbf{c}_K]^T$ and $\hat{\Psi}_1$ is a matrix which contains the first $(K-1)$ columns of $\Psi_{(\text{joint})}$, and the rest of the columns of $\Psi_{(\text{joint})}$ form the matrix $\hat{\Psi}_2$.

The side remarks regarding the application of the above-stated estimation techniques follow. We take advantage of several reference coupling coefficients which contribute simultaneously to the solution for $\hat{\mathbf{C}}$. Thus, the possible numerical error in the estimation of reference coupling via the LS approach can average out, resulting in a robust solution in contrast to the previously mentioned *Single Estimation*. Furthermore, it can be noticed that the matrices to be inverted in (5.7) and (5.11) are constructed directly from the measured signals. This is favorable since no estimated term and estimation error contributed to the matrix formation which can guarantee a low condition number. Noticeably, this feature makes the proposed techniques robust, when the matrix inversion is required.

5.1.3 Clustering

In Section 5.1.2.2, we proposed a clustering method to reduce the computational complexity of *Single Estimation* technique. However, the clustering technique is useful in other cases.

A low signal-to-noise ratio (SNR) at the receiver restricts the achievable precision of the stated coupling estimation, which results in limited accuracy of PA model extraction and limits the achievable linearization performance. Low SNR can be a problem for transmit antennas distant from the receiver antennas since the magnitude of the coupling coefficients are small for these transmitters. Hence, signals originating from these antennas can get masked by the noise.

In order to overcome this problem, we propose to perform a clustering technique that becomes attractive to estimate the couplings in large-scale arrays, which relies on a sequential coupling estimation for each cluster. In a simple case, we perform the coupling estimation for an array with eight elements. The structure of the array is depicted in Fig. 5.3. The procedure involves first splitting the array in a sufficiently small-size cluster, where all of the antenna elements within the array have strong coupling with each other.

The first cluster must contain the reference antenna, i.e., gray circle in Fig. 5.3. Then, we use the technique of the previous section to identify the couplings within the first cluster. We make a note here that either method of *Single Estimation* or *Joint Estimation* can be used to identify the intra-cluster coupling coefficients. Next, the second cluster performs the intra-cluster coupling estimation with an exception. When the first element in the second cluster is in the common transmitter mode, one inter-cluster transmission is performed where an antenna element in the first cluster which is in the closest proximity of the radiating element is receiving. A visual interpretation of the inter-cluster transmission is shown in Fig. 5.3e. The reason for including the inter-cluster transmission is to guarantee the absolute estimation of the coupling across the whole array. Because the reference antenna only presents within the first cluster, the advantage of providing an absolute estimate of coupling

is only provided to the elements within its cluster. Therefore, to take advantage of its presence, inter- cluster transmission is performed once for the second cluster. The procedure continues by performing the inter transmission between the second and the third cluster, and so on.

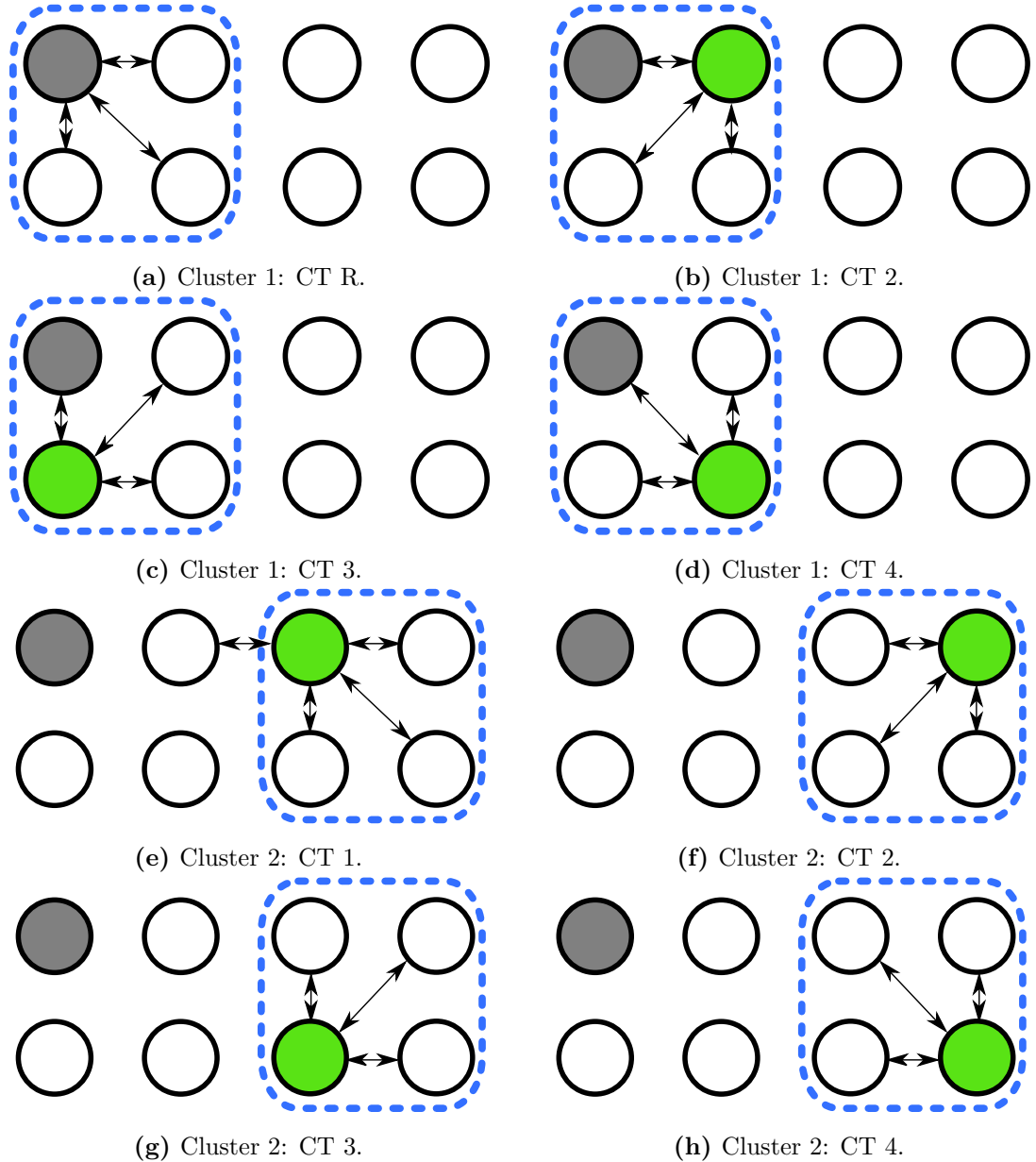


Fig. 5.3 Clustering technique. Two clusters are identified where each cluster contains four antenna elements. The broken blue line indicates the active cluster. The gray circle indicates the reference (R) antenna in the first cluster. The green circle indicates the common transmitter (CT).

5.1.4 Complexity Analysis

Generally, the estimation of couplings in (5.7) and (5.11) requires a Hermitian matrix inversion. Thus, for a $M \times M$ matrix, the complexity order is $O(M^3)$. For a K elements antenna array, the *Single Estimation* technique requires $K - 1$ iterations. In the i th iteration, the dimensions of matrix $\Psi_{\text{single}}^{(i)}$ reduce to $(M - i) \times (M - i)$, where $M = K$. Thus, the complexity of each iteration in *Single Estimation* is dominated by the size of the Ψ_{single}^i in that iteration. Alternatively, for very large linear arrays, the size of the $\Psi_{\text{single}}^{(i)}$ can be adjusted by clustering the antenna elements in step 2, i.e., *Intra-Array Coupling Estimation*.

As for the *Joint Estimation* technique, only one iteration is required to obtain the coupling coefficients. However, for an array with K antenna elements, the dimensions of Ψ_{joint} are $2M \times M$ where $M = K(K - 1)/2$, which are larger compared to the *Single Estimation*.

We make a note that although the linearization is performed regularly, the coupling estimation does not need to be repeated as often. Thus, the order of complexity in both approaches does not hinder the application in a real base station setup. The sequential transmission of the antenna elements may require an interruption of data traffic. However, it is possible to perform the estimation once, when the traffic through it is low. Manufacturers already implemented features in the radio base stations (RBSs) based on the fact that there are times that the RBS does not have any data traffic in place [117].

5.1.5 Performance Assessment

The simulations are performed for a 4×4 rectangular array with patch antennas as in Fig. 5.4 at center frequency of 2.12 GHz. The characteristics of the PAs connected to each antenna element are conducted from measurements of a class AB PA (BLP7G22S-10P) based on the complex polynomial model of order $P = 5$ and $M_1 = M_2 = 2$. The PA models in adjacent transmitters are obtained by adding several perturbations to the measured PA coefficients. Therefore, different

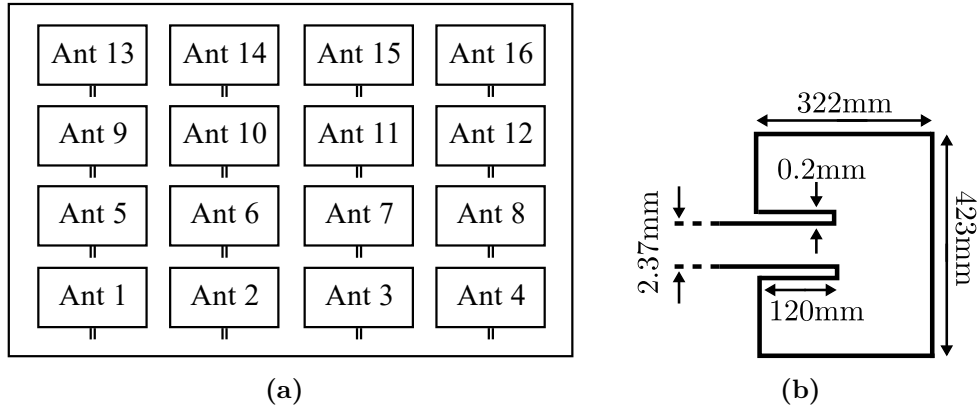


Fig. 5.4 The layout of the 4×4 array is given in (a), the dimensions of a single patch antenna are given in (b).

PA behaviors are achieved, where the nonlinearity characteristics and linear gains of all PAs are in the same order.

The array characteristics are simulated with Keysight Advanced Design System Momentum and S-parameters are obtained. We select FR4 substrate with dielectric constant $\epsilon_r = 4.4$, thickness of 62 mil and $\tan \delta = 0.02$ and element spacing of 0.35 wavelength.

5.1.5.1 Simulation Setup for the Effective Coupling Estimation and Results

In this part, the performance of an effective coupling estimation technique is evaluated. The reference transceiver index is set to $\text{ref} = 10$, which is one of the central elements of the array. The clustering technique explained in Sec. 5.1.3 is used to reduce the inaccuracy of received signals in the low SNR, when the transmit and receive antennas are not in close proximity. The simulation is repeated for different SNR values, and the results are presented in Fig. 5.5. For brevity, the number of presented estimated effective couplings is limited but covers different vertical, horizontal, and diagonal spacing of antenna elements. The SNR of 40 dB, as can be seen from Fig. 5.5, appears to be a region where the NMSE of estimated λ_{ij} value converge regardless of the antenna spacing.

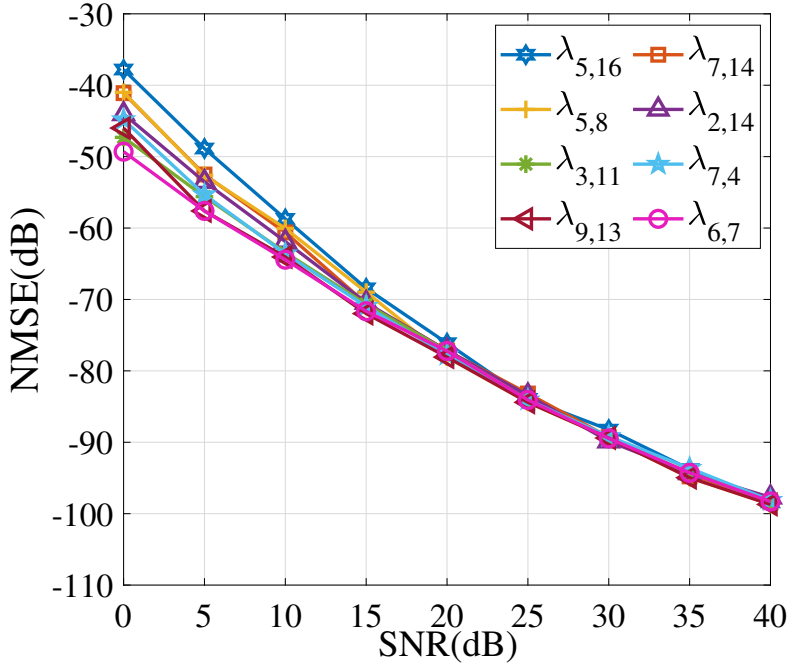


Fig. 5.5 NMSE of the estimated $\lambda_{i,j}$ versus SNR in a 4×4 array.

5.2 Experimental Validation

In this section, the measurement setup for a four-element antenna array MIMO system is presented to validate the proposed effective coupling estimation technique. Then, the results and comparisons are presented in Section 5.3.

The experimental task is performed in two steps. First we present a setup to estimate the effective coupling. Furthermore, in this experiment the effect of the number of reference coupling on the estimated effective couplings is studied. Second, we perform the linearization technique utilizing OTA measurements, using the estimated effective couplings and the S-parameters.

For the experimental validation, OFDM test signals with 5 MHz bandwidth were generated in MATLAB. The signals have a peak-to-average power ratio (PAPR) of 8.5 dB. This bandwidth is wide enough to capture the dynamic effects of the PAs. A signal generator (Agilent ESG4433B) was used to synthesize the driving signal. To effectively characterize the effective coupling, a four-element rectangular patch antenna array was designed for resonant frequency of 2.12 GHz and manufactured with

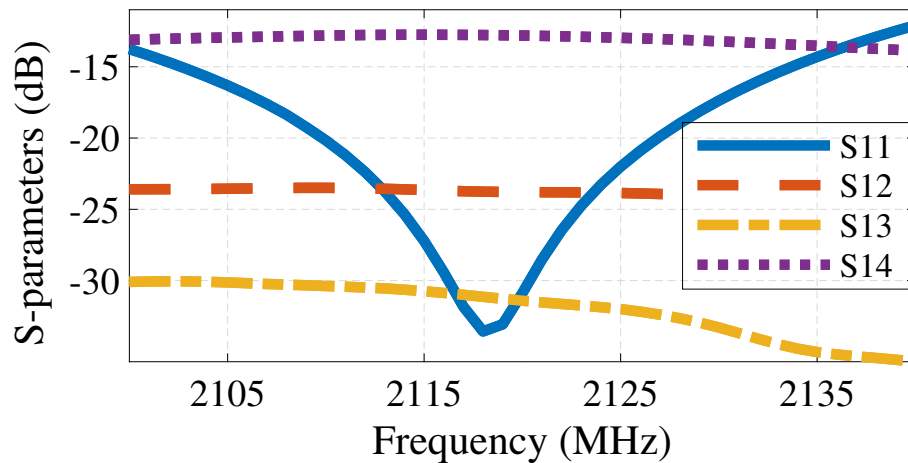


Fig. 5.6 Antenna array measured S-parameters versus frequency for antenna 1. The S-parameters for rest of the array are similar for self reflection (S11), adjacent element reflection (S14), opposite element reflection (S12) and diagonal reflection (S13).

FR4 substrate with dielectric constant $\epsilon_r = 4.4$, thickness of 62 mil and $\tan \delta = 0.02$. The array scattering parameters were measured, where the reference plane was set at the connectors of the array, using a four-port vector network analyzer (VNA). The S-parameter values for one of the antenna elements is depicted in Fig. 5.6. Due to the symmetrical design of the antenna array, and the reciprocity of S-parameters, all antenna elements have similar characteristics. To measure the received signals, a four-channel 16-bit 4 GHz oscilloscope (Rohde&Schwarz RTO2044) was used.

5.2.1 Measurement Setup for Effective Coupling Estimation

A block diagram of the measurement setup for effective coupling estimation is shown in Fig. 5.7. In this experiment TRx is implemented such that ESG and PA represent Tx and the oscilloscope represents the Rx. The Tx and Rx are alternatively connected to the same antenna element, thus emulating the transmit/receive mode in a TDD transceiver. The measured antenna S-parameters were used as a bench mark to evaluate the precision of the estimated couplings. A more precise comparison of the

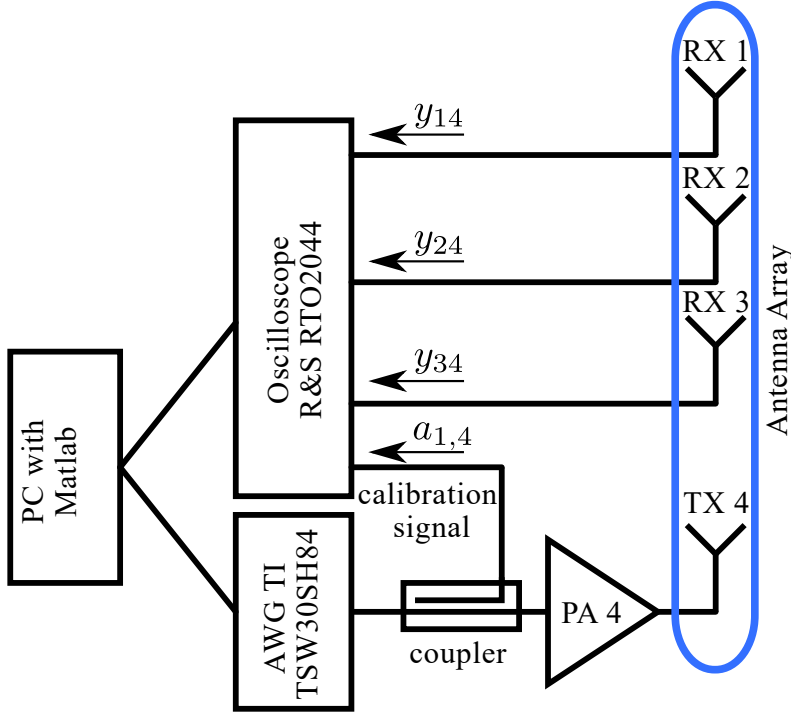


Fig. 5.7 Block diagram of experimental measurement setup for OTA coupling estimation when antenna 4 acts as a common transmitter.

use of S-parameters and estimated couplings is presented via PA model identification and linearization in Section 6.5.1 and Section 6.5.2.

The S-parameter measurements are conducted in a perfectly 50Ω matched setup. Thus, when there is a perfect 50Ω impedance match between the PA and the antenna array, we expect that the estimated effective coupling coefficients match the S-parameter values closely. Any impedance mismatch in a real physical setup results in estimated couplings deviating from S-parameter values.

For the four-element array coupling estimation, four iterations of the experiment are repeated. In each iteration, one of the antenna elements is connected to the signal generator, i.e., in transmission mode, while three other antenna elements were receiving the transmitted signal, i.e., receive mode. The receiver antennas were connected then to the oscilloscope and the received signals were captured simultaneously. Since the generated signal phase can vary each time that the transmission is triggered, a directional coupler was used and the transmitted signal was fed to the coupler input and the coupled path, i.e., the incident signal a_{1j} at

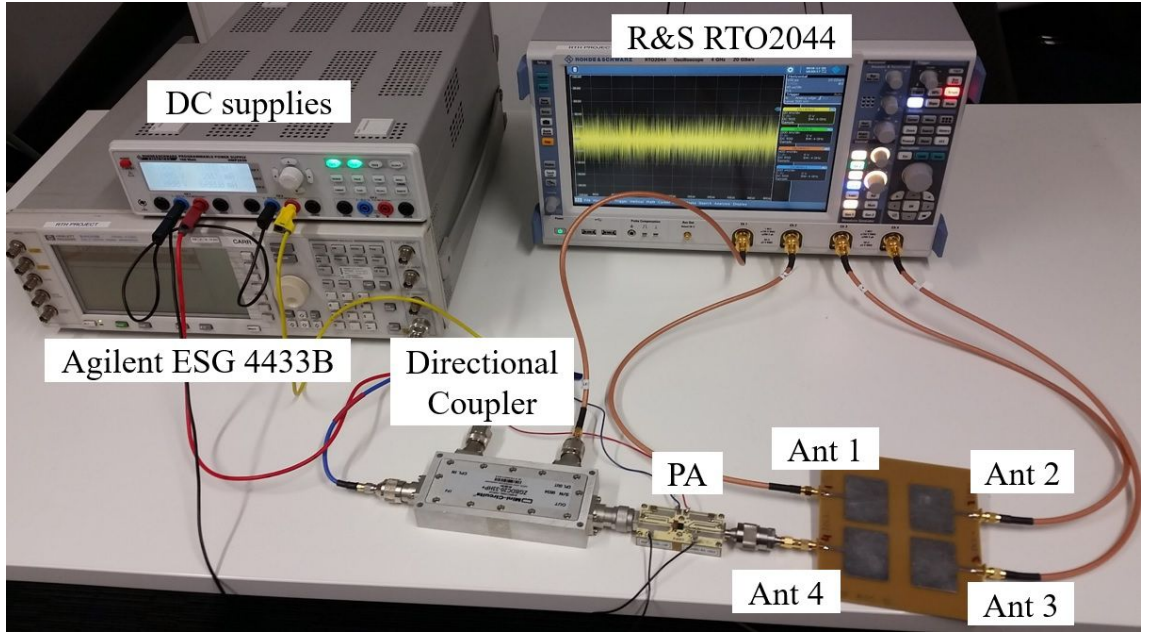


Fig. 5.8 Experimental measurement setup for OTA linearization of the MIMO system.

j th transmitter was measured by the oscilloscope and used as a phase reference between the subsequent measurements. The PA was connected to the reference plane, i.e., the coupler output. The Ψ_{joint} is constructed from the receiver antennas measured signals. The coupled signal a_{1j} is only used in the estimation of λ_{1r} and the evaluation of the reciprocity of the couplings within the array.

Antenna 1 is assigned as the reference antenna in all experiments. To fulfill the requirement for the reference transmitter characteristics to be known, we simply connected the coupler output or the reference plane, directly to the reference antennas and reference couplings are λ_{12} , λ_{13} and λ_{14} .

5.3 Results

In this section, we evaluate the accuracy of coupling estimation for *Single Estimation* and *Joint Estimation*. The results are compared with the measured single frequency S-parameters. Furthermore, the effect of transmitter characteristics on effective coupling estimation is examined by having different transmitter setups.

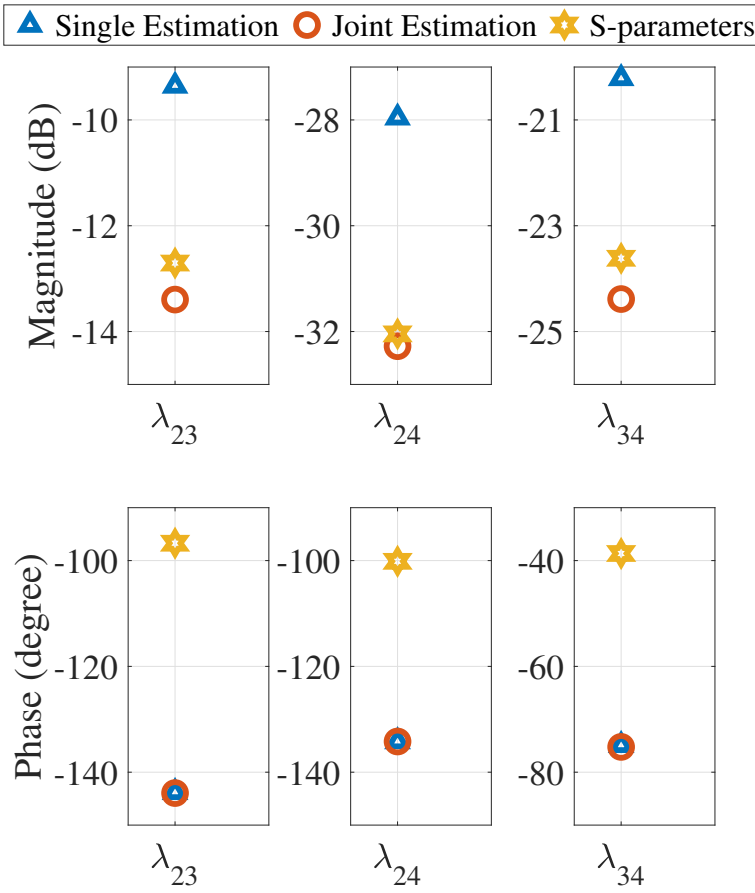


Fig. 5.9 Magnitude (dB) and Phase (degree) of the coupling coefficients corresponding to *Single Estimation*, *Joint Estimation* and S-parameters.

5.3.1 Evaluation of Coupling Estimation

Any impedance mismatch between the PA and antenna as well as the mutual coupling between the antenna elements cause reflection toward the PA output. Such a reflection changes the PA behaviour significantly if the reflected signal power is high [97]. Nevertheless, in experimental setup, the signal level was significantly low to neglect the effect of the reflected signal. To conduct the reference couplings, λ_r , the transmit signal was fed to antenna 1 directly as discussed in Section 5.2.1. To present the results for both *Single Estimation* and the *Joint Estimation* technique, the received signal was captured from all three receiver antennas together with the coupled reference signal.

A comparison of estimated coupling gains and phases are presented in Fig. 5.9 for two estimation techniques, together with the single frequency S-parameters at 2.12 GHz which can be translated to the couplings for a 50Ω match. It can clearly be noticed that the magnitude of the estimated couplings corresponding to *Joint Estimation* performs significantly better than the *Single Estimation*. This can be explained by considering the dense design of the antenna array, where the reference antenna is in close proximity to antenna 2, 3 and 4. Thus, the *Joint Estimation* takes advantage of several reference coupling coefficients. We make a note here that *Joint Estimation* does not simply use an averaging technique for several reference coupling coefficients, but rather all the values of λ_r are involved in the Ψ_{joint} matrix formation. The deviation of magnitude of the jointly estimated couplings from the S-parameter counterparts indicates the impedance mismatch between the PA and antenna. There is a consistent offset in the phase of the estimated coupling coefficients and the measured S-parameters while the phase of the estimated couplings via two different estimation techniques match well. The difference in the phase of the measured S-parameters and those of the estimated couplings are mainly due the different selection of the reference plane of the S-parameters which is at the connectors of the antennas, while the reference plane for couplings estimation is set at the measurement input port of the oscilloscope channels.

In MIMO systems where the transmission and receiver functions are alternated by a switch, the switch response can be modeled together with the transmitter characteristics to preserve the reciprocity of the λ_{ij} .

5.3.2 Impact of Different Transmitter Configurations on Coupling Estimation

The proposed coupling estimation technique eliminates the influence of the characteristics of the transmitters in each path. Three different scenarios were tested to prove the consistency of the estimated coupling, irrespective of the transmitter characteristics. First, each of the transmit antennas were connected directly to the

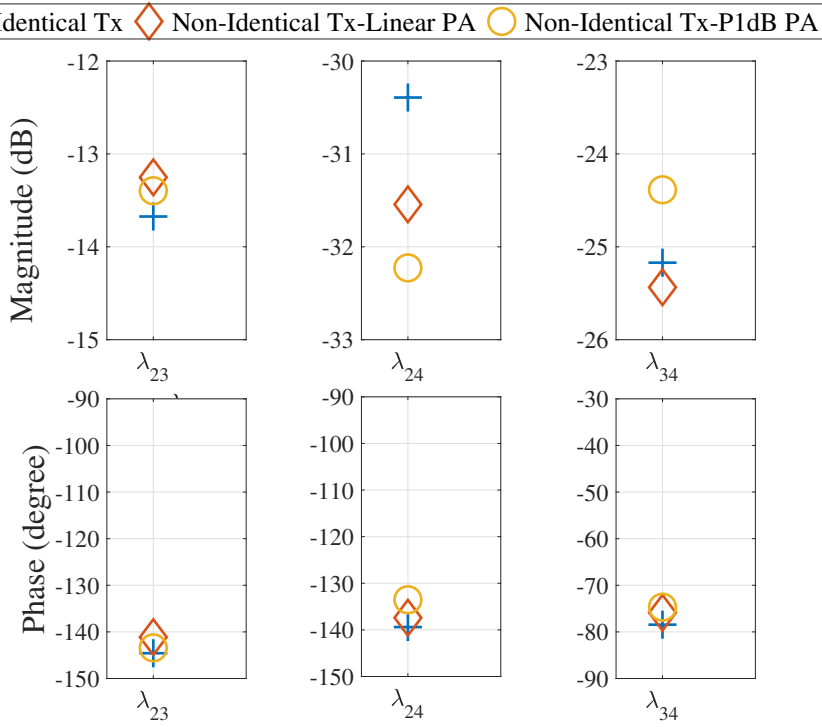


Fig. 5.10 Magnitude (dB) and Phase (degree) of the coupling coefficients corresponding to different transmitter configurations.

direct path of the coupler, hereby referred to as the *Identical Transmitters* case. Second, three class AB PAs (BLP7G22S-10P) were connected to antenna 2, 3 and 4. This is referred to as the *Non-Identical Transmitters* case. To emulate different transmitter characteristics, the PAs were driven with a different back-off level in range 13-15 dB where PA responses are linear. Impedance mismatch between the PA output and antenna and mutual coupling between the antenna elements results in reflections toward the PA output introducing nonlinear distortion that can significantly change the PA behavior [97]. At low power, the effect of the reflected signal is negligible. In the third case, to study the effect of nonlinear distortion and impedance mismatch on the robustness of the coupling estimation, the PAs were driven at the 1-dB compression point (P-1dB).

Estimated coupling gains and phases are presented in Fig. 5.10 for different transmitter configurations which are, *Identical Transmitters*, *Non-Identical Transmitters* with linear PAs, and *Non-Identical Transmitters* with P-1dB PAs.

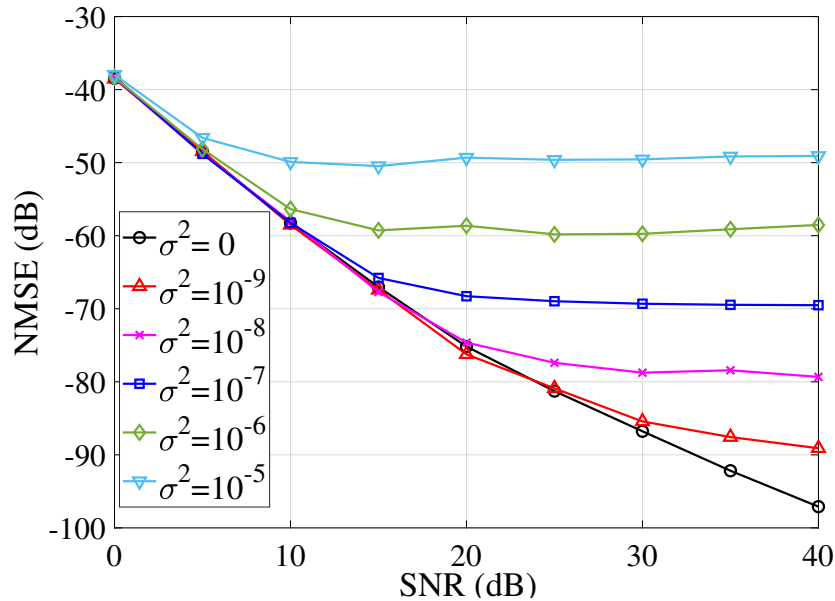


Fig. 5.11 NMSE of estimated couplings vs. SNR for different levels of receiver similarities.

The maximum variation in the magnitude of estimated coupling was obtained for the coupling coefficient related to h_{34} which is 1 dB. The variation of 1 dB in measurement setup is an acceptable margin due to the measurement setup connections have been changed in each measurement iterations to emulate a MIMO TDD system. Thus, the estimated effective couplings for different transmitter types show a good persistence.

5.3.3 Impact of Receiver Characteristic Dissimilarity on Coupling Estimation

For a real physical system, the assumption of perfect similarity in receiver characteristics does not hold. A receiver model was developed to study the effect of dissimilarity in receiver characteristics. In this model, the difference between the receivers is modeled as a stochastic variable and presented as

$$r_i = r(1 + \epsilon_i), \quad i = 1, \dots, K, \quad (5.9)$$

where $\epsilon_i \in \mathcal{CN}(0, \sigma^2)$ is a complex random variable representing the gain deviation relative to the nominal receiver r . The variance of ϵ_i determines the mismatch between the receivers. For $\sigma^2 = 0$ the receivers are identical. Simulation results for different variances of ϵ_i are presented in Fig. 5.11. In this simulation, the S-parameters from the previous experiment were used as the propagation channel. An arbitrary complex constant value was assigned to nominal r . By introducing different variances of ϵ_i distinct gains for r_i were generated. The proposed estimation technique was used to find an estimation of $r_i h_{ij}$. The estimated couplings were compared to the given values of $r_i h_{ij}$ and the normalized mean square error (NMSE) values were calculated.

The NMSE in this figure represents the accuracy in estimation of $r_3 h_{34}$. The error floor is exactly in line with theoretical expectations.

Our assumption for similar receiver characteristics is examined through direct measurement 1 and 2. In these two measurements, the transmitter and receiver antennas were swapped such that their functions were reversed. The couplings $r_i h_{ij}$ and $r_j h_{ji}$ are found, when $f_{t_j}(\mathbf{s}) = \mathbf{s}$, i.e., the *Identical Transmitters* setup. For a known block of transmitted signal \mathbf{s} , an LS approach was used to find the aforementioned couplings. The reciprocity of the propagation channel, i.e., $h_{ij} = h_{ji}$, indicates that any difference between the pairs of $r_i h_{ij}$ and $r_j h_{ji}$ are due to receiver differences.

In these two measurements the j th transmit antenna was connected to the signal generator directly, i.e., $f_j = 1$. A known block of pilot signal was transmitted and received by the i th antennas and λ_{ij} is found by using an LS approach. Then, the transmitter and receiver antennas were swapped such that their functions were reversed, resulting in the calculation of λ_{ji} . Since the propagation channel is reciprocal, i.e., $h_{ij} = h_{ji}$, any difference between λ_{ij} and λ_{ji} indicates the difference between the hardware responses of receivers r_i and r_j . Fig. 5.12 shows the magnitude and the phase of different λ s. *Direct Measurement 1* represent the λ_{23} , λ_{24} and λ_{34} , while *Direct Measurement 2* represent λ values in reverse order, i.e., λ_{32} , λ_{42} and λ_{43} . While there is a perfect match between the phases of λ values in Fig. 5.12, the magnitude

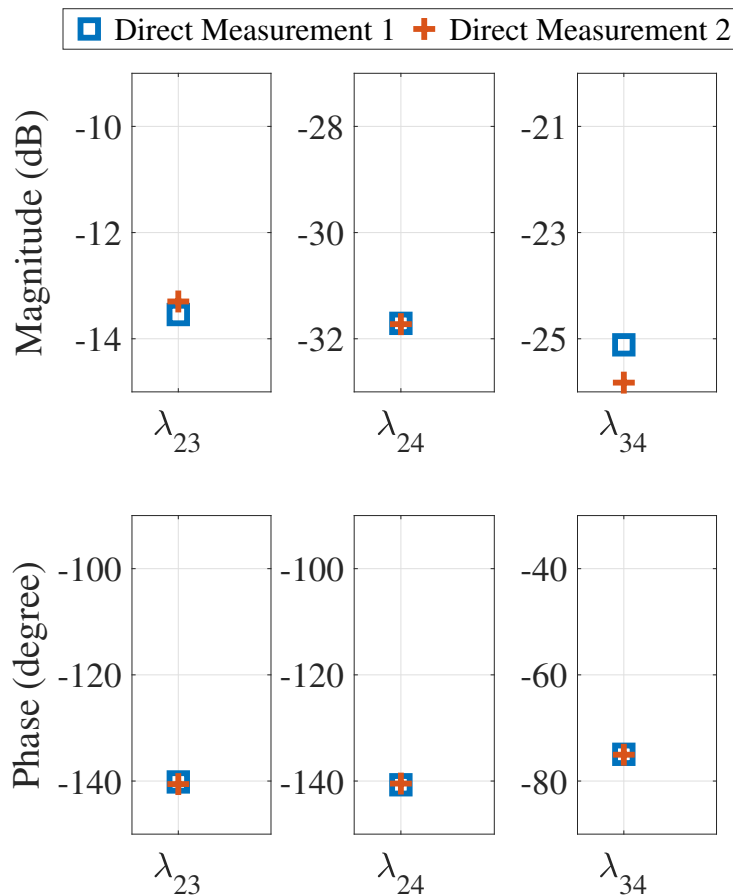


Fig. 5.12 Magnitude (dB) and Phase (degree) of the coupling coefficients to *Direct Measurement 1* and *Direct Measurement 2*.

of λ_{23} and λ_{32} shows a slight difference of 0.2 dB. For λ_{34} and λ_{43} the difference in magnitude is around 0.7 dB. Overall, it should be noted that a variation of less than 1 dB in the measurement setup is an acceptable margin and can be due to the changes in the measurement setup connections and not necessarily an indication of any strong dissimilarity in receiver characteristics.

5.4 Conclusion

A new technique to estimate the intra-array channels in MIMO transceivers has been presented in this chapter. The method relies on a simple sequence of transmitting and receiving of a signal without further calibrations being involved in the procedure. The estimated channels present the behavior of the complete system, i.e., transmitter

Intra Array Coupling Estimation

and receiver are connected to the antenna with impedance mismatches and antenna coupling causing reflections between the array elements and the PA. With the proposed method, as the system end-to-end behavior changes, we can update the channel coefficients. With the aid of the estimated channel coefficients, modeling and linearization of the MIMO arrays may be facilitated using OTA measurements. Such solutions are important considering the current trend towards large-scale MIMO transmitters.

Chapter 6

OTA-based MIMO Transceiver Linearization

The work presented in this chapter relates to the conference proceeding [118].

Recently, over-the-air (OTA) measurements to provide the TOR feedback signal have been proposed for phased arrays as an alternative solution where a limited number of receive antennas capture the transmitted signals[85–87]. Unlike phased arrays, which the linearization can be done for the array response, a fully digital MIMO system requires a DPD per RF PA. This makes OTA-based modeling and linearization of the MIMO system a more complex task, where the channel between the transmitter and receiver antennas must be known. For instance, in [89], Hausmair *et al.* propose to use a few dispersed receiver antennas to collect the combined transmitted signals with OTA measurements. The received signals are used to identify individual PA models, and accordingly, performing the linearization for each PA. Nonetheless, the authors made an assumption that the channels are known.

In this chapter, we propose a DPD technique which utilizes the effective coupling estimation scheme developed in 5. The main idea is to use a few of the embedded receivers of the MIMO TDD transceiver to serve as the OTA-TORs. Recent studies show the benefits of implementing 5G technologies such as Massive MIMO in time-division duplex (TDD) since the pilot overhead is prohibited in frequency-division

duplex (FDD) [76, 119]. In particular, the physical propagation channels for TDD systems are reciprocal since the uplink receiver and downlink transmitter, i.e., the transceivers, are sharing the same antenna by exploiting a switch as depicted in Fig 3.1. In this system, the coupling between the antenna elements enables the intra-array transmission and reception. The approach exploits the preexisting hardware in MIMO TDD system and dispenses the need for TOR per transmitter, therefore reduces the hardware cost and complexity significantly. We develop this DPD technique in three steps: an OTA effective coupling factor estimation scheme that models the propagation channel and receiver gain which is introduced in Chapter 5, a PA model identification for each transmit path, and a nonlinear DPD block in every transmit path. Furthermore, the implementation of TDD transceivers with alternating switches hinder the use of isolators at the antenna since it can block the reception of signal in receive mode. Hence, the excessive nonlinearity and distortion from crosstalk due to antenna coupling and impedance mismatch must be mitigated. Therefore, we adopt the dual-input PA model with linear array model in [97] to compensate for these excessive distortion.

The proposed OTA DPD is evaluated through the measurement of a four-element antenna array. The results are compared to the case when S-parameter measurements replaced the estimated effective coupling within the array, and OTA DPD performs linearization based on the measured S-parameters of the array. In the proposed structure, a combined feedback signal is captured and supplied to the linearization block. Thus, the procedure contains steps similar to the one in [89] and [120]. However, in this work, an iterative approach is adopted to extract the PA models from the combined measured signals. The main reason to perform this iterative model estimation is the presence of crosstalk, which is explained in detail in this section. In this scheme it is assumed that the transmitted signals are not fully correlated.

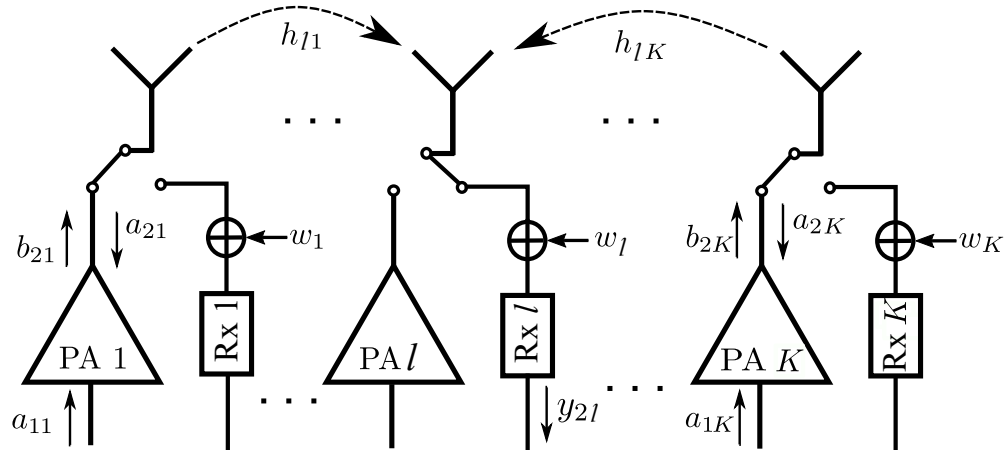


Fig. 6.1 Block diagram of a MIMO system with K transceivers with one transceiver in receive mode while the rest of the array elements are transmitting in presence of crosstalk.

6.1 PA Modeling and Identification for OTA-MIMO Systems

In this section, an expression for a feedback received signal from multi-antenna transmitter is derived assuming that the receiver antenna is placed within the transmitting array as it is depicted in Fig. 6.1. The coupling between the antenna elements of the array enables the OTA-based feedback receiver. The aforementioned coupling not only enables the OTA feedback receiver but it results in excessive nonlinear impairments when presented to the PA outputs. Therefore, the PA models must incorporate the coupling between the transmitting antennas.

To describe the nonlinear input/output relationship of a PA, Volterra series-based approaches have been widely used. Alternatively, the model can represent the discrete-time low-pass equivalent of PA output model, where the baseband input signal is related to the baseband representation of PA output by incorporating only fundamental and odd terms of the respective model. In order to accommodate the linear and nonlinear dynamic effects of PA with fading memory into this model, the excessive terms are introduced. By taking into account the memory effects, the accuracy of the model for wideband signals increases. As a result, a Volterra series based model with memory effects becomes extremely high in order, makes

it infeasible to implement such a model in digital baseband processing. Therefore, depending on the available baseband processing resources, the pruned approaches are adopted to substitute for Volterra series model. Memory polynomial (MP) is a popular reduced form which is exploited frequently as a PA modeling methodology. A dual-input model based on MP approach was presented in Section 3.2.2, when the PA output is a function of incident waves at its in- and outputs, i.e., a_{1j} and a_{2j} . The incident wave a_{2j} is modeled as

$$a_{2j} = \sum_{k=1}^K b_{2k} \lambda_{kj}. \quad (6.1)$$

Accordingly, the baseband description of PA output can be adopted with an equivalent memory polynomial structure. Hence, the PA output at the j th branch can be written as

$$b_{2j}(n) = \sum_{m_1=0}^M \sum_{p=0}^{(P-1)/2} \alpha_{jpm_1} a_{1j}(n - m_1) \quad (6.2a)$$

$$\begin{aligned} & \times |a_{1j}(n - m_1)|^{2p} \\ & + \sum_{m_2=0}^M \beta_{j0m_2} a_{2j}(n - m_2) \\ & + \sum_{m_1=0}^M \sum_{m_2=0}^M \sum_{p=1}^{(P-1)/2} \beta_{jpm_1m_2} \end{aligned} \quad (6.2b)$$

$$\begin{aligned} & a_{2j}(n - m_2) \times |a_{1j}(n - m_1)|^{2p} \\ & + \sum_{m_1=0}^M \sum_{m_2=0}^M \sum_{p=1}^{(P-1)/2} \gamma_{jpm_1m_2} a_{2j}^*(n - m_2) \\ & \times (a_{1j}(n - m_1))^{p+1} (a_{1j}^*(n - m_1))^{p-1}, \end{aligned} \quad (6.2c)$$

where M represents the memory depth and P is the degree of nonlinearity order.

The cross terms in (6.2b) and (6.2c) only contain the linear representation of a_{2j} and a_{2j}^* . This is due to the fact that the incident wave a_{2j} is considered to have lower power [101]. However, for signals with significant power level, higher order of

the a_{2j} must be considered. In matrix form (6.2) can be written as

$$\begin{aligned}\mathbf{b}_{2j} &= \Phi_{t_j}(\mathbf{a}_{1j}, \mathbf{a}_{2j})[\alpha_j^T, \beta_j^T, \gamma_j^T]^T \\ &= \Phi_{t_j}(\mathbf{a}_{1j}, \mathbf{a}_{2j})\theta_j,\end{aligned}\tag{6.3}$$

where matrix Φ_{t_j} represents the basis functions in (6.2a), (6.2b) and (6.2c). The model coefficients to be estimated are α , β and γ .

The combined received signal at the i th receiver from several transmitters for a block of N samples of transmitted signal at i th receiver can be written as follows

$$\begin{aligned}\mathbf{y}_i &= [\lambda_{i1}\Phi_{t_1}(\mathbf{a}_{11}, \mathbf{a}_{21}), \dots, \lambda_{iK}\Phi_{t_K}(\mathbf{a}_{1K}, \mathbf{a}_{2K})]\theta + \mathbf{w}_i \\ &= [\lambda_{i1}\mathbf{b}_{21}, \dots, \lambda_{iK}\mathbf{b}_{2K}]\theta + \mathbf{w}_i,\end{aligned}\tag{6.4}$$

where the vector θ concatenates the coefficients of all PAs where $\theta = [\theta_1^T, \dots, \theta_K^T]^T$. When L receiver antennas are listening, the vector of concatenated received signals is modeled as follows:

$$\mathbf{y} = \begin{bmatrix} \lambda_{t_1 r_1} \Phi_{t_1}(\mathbf{a}_{11}, \mathbf{a}_{21}) & \cdots & \lambda_{t_K r_1} \Phi_{t_K}(\mathbf{a}_{1K}, \mathbf{a}_{2K}) \\ \vdots & \ddots & \vdots \\ \lambda_{t_1 r_L} \Phi_{t_1}(\mathbf{a}_{11}, \mathbf{a}_{21}) & \cdots & \lambda_{t_K r_L} \Phi_{t_K}(\mathbf{a}_{1K}, \mathbf{a}_{2K}) \end{bmatrix} \theta + \mathbf{w},\tag{6.5}$$

where $\mathbf{y} = [\mathbf{y}_1^T \dots \mathbf{y}_L^T]^T$ and $\mathbf{w} = [\mathbf{w}_1^T, \dots, \mathbf{w}_L^T]^T$. For PA model coefficient identification, the estimated effective coupling values substitute the λ_{ij} in (6.5). A set of received signals \mathbf{y} from L receivers are measured and the transmitted signals \mathbf{a}_{1k} are known. The PA coefficients are to be estimated for transmission path 1 to K . The main difference in coefficients identification in (6.4) and those proposed by [89] and [120] is the presence of the reflection signal \mathbf{a}_{2j} , which initially is not known. Unlike the previous studies, a linear LS approach cannot be used directly to estimate θ . Instead, our approach to estimate the PA coefficients is to iteratively update several parameters in Algorithm 1 until a satisfactory result is achieved. Algorithm 1 is based on an estimation of received signal, $\hat{\mathbf{y}}_i$. The known parameters are the incident signals at the PA inputs $\mathbf{a}_1 = [\mathbf{a}_{11}, \dots, \mathbf{a}_{1K}]$, and the measured received signal, \mathbf{y}_i

at the i th receiver. The procedure starts with initialization of $\hat{\mathbf{b}}_{2j}^{(i)}$ at time instance $n = 0$ and iteration $i = 0$. At this moment the input to the PA has not affected its output. Thus, at the start of the procedure there is no signal available at the PA outputs. Subsequently, the $\hat{\mathbf{a}}_{2j}^{(i)}$ can be updated from (6.1), where the values of λ_{kj} can be replaced by their counterparts from the proposed effective coupling estimation. At this point both input signals of \mathbf{a}_{1j} and \mathbf{a}_{2j} to dual-input model in (6.4) are known. This procedure is repeated for transmit paths 1 to K . Therefore, the PA coefficients can be extracted following a LS approach in (6.5) as follows

Algorithm 2 PA model identification

Require: input signals $\mathbf{a}_{11}, \dots, \mathbf{a}_{1K}$, measured received signals \mathbf{y}_i from two or more receivers,

estimated couplings λ

Initialization: set $i = 0$, $\hat{\mathbf{b}}_{2j}^{(0)} = 0$, $\text{NMSE} = \infty$,

define the desired accuracy level by NMSE_{des}

while $\text{NMSE} \geq \text{NMSE}_{des}$ **do**

$k = k + 1$

use $\hat{\mathbf{b}}_{2j}^{(k-1)}$ in (6.1) to compute $\hat{\mathbf{a}}_{2j}^{(k)}$

use \mathbf{a}_{1j} and $\hat{\mathbf{a}}_{2j}^{(k)}$ in (6.6) to find $\hat{\theta}$ by LS

use \mathbf{a}_{1j} , $\hat{\mathbf{a}}_{2j}^{(k)}$ and $\hat{\theta}$ in (6.3) to find $\hat{\mathbf{b}}_{2j}^{(k)}$

use $\hat{\mathbf{b}}_{2j}^{(k)}$ in (6.4) to compute $\hat{\mathbf{y}}_i^k$

calculate $\text{NMSE} = \max_i \{\text{NMSE}(\mathbf{y}_i, \hat{\mathbf{y}}_i^k)\}$ from (6.7)

end while

Output: PA model coefficients

$$\hat{\theta} = \left[\begin{array}{ccc} \lambda_{t_1 r_1} \Phi_{t_1}(\mathbf{a}_{11}, \mathbf{a}_{21}) & \cdots & \lambda_{t_K r_1} \Phi_{t_K}(\mathbf{a}_{1K}, \mathbf{a}_{2K}) \\ \vdots & \ddots & \vdots \\ \lambda_{t_1 r_L} \Phi_{t_1}(\mathbf{a}_{11}, \mathbf{a}_{21}) & \cdots & \lambda_{t_K r_L} \Phi_{t_K}(\mathbf{a}_{1K}, \mathbf{a}_{2K}) \end{array} \right]^+ \mathbf{y}, \quad (6.6)$$

where the pseudoinverse $\mathbf{X}^+ = (\mathbf{X}^H \mathbf{X})^{-1} \mathbf{X}^H$ is used. Next, the estimated PA coefficients $\hat{\theta}$ are used to update the estimated PA outputs \mathbf{b}_{2j} . These estimated PA outputs are used in next iteration to update $\hat{\mathbf{a}}_{2j}$ values. The $\hat{\mathbf{b}}_{2j}$ signals are initially set to zero.

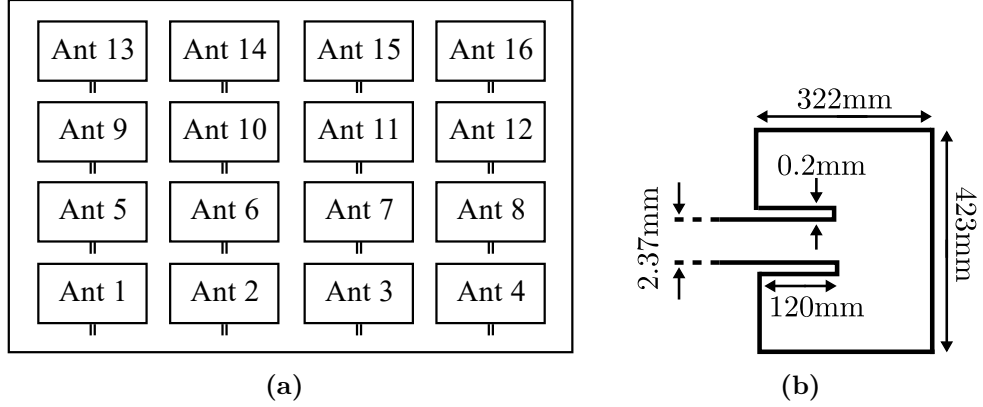


Fig. 6.2 The layout of the 4×4 array is given in (a), the dimensions of a single patch antenna are given in (b).

The iterations are repeated until the algorithm converges and a satisfactory accuracy in the results are achieved. To evaluate the accuracy of the estimated PA parameters, the estimation of $\hat{\mathbf{b}}_{2j}$ are used in (6.5), to find an estimate of all received signals $\hat{\mathbf{y}}_i$. We use normalized mean square error (NMSE) as an index to evaluate the precision of our estimations of $\hat{\mathbf{y}}_i$ signals as

$$\text{NMSE}(\mathbf{y}_i, \hat{\mathbf{y}}_i) = \frac{(\mathbf{y}_i - \hat{\mathbf{y}}_i)^H (\mathbf{y}_i - \hat{\mathbf{y}}_i)}{\mathbf{y}_i^H \hat{\mathbf{y}}_i}. \quad (6.7)$$

In simulations, we noticed a bias in the estimated parameters of β and γ , when only one receiver is used. The reason for this bias is that the basis functions in (6.2b) and (6.2c) comprise the incident wave \mathbf{a}_{1j} and \mathbf{a}_{2j} . Each signal \mathbf{a}_{2j} is composed of PA output signals \mathbf{b}_{2j} . Thus, the LS approach results in PA model coefficients β and γ being optimized to fit the basis functions formed by the \mathbf{a}_{2j} signals. This results in the estimation of PA model coefficients with good accuracy in terms of estimated received signals, while the PA model coefficients are not accurately estimated. However, by using two or more receiver antennas, we can avoid this ambiguity in estimated model coefficients. We remark that when the received signals are strong, only two receiver antennas are sufficient to resolve this uncertainty.

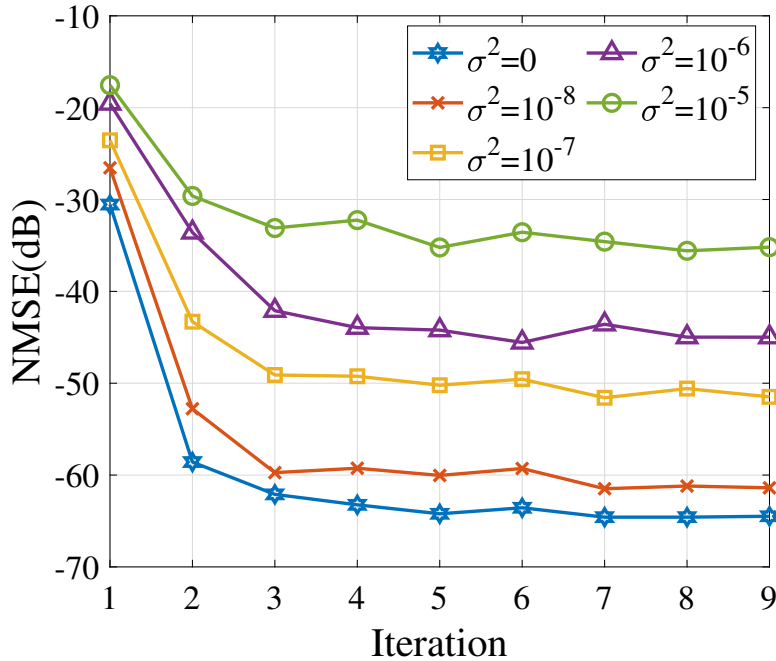


Fig. 6.3 NMSE of estimated PA models per iteration of Algorithm 1

6.2 Performance Assessment

The simulations are performed for a 4×4 rectangular array with patch antennas as in Fig. 6.2 at center frequency of 2.12 GHz. The characteristics of the PAs connected to each antenna element are conducted from measurements of a class AB PA (BLP7G22S-10P) based on the complex polynomial model of order $P = 5$ and $M_1 = M_2 = 2$. The PA models in adjacent transmitters are obtained by adding several perturbations to the measured PA coefficients. Therefore, different PA behaviors are achieved, where the nonlinearity characteristics and linear gains of all PAs are in the same order.

The array characteristics are simulated with Keysight Advanced Design System Momentum and S-parameters are obtained. We select FR4 substrate with dielectric constant $\epsilon_r = 4.4$, thickness of 62 mil and $\tan \delta = 0.02$ and element spacing of 0.35 wavelength.

6.2.1 Simulation Setup for PA Modeling

Algorithm 2 is validated by performing the PA model identification when all the antenna elements are transmitting. The accuracy of the estimated PA model is notable from two perspectives: *i*) the accuracy of estimated effective coupling in the previous step, and *ii*) the convergence of the Algorithm 2 which can be analyzed by standard methods such as the distance between consecutive NMSE of estimated received signals. To emulate the eventual mismatches in the estimation of λ_{ij} , we add a stochastic variable to the effective couplings estimated such that

$$\tilde{\lambda}_{ij} = \lambda_{ij}(1 + \epsilon), \quad (6.8)$$

where $\epsilon \in \mathcal{CN}(0, \sigma^2)$ is a complex random variable representing the coupling estimation error. The accuracy of the estimated PA models is studied for different variances of ϵ . The convergence and accuracy of the PA model estimation are analyzed for ideal SNR of the received signal. In Fig. 6.3, the NMSE of the estimated PA models are presented versus the number of iterations in Algorithm 2. Fig. 6.3 illustrates the role played by the coupling estimation error in terms of PA model accuracy and convergence. Evidently, the bigger the variance of ϵ , the worse the NMSE of PA models. The number of iterations until convergence is seen to be independent of the σ^2 . If the initial guess of $\hat{\mathbf{b}}_{2j}^{(0)}$ is chosen via preexistence measurement, e.g., calibration phase, our simulation indicates convergence in two iterations with $\sigma^2 = 10^{-8}$.

6.3 Predistortion

Following the model-based technique in [121], i.e., MILA, the PA model extracted in the previous section is used to perform linearization on individual transmit paths. The identified PA model coefficients can be used together with λ values to estimate the PA outputs in a MIMO transmitter [95, 97]. For the array systems, the MILA approach provides a feedback signal based on the identified PA model. As for the digital predistorter, we adopt the technique proposed by [99]. In this technique, a

dual-input DPD is implemented in each transmit path. For the sake of clarity we summarized the dual-input DPD steps and we refer the interested readers to [99] for more details. The dual-input DPD is a function of estimated $\hat{\mathbf{a}}_{2j}$ from (6.1) and the known desired output signal $\mathbf{b}_{(des)j}$ from the j th PA. Therefore, in a perfectly linearized transmitter, $\mathbf{b}_{2j} = \mathbf{b}_{(des)j}$. The linearization iteration starts with the initial value of $\hat{\mathbf{a}}_{2j}^{(0)}$ calculated from (6.1) when $\mathbf{b}_{2j} = \mathbf{b}_{(des)j}$ and the estimate of PA output signal $\hat{\mathbf{b}}_{2j}^{(0)}$. Thus, for each iteration, the DPD coefficients in j th transmit path are obtained by utilizing LS approach as follows

$$\varphi_j^{(i+1)} = \mathbf{G}_{t_j}(\hat{\mathbf{b}}_{2j}^{(i)}, \hat{\mathbf{a}}_{2j}^{(i)}) + \hat{\mathbf{a}}_{1j}^{(i)}, \quad (6.9)$$

where $\varphi_j^{(i+1)}$ represent a vector of DPD coefficients and matrix \mathbf{G}_{t_j} contains the blocks of basis waveforms. Respectively, the input signal to the j th PA is calculated by

$$\hat{\mathbf{a}}_{1,j}^{(i+1)} = \mathbf{G}(\mathbf{b}_{(des)j}, \hat{\mathbf{a}}_{2j}^{(i)}). \quad (6.10)$$

The PA output is updated as $\hat{\mathbf{b}}_{2j}^{(i+1)}$. The procedure is repeated until a satisfactory linearization is achieved.

6.4 Experimental Validation

In this section, the measurement setup for a four-element antenna array MIMO system is presented to validate the proposed PA model identification utilizing OTA measurements. Then, the results and comparisons are presented in Section 6.5.

The experimental task is carried out to perform the linearization technique utilizing OTA measurements, using the estimated effective couplings in Section 5.3.1 and the measured S-parameters.

For the experimental validation, OFDM test signals with 5 MHz bandwidth were generated in MATLAB. The signals have a peak-to-average power ratio (PAPR) of

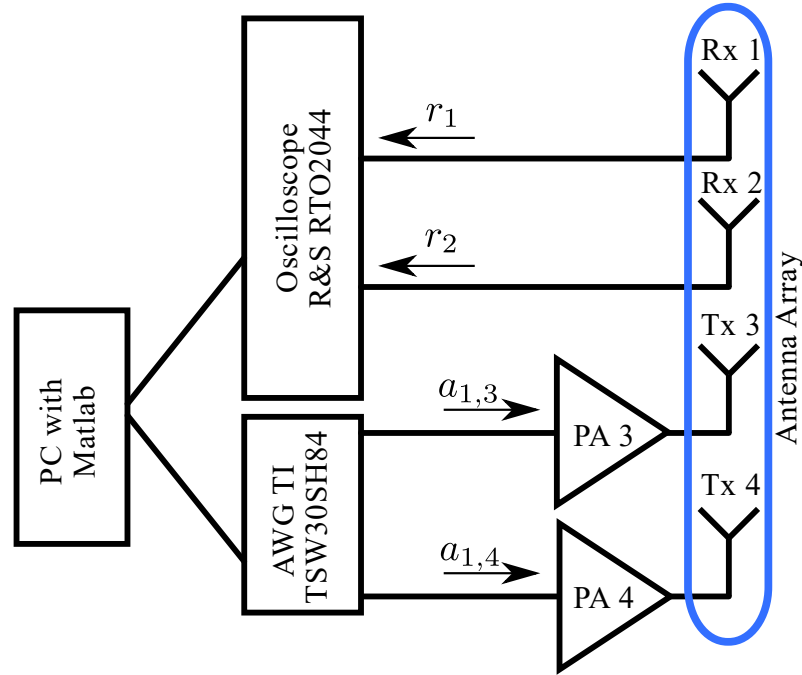


Fig. 6.4 Block diagram of experimental measurement setup for DPD implementation with OTA measurements. Antenna 1 and 2 are in receive mode and antenna 3 and 4 are in transmit mode.

8.5 dB. This bandwidth is wide enough to capture the dynamic effects of the PAs. A dual-channel vector modulator evaluation board (Texas Instrument, TSW30SH84) was used to synthesize the driving signals. The four-element rectangular patch antenna array was used with characteristics of resonant frequency of 2.12 GHz and manufactured with FR4 substrate with dielectric constant $\epsilon_r = 4.4$, thickness of 62 mil and $\tan \delta = 0.02$. The array scattering parameters were measured, where the reference plane was set at the connectors of the array, using a four-port vector network analyser (VNA). To measure the received signals, a four-channel 16-bit 4 GHz oscilloscope (Rohde&Schwarz RTO2044) was used.

6.4.1 Measurement Setup for PA modeling and DPD technique using OTA Measurements

As it was stated earlier, for PA model identification with OTA measurements, two or more receiver antennas are needed. Thus, for the four-element array, two antennas are

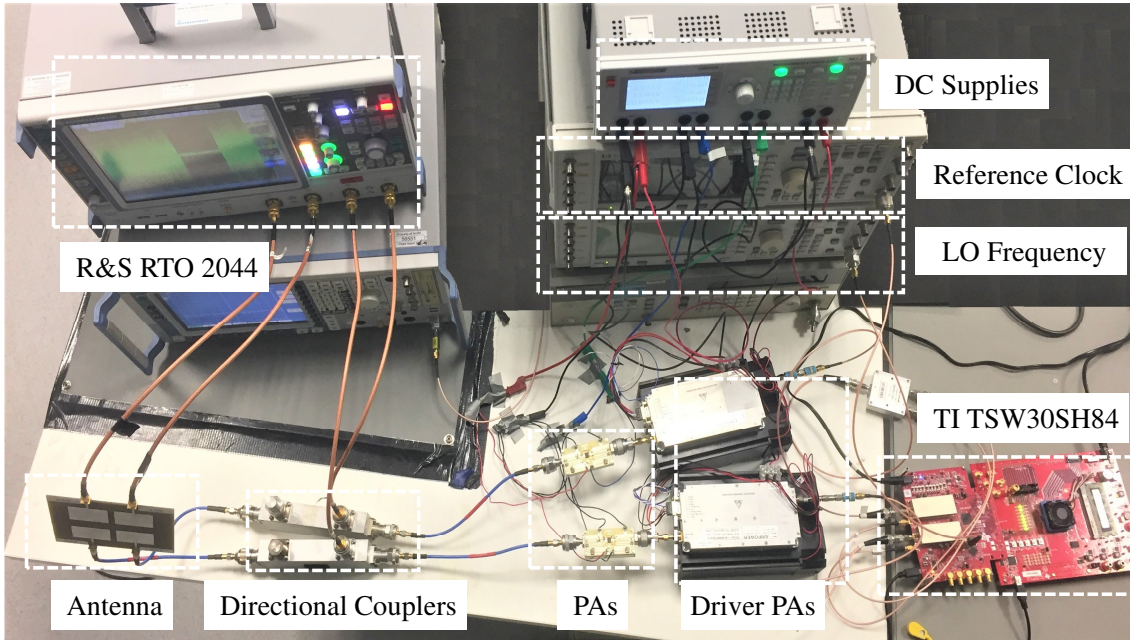


Fig. 6.5 Experimental measurement setup for OTA linearization of the MIMO system.

in receive mode (Rx1 and Rx2), while two antennas are transmitting simultaneously (Tx3 and Tx4). The block diagram of the setup is depicted in Fig. 6.4. Since the coupling between each pair of antennas is identified in the previous step, the transmitter and receiver antennas order is chosen arbitrarily. For any extended arrays, there is no need to increase the number of receiver antennas as long as there is a sufficiently high level of coupling between the transmitter antennas and the receivers. The linearized results are presented when estimated couplings are used to determine the signal $\mathbf{a}_{2,j}$ and the received signal \mathbf{y}_i . Subsequently, the same procedure is followed by replacing the estimated coupling values by their counterpart S-parameters and the results are compared.

The antennas are wideband in relation to the transmit signal bandwidth. As depicted in Fig. 5.6, the array shows almost flat characteristics within the 5 MHz of transmitted signal bandwidth for S12, S13 and S14. However, the self reflection parameter S11, shows strong frequency dependent behavior, while it presents low

power level in comparison to the opposite element reflection (S12) and adjacent element reflection (S14). Therefore, we limit our experiment to the single frequency representation of the S-parameters at the center frequency $f_c = 2.12$ GHz which allows a scalar representation of the coupling as in (6.1).

The in-band performance of DPD is evaluated by NMSE and, to evaluate the out-of-band radiation of the distortion in the adjacent channels, the adjacent channel leakage ratio (ACLR) is used. The NMSE is formulated as [122]

$$\text{NMSE} = \frac{\sum_{n=0}^{N-1} |x(n) - \hat{x}(n)|^2}{\sum_{n=0}^{N-1} |x(n)|^2}, \quad (6.11)$$

where $x(n)$ is the desired PA output and $\hat{x}(n)$ is the measured PA output signal for N samples. The ACLR can be defined as

$$\text{ACLR} = \max_{m=L,U} \left\{ \frac{\sum_{f(adj)_m} |X(f)|^2}{\sum_{fch.} |X(f)|^2} \right\}, \quad (6.12)$$

where $X(f)$ denotes the power spectrum of $x(n)$ for inband frequencies, i.e., fch and the frequencies in lower (L) and upper (U) adjacent channels $f(adj)_m$.

6.5 Results

In this section, we first evaluate the coupling estimation, since its precision is indispensable for the dual-input DPD technique. Then, the results for the PA model identification and DPD performance are presented, and compared to the case where the single frequency S-parameters are used.

6.5.1 Evaluation of PA model identification with OTA measurements

The PA model identification reliability is integral for the proposed dual-input DPD with OTA measurements (OTA DPD).

A photograph of the measurement setup based on the block diagram of Fig. 6.4 is presented in Fig. 6.5. The two uncorrelated and independent driving signals for the PAs were created in MATLAB. The signals used for these experimental validations were OFDM signals and similar to the previous experiment, the signals have 5 MHz of bandwidth and PAPR of around 8.5 dB. The signals were fed to the driver PAs which followed by the main PAs and connected to the transmit antennas. The individual receiver antennas were connected to the oscilloscope channels. The two received signals were captured simultaneously, each with an individual receiver. The main PAs were two class AB PAs (BLP7G22S-10P). The TSW board and oscilloscope were connected to the 10MHz reference clock to synchronize the transmitters and the receivers.

Each PA output was connected to a directional coupler where the coupled path was measured with the oscilloscope and represented to evaluate the performance of the PA identification and OTA DPD for individual PAs, and was not involved in the PA modeling and linearization procedure. The direct path of the couplers was fed to two of the antenna elements, representing the signals from Tx3 and Tx4. The two other antenna elements were then measured with the oscilloscope and represented the received signals from Rx1 and Rx2. The captured signals from Rx1 and Rx2 were processed in MATLAB at a baseband sampling frequency of 25 MHz.

The proposed PA model identification technique was tested when the estimated couplings and the S-parameters were used to replace the couplings. A disadvantage of using S-parameters is that a separate and calibrated measurement setup is needed to measure the antennas S-parameters and the antenna array must be disassembled from the PAs. In addition, the calibration for the S-parameter measurement setup does not necessarily match the calibration in the intended transmission setup.

In this MIMO system, each received signal is a linear combination of the two transmitted signals experiencing the channel between the transmitter and receiver antennas as well as the receiver chain.

It is clear that the S-parameters represent the coupling between the antenna elements, while the receiver characteristics are not included in S-parameters. In

contrast, the proposed coupling estimation technique not only estimates the coupling, but it presents the effect of the receiver chain, resulting in a more accurate estimation of the received signal.

One particular aspect of precise model identification is the necessity of time and phase alignment of the PA input signal with received signal. Since in this MIMO setup, each received signal associates with two input signals, the received signals cannot be correctly time-aligned and phased-aligned with respect to both input signals. Instead, we time aligned the input signals with respect to the received signal at Rx1 and generated two reference signals $\mathbf{a}_{1,1}^{\text{ref}(1)}$ and $\mathbf{a}_{1,2}^{\text{ref}(1)}$. The reference signals with respect to the received signal at Rx2 were $\mathbf{a}_{1,1}^{\text{ref}(2)}$ and $\mathbf{a}_{1,2}^{\text{ref}(2)}$ respectively. Thus, each basis function $\Phi_{t_j}(\cdot)$ was calculated two times in (6.4): once with input signal $\mathbf{a}_{1,j}^{\text{ref}(1)}$ in relation to \mathbf{y}_1 , and then with input signal $\mathbf{a}_{1,j}^{\text{ref}(2)}$ in relation to \mathbf{y}_2 .

The spectrum of the received signal via simulation was obtained by linear combination of the modeled PA outputs multiplied by the respective couplings. A comparison of the spectrum of individual received signal to the spectrum of the respective measured received signal is shown in Fig. 6.6 and Fig. 6.7. More specifically, Fig. 6.6 shows the simulation results when the S-parameters are representing the couplings and in Fig. 6.7 when estimated couplings were used. The error spectra of the models are also shown. As it can be seen in Fig. 6.6 and Fig. 6.7, the simulated spectra of the received signal match well with the measured spectra for Rx1 and Rx2 in both cases. However, when the estimated couplings were used, the error spectra show slightly better results. For a more precise evaluation of the PA model identification, the coupled output of the PAs were measured and compared with the modeled PA outputs.

A comparison of the spectrum of each individual simulated PA output to the spectrum of the respective measured PA output is shown in Fig. Fig. 6.8 and Fig. 6.9. The result in Fig. 6.8 shows the simulation results when the S-parameters represent the couplings and Fig. 6.9 shows the simulation results when the estimated couplings represent the couplings. The spectra of the error are shown to give a better

Table 6.1 ACLR and NMSE for Different Coupling Coefficients for OTA DPD Technique

DPD technique	ACLR (dB)				NMSE (dB)	
	PA1	PA2	Rx1	Rx2	PA1	PA2
no DPD	-39.5	-34.8	-40.0	-36.4	-23.8	-20.1
SP DPD	-47.9	-45.2	-47.0	-45.9	-33.2	-26.3
EC DPD	-49.1	-49.7	-49.3	-48.9	-39.3	-38.0

understanding of the PA modeling performance. It is clear that, for the case with the S-parameters, the PA model does not perform as well as the proposed technique.

Analysis of the presented results, two patterns can be noted. First, the error spectra of the PA models are worse than the error spectra of the received signals. This effect can be explained by the fact that in PA model identification technique, when we use S-parameters, any impedance mismatch in the experimental setup results in a deviation from the S-parameters values. Thus, the PA modeling using the S-parameters shows a significant error in the spectra. For the other case, we used the estimated couplings, which are the combination of the coupling and the receiver characteristics. However, the coupling represented between two transmit branches does not include any receiver characteristics. Thus, the lower error spectra for received signals compared to the error spectra of PA outputs indicates a small bias in PA model identification. Nonetheless, the modeling technique, when the estimated couplings were used, results in a significantly low error spectra compared to the case when S-parameters are used. Second, we notice that although the estimated PA models for PA1 and PA2 show relatively similar patterns when S-parameters are used, the overall estimated receiver model for Rx2 is worse than Rx1 with S-parameters (See Fig. 6.6 and Fig. 6.7). The fact that PA2 is in closer proximity to Rx2, indicates a higher error in model identification of PA2 with S-parameters.

Overall, it must be noticed that several factors limit the PA model evaluation using OTA measurements, as well as the proposed coupling estimation. The coupling estimation procedure was carried out in a different measurement setup, where the connections to the antenna were changed to imitate a MIMO setup. Ideally,

the proposed estimation technique is performed in a full MIMO setup where the impedance mismatch effects remain constant, owing to the connections being unchanged. However, with a full MIMO system, the proposed technique is superior to the conventional setups where the output of each PA must be measured separately, to perform the PA modeling and linearization. The S-parameters measurements also cannot fully represent the couplings in the setup, where every difference in the impedance matching can cause small uncertainties that can add up and influence the outcome of the results.

6.5.2 Evaluation of Dual-Input DPD with OTA measurements

Results of the proposed OTA DPD technique, where the coupling and the channel between the antennas were replaced by the estimated coupling are indicated with DPD with estimated coupling (EC DPD) and the results using the single frequency S-parameters are indicated with DPD with S-parameters (SP DPD). The level of linearization was limited to the noise floor of the oscilloscope.

The ACLRs for each of the received signals at Rx1 and Rx2, and each of the output signals from PA1 and PA2 are given in Table 6.1. When no DPD is implemented, the ACLR values are -39.5 dB and -34.8 dB for PA1 and PA2 respectively. Implementing the SP DPD improves the ACLR to -47.9 for PA1 and -45.2 dB for PA2. By using the proposed EC DPD, the ACLR improves to around -49.5 dB for both PAs. The ACLR results of Rx1 and Rx2 indicate the improvement in the linearization of the received signals to a similar level as the individual PA outputs.

The NMSEs for PA1 and PA2 output signals are given in Table 6.1. In order to present the NMSE values for the received signals, the channels between the antenna elements must be replaced by the estimated coupling coefficients. This can cause uncertainties in the NMSE results of the received signals. Thus, we limit the presented NMSE results only to the PA output signals. Compared to the case without DPD, SP DPD achieves an improvement of 12 dB for PA1. However, for

PA2 the performance of SP DPD was only 6 dB of improvement. In comparison, the proposed EC DPD shows an improvement of 18 dB for PA2 and 15.5 dB for PA1. To this end, EC DPD shows better linearization performance. The results show an agreement with the case when the S-parameters are used to estimate the PA models which results in worse performance.

In Fig. 6.10, the spectrum of the signal at PA outputs are plotted when no DPD is implemented. Then, the PA outputs are plotted when the EC DPD and SP DPD are implemented. The plots are clearly inline with the results presented in Table 6.1. In Fig. 6.11, the spectrum of the received signals, RX1 and RX2 are plotted when no DPD is implemented. Then, the spectrum are plotted when the EC DPD and SP DPD are implemented. The results indicates the level of distortion in combined received signals. The spectrum in the Fig. 6.10, and Fig. 6.11 indicate that the linearization performed in the proposed technique is independent of the OTA receiver position.

6.6 Conclusion

In this chapter, the estimated coupling technique presented in Chapter5 is used in combination with PA modeling for identification and linearization. The proposed techniques allow for linearization of an arbitrary size MIMO system that suffers from cross-talk and impedance mismatch without a need for separate observation receiver per transmitter branch. The effectiveness of the proposed techniques are validated in a measurement setup with a four-element antenna array, representing a MIMO system. S-parameter measurements require disassembly of PAs from the antennas. Particularly, at mm-wave, the disassembly of antenna from the PAs is not possible, and OTA measurements to identify the coupling coefficients is the only way forward. Therefore, the hardware complexity of the proposed technique remains low as the size of the array increases. Considering the high demand for large-scale MIMO systems, our technique has a considerable benefit in reducing the cost and complexity of array linearization. As we have shown, no prior knowledge of transmitter and receiver

hardware responses is required to identify the coupling between the antennas as well as the PA modeling and linearization.

Results are shown for coupling estimation with their S-parameters counterparts. It can be seen that the existing impedance mismatch in the setup causes a deviation between the estimated couplings and the S-parameters. To validate the accuracy of the estimated couplings, a PA modeling technique together with a dual-input DPD were implemented. The estimated couplings and the S-parameters were used to imitate the channel between the antenna elements while the PA modeling and the linearization were performed. It can be seen that our proposed technique yields an improved performance without any need for a separate calibrated setup similar to those used for S-parameters measurements. We make it clear that at least two receiver antennas are required for PA model identification technique with OTA measurements. As the size of the array increases, no more receiver antennas are needed, as long as all transmitted signals are coupled into the receiver antennas.

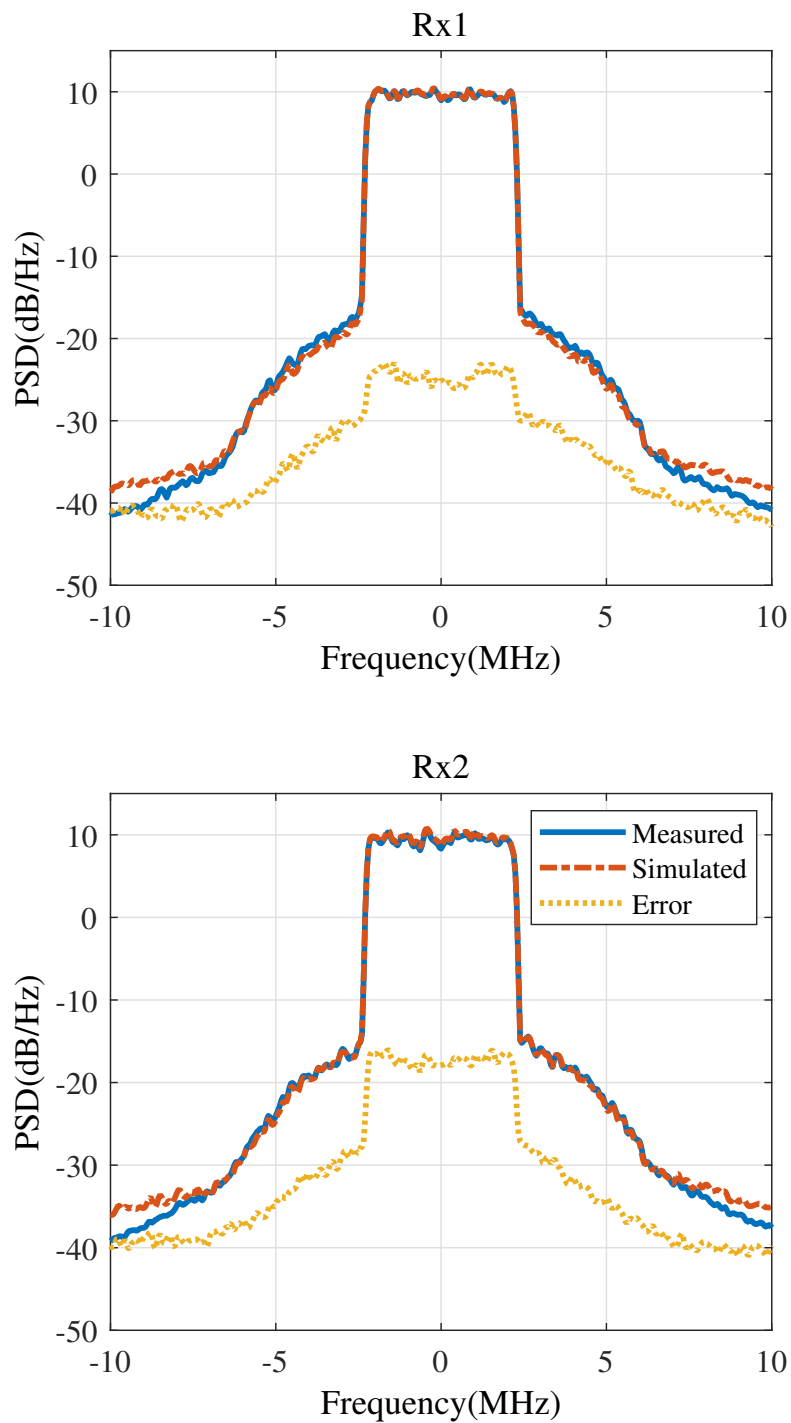


Fig. 6.6 Spectra of received signals at Rx1 and Rx2 from measurement (Meas), simulation (Sim), and the spectra of error (Err) in simulation, when the couplings between the antenna elements are replaced by single frequency S-parameters.

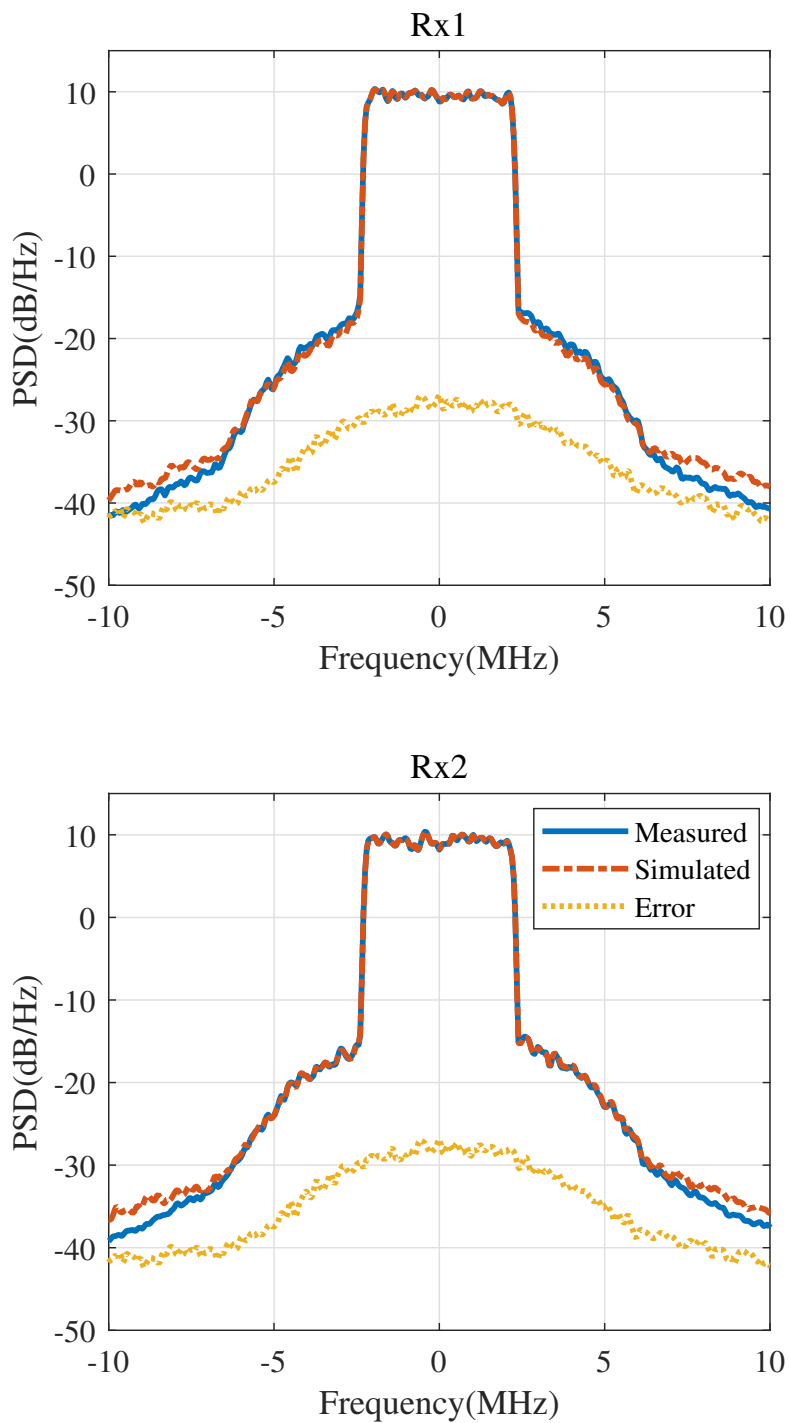


Fig. 6.7 Spectra of received signals at Rx1 and Rx2 from measurement (Meas), simulation (Sim), and the spectra of error (Err) in simulation, when the couplings between the antenna elements are replaced by estimated couplings.

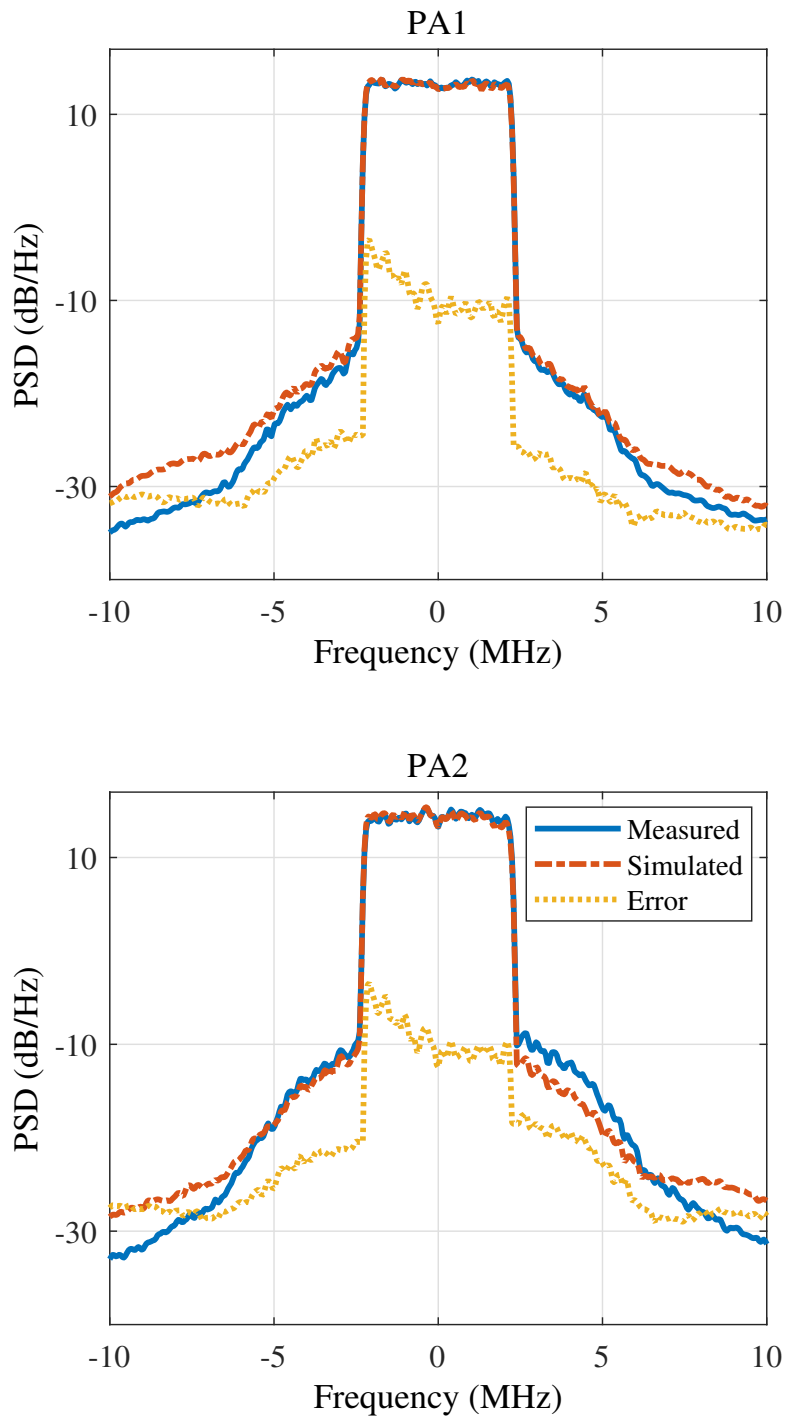


Fig. 6.8 Spectra of measured PA outputs (Meas) from couplers coupled line, and the simulated PA outputs (Sim). The error spectra (Err) shows the error in simulation when the couplings between the antenna elements are replaced by single frequency S-parameters.

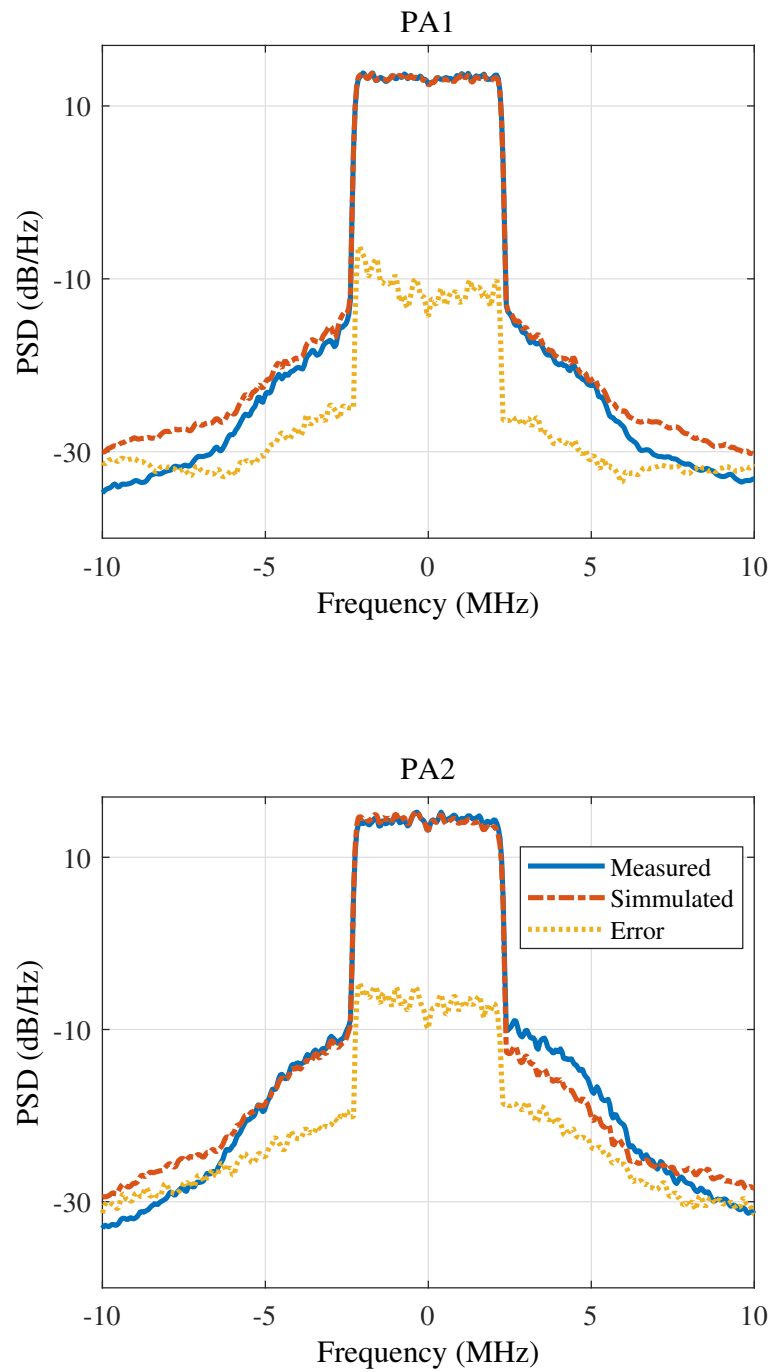


Fig. 6.9 Spectra of measured PA outputs (Meas) from couplers coupled line, and the simulated PA outputs (Sim). The error spectra (Err) shows the error in simulation when the couplings between the antenna elements are replaced by estimated couplings.

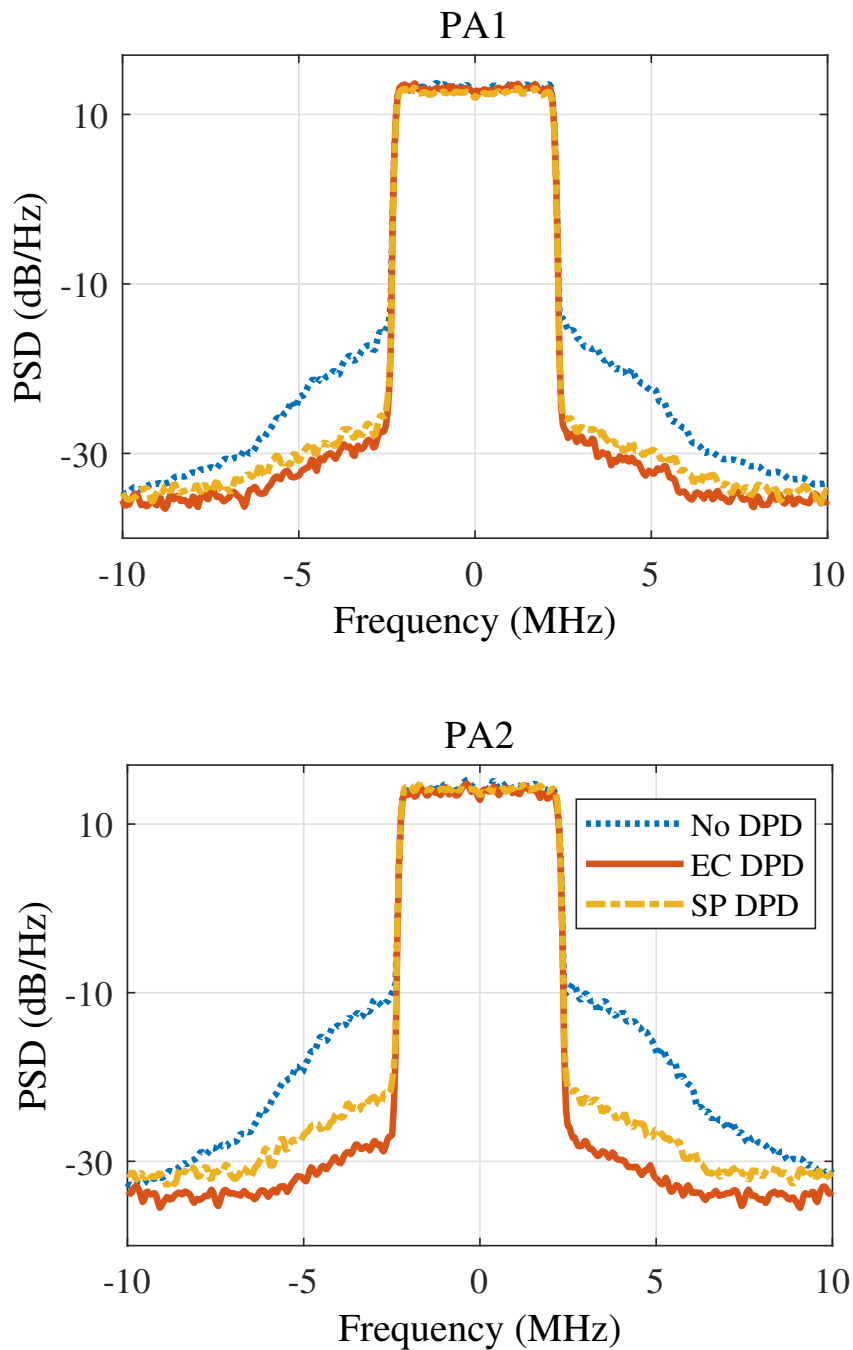


Fig. 6.10 Spectra of the linearized PAs. The figure shows the results without DPD, with the single frequency S-parameters DPD (SP DPD) and with the estimated coupling technique DPD (EC DPD).

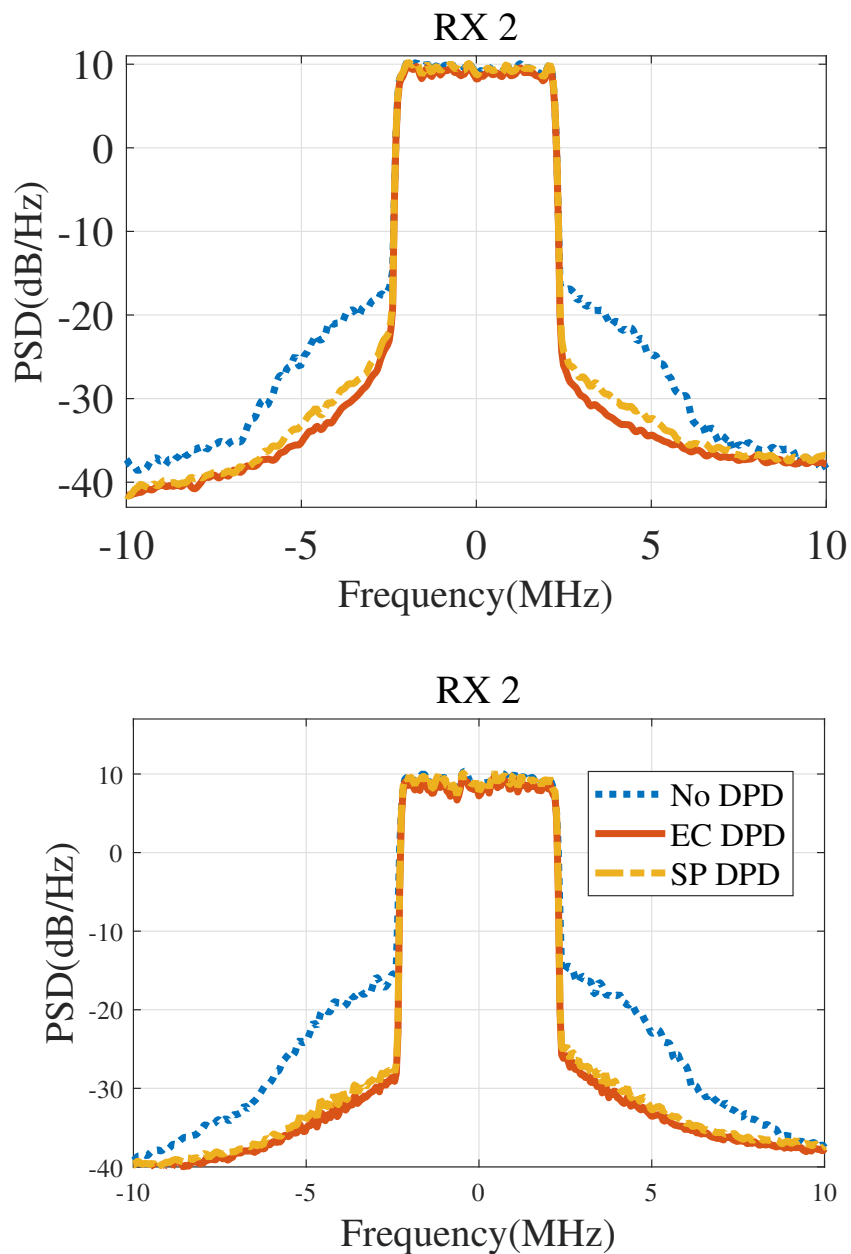


Fig. 6.11 Spectra of the linearized received signals. The figure shows the results without DPD, with the single frequency S-parameters DPD (SP DPD) and with the estimated coupling technique DPD (EC DPD).

Chapter 7

Digital Predistortion for Phased Arrays

The work presented in this chapter relates to the conference proceeding [88] and [123].

Beamforming is one of the transmission modes in MIMO communication. It enables directive communication by shaping the transmitted beam pattern. Hence, the array gain and diversity gain are improved in a particular direction. The hybrid beamforming is a variant of MIMO system which incorporate the advantage of beamforming in MIMO systems. The beamforming is carried out by transmitting the same signal from several antennas. Particularly, phased array shapes the radiated signal pattern by varying the amplitude and the phase of the radiated signal from several antennas. The block diagram of a phased array is represented in Fig. 7.1. When the beamforming parameters are implemented in RF analog, a single digital baseband signal is fed to several RF transmitters.

A typical implementation of the digital predistortion (DPD) technique is done in digital baseband and requires as many feedback paths and predistorders as the number of power amplifiers. However, for phased array systems where one digital baseband branch is connected to several analog transmission paths in RF, only a single DPD can be implemented per sub-array. This single DPD is expected to

linearize several PAs, each of which can have different characteristics. Different strategies can be applied to optimize the single DPD performance. In [90], the authors propose a single DPD technique to linearize multiple PAs in a phased array. Their proposed solution relies on minimizing the sum of the least squared errors of the different branches. A beam-oriented single DPD is introduced in [91] where a single DPD is employed to linearize the main beam signal. The proposed DPD is based on minimization of the least square error of the superposition of the PA outputs after the effect of analog beamformers are removed. An array DPD was introduced by [92], where the combined error in the far-field is minimized. The combined error is estimated by taking the feedbacks from all PAs and calculating the combined response of the array in the far-field and comparing it with the input signal to the PAs. The work in [93] is using the same approach by canceling the beamforming weights before combining via an anti-beamforming module. Further, the effect of phase and amplitude mismatch of feedback signals on the DPD learning algorithm has been investigated. In [94], a single DPD is trained to linearize the sub-array by modeling the main beam signal and comparing it with the input signal and observe the signal linearity in the far-field.

In this chapter, we perform a comparative study among different single DPD solutions for phased array systems with combined feedback response and with individual PA feedback responses. By proposing a novel single DPD method, we formulate a convex optimization problem which relies upon on joint minimization of the cost functions from all transmission branches. We demonstrate that the proposed solution outperforms the ones in [90–94]. This improved performance is especially notable when the PAs in the different branches possess considerably different characteristics. The DPD learning utilizes a closed-loop estimation technique which is not sensitive to the PA output noisy measurements.

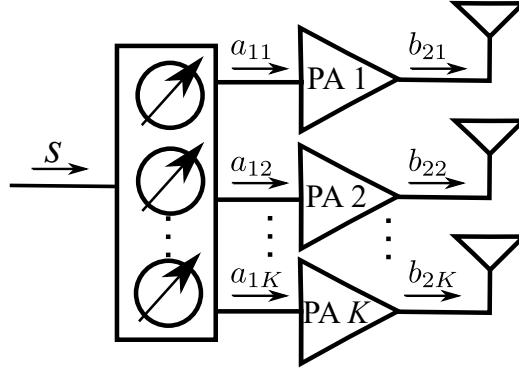


Fig. 7.1 Block diagram of a phased array.

7.1 Single DPD System Model

A block diagram of analog beamforming phased array with a single DPD is depicted in Fig.7.2. The PA outputs can be obtained using a shared feedback path connected to each transmission path by a switch. To have access to all PA outputs, time sharing can be used. The complex baseband equivalent of the PA output can be written as a polynomial model [124]. The nonlinear memory effects are typically weaker than the nonlinearities without memory [125], and we omit the memory effect here, but it is easy to generalize to memory if desired. The baseband equivalent of each PA output in the i th transmission path when no DPD is applied can be expressed as

$$b_{2i}(n) = v_i \phi_s^T(n) \boldsymbol{\theta}_i, i = 1, \dots, N_T, \quad (7.1)$$

where N_T is the number of PAs, $\phi_s(n) = [s(n), s(n)|s(n)|^2, \dots, s(n)|s(n)|^{p_i-1}]^T$ is the basis waveform and v_i represents the analog beamforming phase shifters in the i th transmitter path. The vector $\boldsymbol{\theta}_i$ denotes the i th PA model impulse response and p_i is the order of nonlinearity in the i th PA. In a multi-transmitter system, the individual PAs have different non-linearity characteristics that can be presented by different model coefficients. However, the combined response of the array still can be modeled with a single polynomial. Given this fact, the single DPD for a sub-array can be

modeled in the form of a polynomial as

$$s_{\text{DPD}}(n) = \boldsymbol{\phi}_s^T(n) \boldsymbol{\varphi}, \quad (7.2)$$

where $\boldsymbol{\varphi} \in \mathbb{C}^{p \times 1}$ is the vector of the DPD coefficients for the basis waveform $\boldsymbol{\phi}_s(n) = [s(n), s(n)|s(n)|^2, \dots, s(n)|s(n)|^{p-1}]^T$. The model is linear in $\boldsymbol{\varphi}$, and thus the model can be fitted with the least squares approach. Utilizing a DLA or closed-loop learning DPD, to obtain the optimum DPD coefficients, the difference between the desired output signal and the actual PA output is obtained as

$$e_i(n) = \frac{1}{G_i} \tilde{b}_{2i}(n) - s(n), \quad (7.3)$$

for each path where G_i is the complex linear gain of the i th PA. The linear gain of the PA can be known by using the least square approach between the PA input and output. The phase offsets in output feedback signals are introduced by analog phase shifters which can degrade the performance of the single DPD. Thus, the phase offsets must be taken into account prior to DPD learning either by canceling the effect of phase shifters in the feedback path or modeling the equivalent far-field model of individual PA outputs. Modeling the output signals in the far-field can limit the performance of DPD to a specific direction while, counteracting the effect of phase shifters in the feedback signals, facilitates the adoption of trained DPD coefficients for different steering directions or dynamic steering. Thus, we suggest a phase correction such that the signal $\tilde{b}_{2i}(n)$ is obtained as

$$\tilde{b}_{2i}(n) = v_i^* b_{2i}(n), \quad (7.4)$$

where v_i^* is complex conjugate of the the analog beamforming phase shifters in the i th transmit branch. By multiplying the PA outputs with v_i^* , the effect of phase shifters can be canceled. In the closed-loop learning, the estimation loop contains the DPD block. As it was explained in Section 2.8.1.2, the estimated parameter corresponds to the residual error in the DPD coefficients [126]. For a block of time

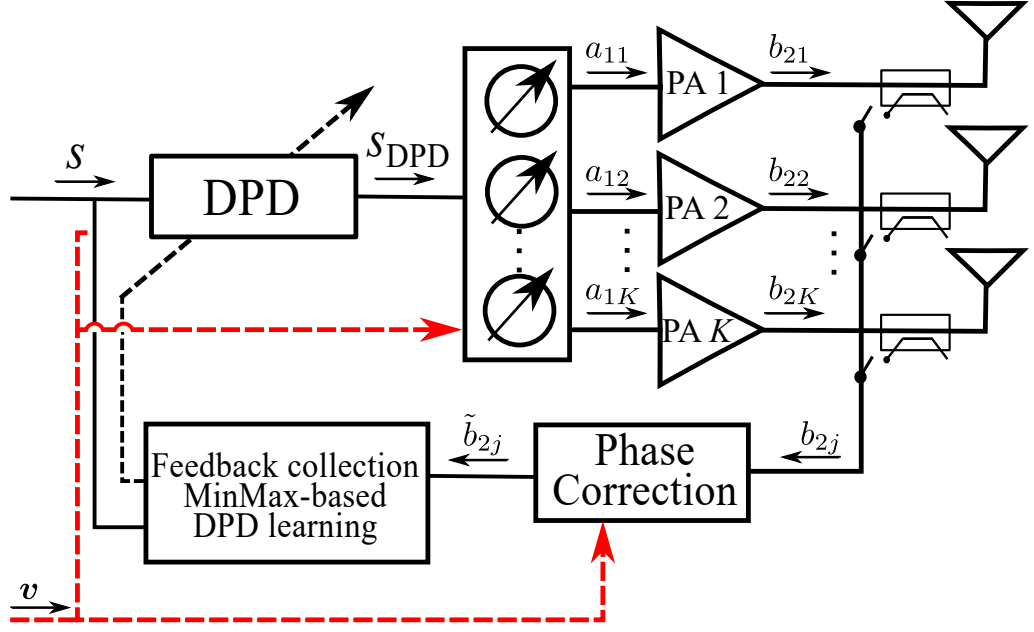


Fig. 7.2 Block diagram of a sub-array to access each PA units output with shared feedback.

samples, the cost function to be minimized reads as

$$J_{\text{CL}} = \|\mathbf{e}_i - \Phi_s^T \Delta\varphi\|_F^2, \quad (7.5)$$

where $\Delta\varphi \in \mathbb{C}^{p \times 1}$ is the vector of the residual model coefficients, p represents the order of nonlinearity and $\|\cdot\|_F$ represents the Frobenius norm. Through a few iterations the DPD coefficient can be updated. First, by using the least-squares technique, the estimation of coefficient residual is obtained as

$$\Delta\varphi = (\Phi_s)^{\dagger} \mathbf{e}_i, \quad (7.6)$$

where the matrix Φ_s contains the blocks of time samples of basis waveforms and $(\Phi_s)^{\dagger} = (\Phi_s^H \Phi_s)^{-1} \Phi_s^H$ is the pseudoinverse. Then, the coefficients are updated as follows

$$\varphi^{i+1} = \varphi^i + \Delta\varphi, \quad (7.7)$$

where $\varphi^0 = [1, 0, \dots, 0]$.

7.2 Beamforming DPD with MinMax

Various studies have used different methods to estimate single DPD coefficients. These can be classified in two categories, combined output of the array response [91–94] or Combined Feedback DPD, and the sum over the least square errors [90] or Sum of Errors DPD. First, we present these two methods in a closed-loop learning form. Then, we propose a novel DPD method, noted as MinMax DPD. Finally, we perform a comparison between these three DPD methods. It has been shown in [127] that the out-of-band radiations are not dominant in the directions other than the direction of UE. This is the primary motivation behind the Combined Feedback DPD as it considers the combined response of the array in far-field. Combined Feedback DPD can be implemented either via a combined feedback receiver signal [91, 93] or by modeling the combined far-field signal [92, 94]. In both techniques, the effect of analog phase shifters is removed before DPD coefficients learning. To minimize the array error with respect to the far-field combined signal, a large block of error samples can be obtained by comparing the combined the far-field signal at the position of UE and the input signal. In order to calculate far-field combined signal, the feedback signals are co-phased and combined. An alternative approach is to model the far-field response of the array. Combined Feedback DPD is based on the minimization of the following statement

$$\arg \min_{\Delta \boldsymbol{\varphi} \in \mathbb{C}^{p \times 1}} \left\| \left(\frac{1}{G_A} \sum_{i=1}^{N_T} \tilde{\mathbf{b}}_{2i} - \mathbf{s} \right) - \boldsymbol{\Phi}_s^T \Delta \boldsymbol{\varphi} \right\|_F^2, \quad (7.8)$$

where G_A represents the array linear gain and the signals $\mathbf{s} = [s(n), s(n-1), \dots, s(n-k)]^T$ and $\mathbf{b}_{2i} = [b_{2i}(n), b_{2i}(n-1), \dots, b_{2i}(n-k)]^T$.

Another approach, Sum of Errors DPD, is introduced in [90], minimizes the sum over the least square errors, i.e., the sum of cost functions in (7.5) is minimized as

$$\arg \min_{\Delta \boldsymbol{\varphi} \in \mathbb{C}^{p \times 1}} \sum_{i=1}^{N_T} \left\| \left(\frac{1}{G_i} \tilde{\mathbf{b}}_{2i} - \mathbf{s} \right) - \boldsymbol{\Phi}_s^T \Delta \boldsymbol{\varphi} \right\|_F^2. \quad (7.9)$$

In this approach, the error signal for each PA output signal is computed individually and the sum of them is minimized to obtain the optimum solution for φ . For the sake of consistency we perform co-phasing of the PA output signals in the same way it has been implemented for Combined Feedback DPD. Exploiting triangle inequality, it can be inferred that the performance of (7.8) outperforms (7.9) in the desired direction [92]. However, in both techniques, the PA output with the most deviation from the reference signal $x(n)$, has the dominant contribution in the cost function minimization. Consequently, by linearizing the highly nonlinear PAs, the PAs with lower nonlinearity order heavily expand and degrade the combined performance of the array [92]. To address this issue, we propose a novel strategy by utilizing individual cost functions. The model coefficients must then be estimated to minimize all the cost functions up to an acceptable range. In order to minimize all the cost functions jointly, we formulate a convex optimization problem as

$$\arg \min_{\Delta \varphi \in \mathbb{C}^{p \times 1}} \max_{i=1, \dots, N_T} \left\| \left(\frac{1}{G_i} \tilde{\mathbf{b}}_{2i} - \mathbf{s} \right) - \Phi_s^T \Delta \varphi \right\|_F^2, \quad (7.10)$$

where the model coefficient residuals, $\Delta \varphi$ is the variable to optimize. A careful reader must notice that this optimization problem does not imply minimization of one cost function related to the most nonlinear PA. Instead, (7.10) performs an optimization where the maximum joint error is minimized. Introducing an auxiliary variable d representing the minimum Euclidean distance, the optimization problem in (7.10) can be equivalently written as

$$\begin{aligned} & \underset{\Delta \varphi \in \mathbb{C}^{p \times 1}, d \in \mathbb{R}}{\text{minimize}} && d \\ & \text{subject to} && \left\| \left(\frac{1}{G_i} \tilde{\mathbf{b}}_{2i} - \mathbf{s} \right) - \Phi_s^T \Delta \varphi \right\|_F^2 \leq d, \quad i = 1, \dots, N_T. \end{aligned} \quad (7.11)$$

It can be seen that in the above formulation the quadratic constraints that represent the minimum Frobenius norm squared, are convex with respect to φ . Also, the object d is convex with respect to φ . Thus, the above standard optimization problem can be efficiently solved using standard techniques [128]. We used CVX, a Matlab-based

modeling system for convex optimization, to specify and solve the convex problem in (7.11) [129, 130].

7.3 Simulation Results

As a proof of concept, we perform quantitative performance analysis. The system level simulation for a sub-array with four transmit antennas in a uniform linear array (ULA) with the spacing of half wavelength is implemented in Matlab. In all experiments, the PAs are modeled with a memoryless complex polynomial. First, the PA models for a 3rd and 5th order polynomials are estimated. Then, we obtain the models for the PAs in the adjacent branches by adding a small perturbation to the 3rd and 5th order nonlinearity coefficients such that different PA behaviors are obtained while retaining the similar input-output nonlinear characteristics and linear gain for all PAs. Orthogonal frequency-division multiplexing (OFDM) signal with 5 MHz bandwidth is used where clipping is applied to the input signal to obtain peak-to-average power ratio (PAPR) of 8.5 dB before linearization. To evaluate the performances, the adjacent channel leakage ratio (ACLR) is used to calculate the out-of-band radiation of the distortion in the adjacent channels due to the nonlinearity in the system. The ACLR for a signal $x(n)$ is formulated as

$$\text{ACPR} = \max_{m=L,U} \left\{ \frac{\sum_{f(\text{adj})_m} |X(f)|^2}{\sum_{f(\text{ch.})} |X(f)|^2} \right\}, \quad (7.12)$$

Table 7.1 ACLR (dB) evaluation of three different DPD methods for different PA models.

DPD method	3rd Order PA model	5th Order PA model
Sum of Errors	-39.91	-27.58
Combined Feedback	-41.65	-33.56
MinMax	-43.65	-41.66

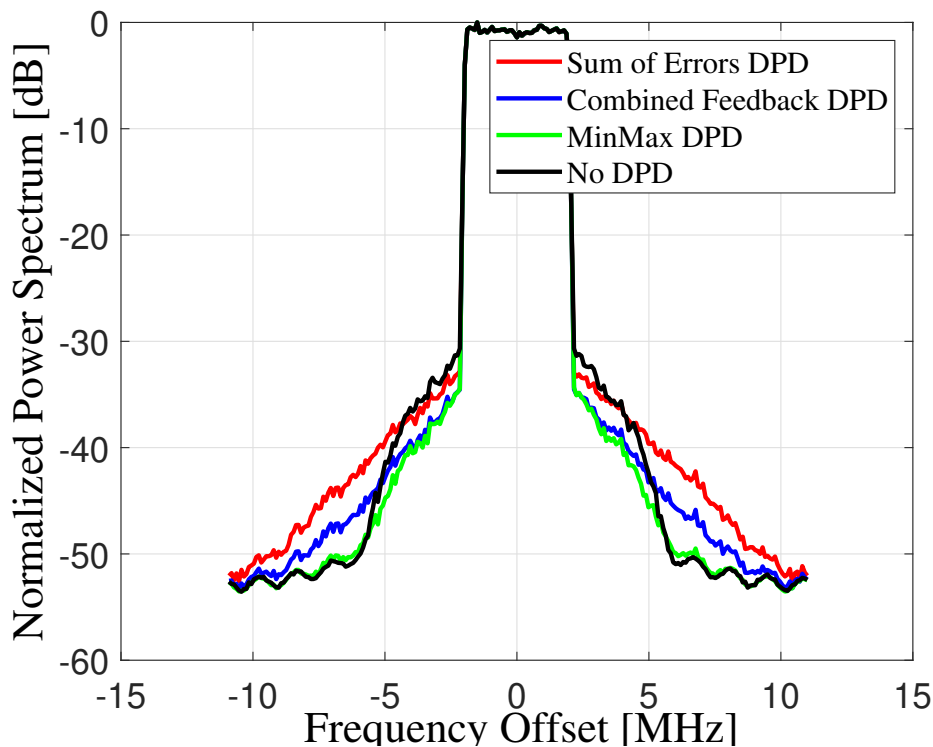


Fig. 7.3 Spectra of the combined array response in the far-field for different DPD methods with PA model of 3rd order polynomial.

where $X(f)$ denotes the power spectrum of $x(n)$ and $f(adj)_m$ represents the frequencies in lower (L) and upper (U) adjacent channels. The fch represents the inband frequencies. The results for the DPD training of $N = 12500$ samples are presented.

The combined far-field response of array is studied when three different DPDs are implemented and trained for the sub-array when the steering angle is set to 30° . In Fig. 7.3 and Fig. 7.4 the power spectral densities (PSD) of the overall array are depicted for 3rd and 5th order nonlinearity with three different DPDs. Clearly, MinMax DPD outperforms Combined Feedback and Sum of Errors DPDs. To quantitatively study the performances, the ACLR results are presented in Table 7.1. For 3rd order polynomial, the MinMax performs on average 2.82 dB better in ACLR measurements. However, as the polynomial order increases to 5, MinMax DPD outperforms the two other DPD by 11 dB on average. Comparing 3rd and 5th order nonlinear models, MinMax performance does not degrade more than 2

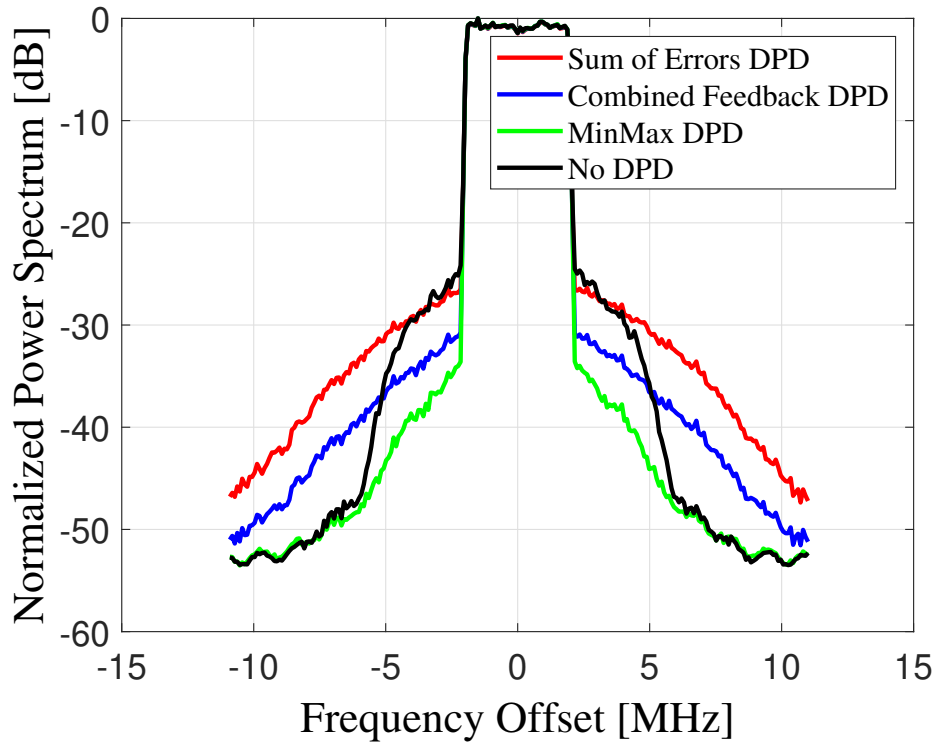


Fig. 7.4 Spectra of the combined array response in the far-field for different DPD methods with PA model of 5th order polynomial.

dB while the ACLR for Combined Feedback DPD worsens by 8 dB and Sum of Errors DPD by 12.33 dB. The reason that the MinMax DPD performance does not degrade considerably by increasing the nonlinearity order of the PAs is due to the fact that MinMax DPD does not depend on the superposition of signals. Rather, the MinMax consider each error signal individually. However, in the Sum of Errors DPD, as the nonlinearity increases the superposition of error signals results in performance degradation. In Combined Feedback DPD, the combined far-field signal deviates further from the input signal as the nonlinearity of the PAs increase.

In Fig. 7.5, the AM/AM response of individual PAs and the combined effect of the three different DPD approaches are presented. It is evident that the MinMax approach results in considerably more linear behavior of the signal in far-field. In the simulations, it was observed that for the PA model with the 3rd order nonlinearity, when no DPD is applied, the combined response of the array shows significant

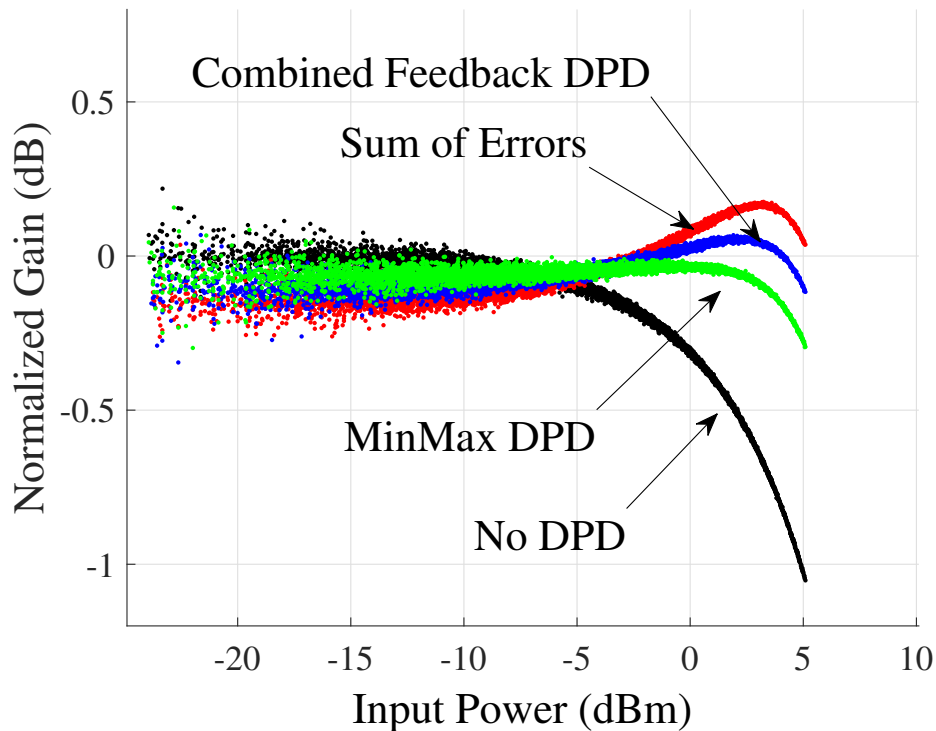


Fig. 7.5 AM/AM plots for combined array far-field responses without DPD and with three different DPD methods with 3rd order PA models.

linearity. This is because the nonlinearities in different PAs can cancel each other out in the far-field. However, when no DPD is applied, the linear gain of the array degrades as it is shown in Fig. 7.5. By implementing the DPD, the combined response of the signal retains the linear gain thus improving the efficiency. In this sense, MinMax DPD achieves best linearization while sustaining the linear gain of the array.

7.4 Measurement Results Under PA Amplitude Variations

One of the common techniques to reduce the sidelobe level (SLL) of the created beam is the amplitude tapering. In this technique different levels of signal power are fed to the PAs across the array. As a result, the PAs across the array have different

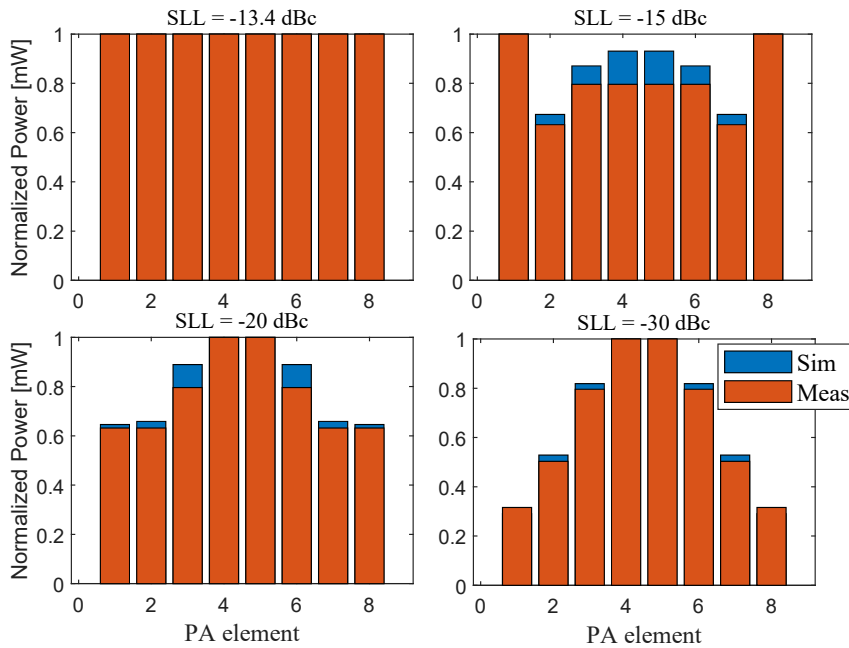


Fig. 7.6 PA input power weights of a 8-element uniform linear array to achieve SLL = -13.4 dBc, -15 dBc, -20 dBc and -30 dBc. The simulated power distributions are presented in blue and the actual power distribution in measurement test bench are presented in red.

behavior. To study the effect of amplitude tapering on linearization performance, Taylor distribution for 8-element uniform linear array (ULA) with the spacing of $\lambda/2$ at SLL of -15 dBc, -20 dBc, -30 dBc are simulated and shown in Fig. 7.6. In measurement setup, the distribution of power amplitude can be implemented by adding attenuators at the input of PAs.

7.4.1 Measurement Setup

Fig. 7.7 shows the measurement setup to linearize four PAs with a single DPD. To evaluate the DPD performances, an OFDM signal with 5 MHz bandwidth with PAPR of 8.5 dB was sent at the carrier frequency of 2.12 GHz using a vector signal generator (R&S SMW200A). The bandwidth is wide enough to excite the dynamic effects of the PAs. The generated signal is then fed to a 4-way power divider and four class AB PAs (BLP7G22S-10P), and the PA outputs are captured by an oscilloscope (R&S

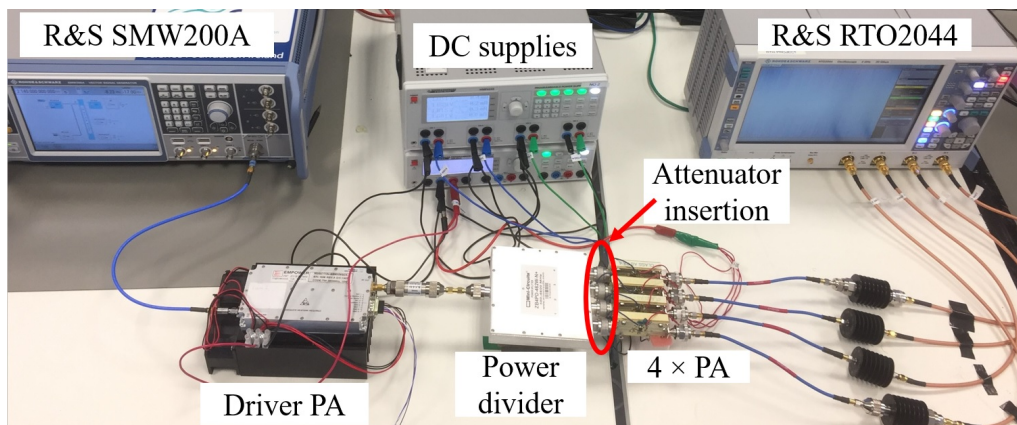


Fig. 7.7 Photograph of the test setup.

RTO2044) and down-converted to baseband. A memory polynomial with the deepest memory of $M = 3$ and the highest nonlinearity order of $P = 9$ across the PAs are used to form the basis functions. The effect of phase shifters is emulated in baseband, which merely implies setting them to zero, i.e., considering the ULA broadside. Hence, the effect of beam steering on individual PA nonlinearity characteristics when the antenna exhibits mutual coupling is not considered in this study. Nonetheless, the results in this study are still valid in terms of PA characteristic variations across the array.

As it is shown in Fig. 7.6, the relative power distribution in ULA array allows for exploitation of symmetry such that half of the weights, i.e., elements one to four, are used to excite four PAs. The measured PA outputs are then mirrored and used to form an 8-element array.

The amplitude variations are applied by adding attenuators with the accuracy of 1 dB at the input of the PAs, as is highlighted in Fig. 7.7. The achieved power distribution for each PA slightly differs from the simulated power distribution (see Fig. 7.6). Therefore, the resulting SLLs are expected to be different from the targeted levels. The nonlinearity of the PAs is the other factor that can affect the achievable SLL reduction because the PAs driven into the nonlinear region can compress the output signal.

The amplitude variations are applied by adding attenuators with the accuracy of 1 dB at the input of the PAs, as is highlighted in Fig. 7.7. The achieved power distribution for each PA slightly differs from the simulated power distribution (see Fig. 7.6). Therefore, the resulting SLLs are expected to be different from the targeted levels. The nonlinearity of the PAs is the other factor that can affect the achievable SLL reduction because the PAs driven into the nonlinear region can compress the output signal.

7.4.2 Measurement Results

Fig. 7.8 presents the radiation patterns for the cases with different SLLs. When no SLL reduction is implemented, i.e., the uniform distribution of the amplitude weights, SLL of -13.4 dBc is expected and achieved (Fig. 7.8a). As it was expected and explained earlier, the cases with SLL of -15 dBc, -20 dBc and -30 dBc are not achieving the targeted levels due to the limited accuracy of the attenuators.

The DPD performances are presented in the form of adjacent channel power (ACP) in Fig. 7.8. The gain normalization per PA output is performed for DPD training. The array far-field radiation pattern is calculated in MATLAB by using the measured PA outputs. In order to illustrate the nonlinear behavior of the array, the ACP in the far-field is calculated when no DPD is implemented and when three different DPDs are implemented.

The slight changes in tapering weights for SLL of -15 dBc results in lower ACP in every direction in Fig. 7.8b compared to the uniform distribution of weights in Fig. 7.8a. The performance of Comb DPD and SumErr DPD are similar, and they outperform the MinMax DPD, which is expected due to the relatively similar behavior of the PAs. By increasing the amplitude variations for SLL of -20 dBc and -30 dBc, the MinMax DPD yields an enhanced performance compared to the two other DPDs. We noticed that the ACP, with no DPD, is slightly reduced in Fig. 7.8d. It can be explained by the fact that the amplitude weights of PA 1 and PA 2 are reduced to satisfy the SLL of -30 dBc. As a result, these PAs are operating

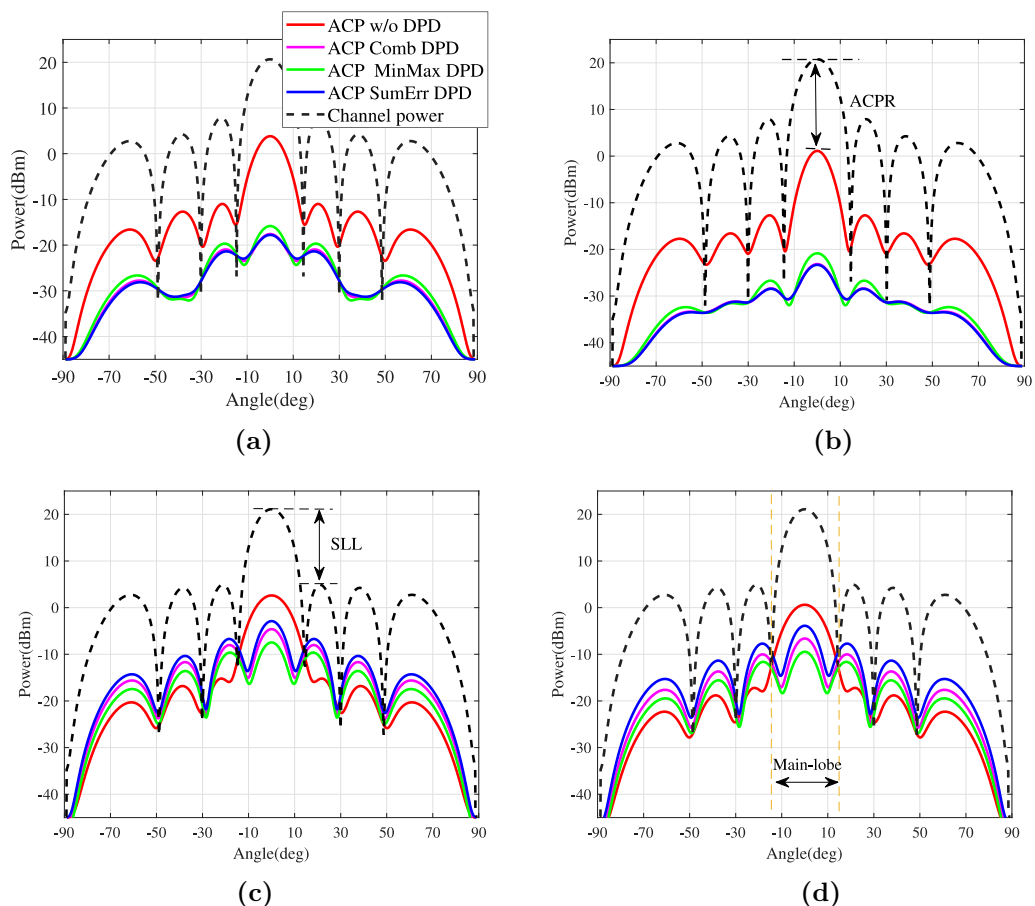


Fig. 7.8 Channel power and ACP of combined feedback (Comb DPD), joint optimization (MinMax DPD), and sum of the errors (SumErr DPD) for: (a) uniform power distribution, (b) SLL = -15 dBc, (c) SLL = -20 dBc, (d) SLL = -30 dBc.

with backoff, which reduces the ACP. In contrast to Fig. 7.8a and 7.8b, for cases of SLL -20 dBc and -30 dBc, the ACP in other spatial directions is increased after the DPD is implemented. The ACP in the main lobe and sidelobes are nearly level for MinMax DPD, which is not aligned with the original pattern of ACP before DPD implementation.

7.5 Conclusion

In this chapter, we proposed a novel technique for training a single DPD for linearization of a phased array. The proposed DPD implements a joint minimization of cost functions corresponding to individual PAs which is an effective method to obtain

a linear combined response of an array. Our numerical results demonstrated that the proposed DPD technique is highly effective when there is a significant deviation in PA behaviors. With simulations, we showed that as the nonlinearity order in PAs increases, the proposed DPD sustains its linearization while the other methods undergo significant performance degradation. Our numerical results demonstrated that by using the proposed DPD technique, for the PA models with the 5th order nonlinearity, the MinMax DPD outperforms the state-of-the-art solutions. We showed that in comparison to Combined Feedback DPD, the MinMax DPD has a better performance of 8.1 dB in the ACLR measurements and outperforms Sum of Errors DPD by 14 dB. For the 3rd order PA models, the combined far-field signal without DPD shows linear performance where the nonlinearities cancel each other out but the linear gain of the array drops by combining the linear PAs with heavily nonlinear PAs. In an experimental measurement setup, we tested the aforementioned DPD techniques by exploiting the amplitude variation to achieve SLL reduction. By implementing the amplitude variation, we changed the PAs behavior across the array. Different linearization algorithms are tested. The measurement results indicate that a slight variation of amplitude can result in improved performance of DPD. However, when the distribution of the amplitudes has a wide variation, linearization performance is degraded, and the peaks of ACP are generated in sidelobes. The performance of different phased array DPDs are aligned with the simulation results, showing the improvement in performance when the MinMax DPD is used.

Chapter 8

Conclusion

8.1 Conclusions

Growing demand for different forms of communication and different applications of communication systems has triggered the development of several technologies. To satisfy user demand for higher data rates, and the capacity of the communication system, the smart use of the limited spectrum is imperative. Multiple-input multiple-output (MIMO) technology will continue to play a vital role in next-generation wireless systems, e.g., the fifth-generation wireless networks (5G). Large-scale antenna arrays (also called massive MIMO) seem to be the most promising physical layer solution for meeting the ever-growing demand for high spectral efficiency.

This thesis addresses the challenges in compensation of distortion in MIMO systems. The effect of crosstalk distortion on digital predistortion (DPD) in MIMO system is investigated in Chapter 4. Two different learning algorithm are studied, i.e., indirect learning algorithm (ILA) and direct learning algorithm (DLA). The simulation results show the advantage of using DLA in terms of linearization and complexity, when MIMO system suffers from crosstalk.

By increasing the size of the MIMO systems, the cost and area of the system become a concern. Therefore, system designers seek efficient hardware and signal processing solutions. The conventional technique for mitigation of the distortion due

to the power amplifier (PA) must be modified as well. In this thesis, a technique to reuse the hardware in MIMO time division duplex (TDD) systems for DPD implementation is proposed in Chapter 5 and Chapter 6. The technique is developed by utilizing over-the-air (OTA) intra-array measurements. One of the essential components of a DPD module is a transmitter observation receiver (TOR) to capture the PA output signal and provide the baseband representation of it. This means that each transmitter requires a separate complete receiver chain. MIMO TDD systems are equipped with transceivers where each transceiver has its dedicated RF transmitter and receiver operating in the same frequency band and sharing the same antenna element. This technique is enabled based on channel reciprocity in TDD systems.

Firstly, we developed a scheme to identify the intra-array channels, i.e., the coupling between the antenna elements in Chapter 5. The channel between the transmitter and the TOR antenna must be known when the linearization must be done per transmit branch. This technique is based on consecutively transmitting from different antennas and receiving the signals by the other antennas. To the best of our knowledge, previous similar works did not perform linearization per transmitter. Also, the intra-array coupling estimation, solely based on on-site measurements, has never been done similarly. This thesis compares the proposed effective coupling estimation with scattering parameters (S-parameters) measurements of the array. However, since the S-parameter measurements are usually conducted in a well-calibrated environment with a 50Ω matched setup, they cannot correctly represent the intra-array coupling. This makes the proposed technique more accurate in practical use. In addition, the assumptions in our proposed effective coupling estimation are examined in simulations and experimental setup. The results indicate an acceptable margin to make an assumption, such as similar receiver characteristics. It has been demonstrated that a deviation of less than 1 dB can be achieved with the proposed technique, which is an acceptable margin on our experimental setup.

Secondly, a linearization scheme is developed based on a model-based indirect learning (MILA) approach in Chapter 6. In this scheme, several transmitted signals

are captured with the OTA TOR when the transmitted signals are not fully correlated. Individual PA models are estimated via an iterative procedure. By conducting the PA models, linearization is performed based on the estimated model. This technique is superior to similar linearization based on shared TOR, where the signals are captured with directional couplers at the PA output. In MILA based techniques, the associated noise in the measured signal is avoided in linearization iterations. Our proposed linearization technique is finally experimentally validated on a 2×2 MIMO test bench. The results showed an overall improvement of 19 dB in terms of NMSE. The proposed technique is compared with the case when the S-parameters substitute the coupling between the antenna elements. The results indicate that by utilizing the proposed effective coupling estimation in OTA DPD, the NMSE is improved about 6 dB compared to the case in which the S-parameters are used.

Finally, in Chapter 7, the phased array linearization is visited in this thesis, which is an essential subsection of future MIMO systems for directive communication in millimeter wave bands. Hardware architectures such as hybrid beamforming take advantage of phased arrays. The main idea of phased arrays is to transmit the same data stream on each antenna element with varying phase and/or amplitude. Therefore, all RF transmit paths are sharing the same baseband digital signal when the amplitude and phase variations are implemented in analog RF. Hence, the linearization via DPD can be performed such that a single DPD linearizes the response of several RF PAs. The challenge of phased array PAs having varying characteristics has not been adequately addressed in the literature. The use of the minimax optimization technique has been investigated in this thesis. In this regard, we seek to continuously perform optimization to achieve the most effective DPD coefficient to linearize several PAs with a high degree of variation between their behavioral models. We further investigated the effectiveness of this technique by increasing the nonlinearity model from 3rd order to 5th order. The compared results with the conventional single DPD techniques reveal the effectiveness of our proposed single DPD based on minimax optimization. The proposed technique, then is examined in an experimental setup, where the effect of amplitude variation on the

proposed technique and the conventional techniques was studied. The results are inline with the simulations.

In summary, this thesis makes a contribution to distortion mitigation in MIMO systems. Signal processing techniques have been successfully applied to compensate for RF distortions in MIMO systems suffering from crosstalk with reduced complexity of RF hardware systems. Hence, the proposed techniques facilitate the implementation of future wireless communication systems with feasible and sustainable solutions.

8.2 Future Work

The work presented in this thesis considers a limited set of existing problems in modern wireless communication systems. There are still areas that must be considered and addressed in future research. The possible future extension of this work is listed as, but not limited to:

The technique presented in this thesis to estimate the effective coupling only considers the antennas in which their bandwidth is wide compared to the transmitted signal bandwidth. Therefore, it is necessary to present a dynamic model for the effective coupling for those antennas with bandwidth similar to the transmitted signal bandwidth.

The proposed MILA-based OTA DPD technique in Chapter 6 requires at least two receiver antennas to act as OTA TOR. A useful continuation of the technique presented in this chapter can incorporate a possible regularization step in order to prevent the overfitting problem in PA model identification using the OTA measurements. We make a note that for large-scale arrays, the position and number of receiver antennas can vary and must be studied carefully.

The theory presented in Chapter 7 to linearize the phased arrays, only considered a narrow-band modeling strategy. Hence, this work can be extended to incorporate wider bandwidth signals in phased array linearization.

To meet the demand for high-speed wireless communication in 5G, millimetre Wave (mm-Wave) communication is being seen as a promising candidate. For the bands over the 24 GHz, the radios will require partly novel techniques to operate in mm-Wave and there will be more widespread use of massive MIMO, beamforming and highly integrated antenna systems. The proposed techniques in Chapter 5, Chapter 6 and Chapter 7, are experimentally examined in sub-6 GHz bands due to the limitations in laboratory. However, the proposed techniques are initially designed to tackle the issues in mm-Wave massive MIMO systems and anticipated to be adopted in mm-Wave frequency bands. Future works includes experimentally validate this assumption.

The advancement of machine learning in communication opens doors to new fields to be explored in wireless systems. As the signal bandwidth increases, the Volterra-based models used in this thesis, become complex. Furthermore, for wideband signals, the distorted terms become correlated, results in rank deficiency problems in conventional modeling techniques. Future works can incorporate neural network approaches to address these issues in ultra-wideband wireless systems.

Appendix A

Matrix Representation of Ψ for Effective Coupling Single Estimation

In Single Estimation technique, the matrix Ψ is built from a sequence of received signals in a K elements array. Accordingly, Ψ is presented as follow

$$\Psi_{\text{single}}^{(i)} = \begin{bmatrix} (K - i - 1) \|\mathbf{y}_{(i-1)i}\|^2 & -\mathbf{y}_{(i-1)i}^* \mathbf{y}_{(i+1)i} & \cdots & -\mathbf{y}_{(i-1)i}^* \mathbf{y}_{Ki} \\ -\mathbf{y}_{(i+1)i}^* \mathbf{y}_{(i-1)i} & \vdots & \cdots & -\mathbf{y}_{21}^* \mathbf{y}_{Ki} \\ \vdots & \vdots & \ddots & \vdots \\ -\mathbf{y}_{Ki}^* \mathbf{y}_{(i-1)i} & \cdots & \cdots & (K - i - 1) \|\mathbf{y}_{Ki}\|^2 \end{bmatrix}, \quad (\text{A.1})$$

where $\forall i = 2, \dots, K - 1$ and \mathbf{y}_{nm} represents the vector of received signal at n th antenna when m th antenna is transmitting and $\|\cdot\|$ is the norm operator and $*$ represent the conjugate of the signal. For the i th step of iteration the $\Psi_{\text{single}}^{(i)}$ is recalculated.

Appendix B

Matrix Representation of Ψ for Effective Coupling Joint Estimation

When the reference antenna is in close proximity of all antenna elements, the matrix Ψ for joint estimation is presented as

$$\Psi_{\text{joint}} = \begin{bmatrix} \|\mathbf{y}_{1r}\|^2 & -\mathbf{y}_{1r}^* \mathbf{y}_{2r} & 0 & 0 & \cdots & \cdots & 0 \\ -\mathbf{y}_{2r}^* \mathbf{y}_{1r} & \|\mathbf{y}_{2r}\|^2 & 0 & 0 & \cdots & \cdots & 0 \\ \|\mathbf{y}_{1r}\|^2 & 0 & -\mathbf{y}_{1r}^* \mathbf{y}_{3r} & 0 & \cdots & \cdots & 0 \\ -\mathbf{y}_{3r}^* \mathbf{y}_{1r} & 0 & \|\mathbf{y}_{3r}\|^2 & 0 & \cdots & \cdots & 0 \\ \vdots & \vdots & \vdots & \vdots & \ddots & \vdots & \vdots \\ 0 & \cdots & \cdots & \cdots & 0 & \|\mathbf{y}_{(K-2)K}\|^2 & -\mathbf{y}_{(K-2)K}^* \mathbf{y}_{(K-1)K} \\ 0 & \cdots & \cdots & \cdots & 0 & -\mathbf{y}_{(K-1)K}^* \mathbf{y}_{(K-2)K} & \|\mathbf{y}_{(K-1)K}\|^2 \end{bmatrix} \quad (\text{B.1})$$

where K is the number of antenna elements within the array and \mathbf{y}_{nm} represents the vector of received signal at n th antenna when m th antenna is transmitting and $\|\cdot\|$ is the norm operator and $*$ represent the conjugate of the signal. The index r represents the reference antenna.

References

- [1] R. N. Clarke, “Expanding mobile wireless capacity: The challenges presented by technology and economics,” *Telecommunications Policy*, vol. 38, no. 8, pp. 693 – 708, 2014. [Online]. Available: <http://www.sciencedirect.com/science/article/pii/S0308596113001900>
- [2] E. G. Larsson and L. V. der Perre, “Massive MIMO for 5G,” *IEEE 5G Techn. Focus*, vol. 1, no. 1, Mar 2017.
- [3] T. L. Marzetta, E. G. Larsson, H. Yang, and H. Q. Ngo, *Fundamentals of Massive MIMO*. Cambridge University Press, 2016.
- [4] E. Costa and S. Pupolin, “M-QAM-OFDM system performance in the presence of a nonlinear amplifier and phase noise,” *IEEE Transactions on Communications*, vol. 50, no. 3, pp. 462–472, March 2002.
- [5] J. Pedro and B. Carvalho, *Intermodulation Distortion in Microwave and Wireless Circuits*. Norwood: Artech House, 2003. [Online]. Available: <https://cds.cern.ch/record/995354>
- [6] 3GPP, “Technical Specification Group Radio Access Network; NR; Base Station (BS) radio transmission and reception,” 3rd Generation Partnership Project (3GPP), Technical Specification (TS) 36.331, 06 2020, version 16.4.0. [Online]. Available: <https://portal.3gpp.org/desktopmodules/Specifications/SpecificationDetails.aspx?specificationId=3202>
- [7] “Universal mobile telecommunications system (UMTS); base station (BS) radio transmission and reception (FDD),” European Telecommunication Standard Institute, Technical Specification (TS) 36.331, September 2004, version 6.7.0.
- [8] W. H. Doherty, “A new high efficiency power amplifier for modulated waves,” *Proceedings of the Institute of Radio Engineers*, vol. 24, no. 9, pp. 1163–1182, Sep. 1936.
- [9] F. H. Raab, “Efficiency of Doherty RF power amplifier systems,” *IEEE Transactions on Broadcasting*, vol. BC-33, no. 3, pp. 77–83, Sep. 1987.
- [10] F. H. Raab, P. Asbeck, S. Cripps, P. B. Kenington, Z. B. Popovic, N. Pothecary, J. F. Sevic, and N. O. Sokal, “Power amplifiers and transmitters for RF and microwave,” *IEEE Transactions on Microwave Theory and Techniques*, vol. 50, no. 3, pp. 814–826, March 2002.

References

- [11] B. Kim, I. Kim, and J. Moon, "Advanced Doherty architecture," *IEEE Microwave Magazine*, vol. 11, no. 5, pp. 72–86, Aug 2010.
- [12] F. H. Raab, "Efficiency of envelope-tracking RF power amplifier systems," *RF Expo East*, pp. 303–311, November 1986.
- [13] F. Wang, A. H. Yang, D. F. Kimball, L. E. Larson, and P. M. Asbeck, "Design of wide-bandwidth envelope-tracking power amplifiers for OFDM applications," *IEEE Transactions on Microwave Theory and Techniques*, vol. 53, no. 4, pp. 1244–1255, April 2005.
- [14] C. Hsia, A. Zhu, J. J. Yan, P. Draxler, D. F. Kimball, S. Lanfranco, and P. M. Asbeck, "Digitally assisted dual-switch high-efficiency envelope amplifier for envelope-tracking base-station power amplifiers," *IEEE Transactions on Microwave Theory and Techniques*, vol. 59, no. 11, pp. 2943–2952, Nov 2011.
- [15] H. Chireix, "High power outphasing modulation," *Proceedings of the Institute of Radio Engineers*, vol. 23, no. 11, pp. 1370–1392, Nov 1935.
- [16] D. Cox, "Linear amplification with nonlinear components," *IEEE Transactions on Communications*, vol. 22, no. 12, pp. 1942–1945, December 1974.
- [17] M. Faulkner, "Amplifier linearization using RF feedback and feedforward techniques," *IEEE Transactions on Vehicular Technology*, vol. 47, no. 1, pp. 209–215, Feb 1998.
- [18] J. L. Dawson and T. H. Lee, "Automatic phase alignment for a fully integrated Cartesian feedback power amplifier system," *IEEE Journal of Solid-State Circuits*, vol. 38, no. 12, pp. 2269–2279, Dec 2003.
- [19] Y. Y. Woo, J. Kim, J. Yi, S. Hong, I. Kim, J. Moon, and B. Kim, "Adaptive digital feedback predistortion technique for linearizing power amplifiers," *IEEE Transactions on Microwave Theory and Techniques*, vol. 55, no. 5, pp. 932–940, May 2007.
- [20] K. J. Parsons and P. B. Kenington, "The efficiency of a feedforward amplifier with delay loss," *IEEE Transactions on Vehicular Technology*, vol. 43, no. 2, pp. 407–412, May 1994.
- [21] K. Madani, "Reducing the intermodulation distortion in multi-carrier microwave power amplifiers," in *1999 Symposium on High Performance Electron Devices for Microwave and Optoelectronic Applications. EDMO (Cat. No.99TH8401)*, Nov 1999, pp. 153–157.
- [22] R. N. Braithwaite, "Positive feedback pilot system for second loop control in a feedforward power amplifier," *IEEE Transactions on Circuits and Systems I: Regular Papers*, vol. 55, no. 10, pp. 3293–3305, Nov 2008.
- [23] A. Gokceoglu, A. ghadam, and M. Valkama, "Steady-state performance analysis and step-size selection for LMS-adaptive wideband feedforward power amplifier linearizer," *IEEE Transactions on Signal Processing*, vol. 60, no. 1, pp. 82–99, Jan 2012.

-
- [24] J. K. Cavers, "Amplifier linearization using a digital predistorter with fast adaptation and low memory requirements," *IEEE Transactions on Vehicular Technology*, vol. 39, no. 4, pp. 374–382, Nov 1990.
- [25] M. Faulkner and M. Johansson, "Adaptive linearization using predistortion-experimental results," *IEEE Transactions on Vehicular Technology*, vol. 43, no. 2, pp. 323–332, May 1994.
- [26] A. N. D'Andrea, V. Lottici, and R. Reggiannini, "RF power amplifier linearization through amplitude and phase predistortion," *IEEE Transactions on Communications*, vol. 44, no. 11, pp. 1477–1484, Nov 1996.
- [27] J. K. Cavers, "Optimum table spacing in predistorting amplifier linearizers," *IEEE Transactions on Vehicular Technology*, vol. 48, no. 5, pp. 1699–1705, Sep. 1999.
- [28] J. C. Pedro and N. B. De Carvalho, "On the use of multitone techniques for assessing rf components' intermodulation distortion," *IEEE Transactions on Microwave Theory and Techniques*, vol. 47, no. 12, pp. 2393–2402, Dec 1999.
- [29] L. Guan and A. Zhu, "Green communications: Digital predistortion for wide-band rf power amplifiers," *IEEE Microwave Magazine*, vol. 15, no. 7, pp. 84–99, Nov 2014.
- [30] P. L. Gilabert, A. Cesari, G. Montoro, E. Bertran, and J. Dilhac, "Multi-lookup table FPGA implementation of an adaptive digital predistorter for linearizing RF power amplifiers with memory effects," *IEEE Transactions on Microwave Theory and Techniques*, vol. 56, no. 2, pp. 372–384, Feb 2008.
- [31] "Etsi rrs05-024," *Nokia Siemens Networks*.
- [32] R. N. Braithwaite, "A comparison of indirect learning and closed loop estimators used in digital predistortion of power amplifiers," in *2015 IEEE MTT-S International Microwave Symposium*, May 2015, pp. 1–4.
- [33] S. C. Cripps, *RF Power Amplifiers for Wireless Communications, Second Edition (Artech House Microwave Library (Hardcover))*. Norwood, MA, USA: Artech House, Inc., 2006.
- [34] 3GPP, "Technical specifications and technical reports for a UTRAN-based 3GPP system," *TS 21.101, 3rd Generation Partnership Project (3GPP)*, June 2008.
- [35] ETSI TS 136 101, "LTE; evolved universal terrestrial radio access (E-UTRA); user equipment (UE) radio transmission and reception (3GPP TS 36.101 version 14.3.0 release 14)." [Online]. Available: https://www.etsi.org/deliver/etsi_ts/136100_136199/136101/14.03.00_60/ts_136101v140300p.pdf
- [36] J. Kim and K. Konstantinou, "Digital predistortion of wideband signals based on power amplifier model with memory," *Electronics Letters*, vol. 37, no. 23, pp. 1417–1418, Nov 2001.

References

- [37] M. Kazimierczuk, *RF Power Amplifiers*. Wiley, 2008. [Online]. Available: <https://books.google.ie/books?id=dm-HZg99pkIC>
- [38] J. R. Lane, R. G. Freitag, Hyo-Kun Hahn, J. E. Degenford, and M. Cohn, "High-efficiency 1-, 2-, and 4-W Class-B FET power amplifiers," *IEEE Transactions on Microwave Theory and Techniques*, vol. 34, no. 12, pp. 1318–1326, Dec 1986.
- [39] G. Monprasert, P. Suebsombut, T. Pongthavornkamol, and S. Chalermwisutkul, "2.45 GHz GaN HEMT Class-AB RF power amplifier design for wireless communication systems," in *ECTI-CON2010: The 2010 ECTI International Conference on Electrical Engineering/Electronics, Computer, Telecommunications and Information Technology*, May 2010, pp. 566–569.
- [40] A. Juhas and L. A. Novak, "Comments on Class-E, Class-C, and Class-F power amplifier based upon a finite number of harmonics," *IEEE Transactions on Microwave Theory and Techniques*, vol. 57, no. 6, pp. 1623–1625, June 2009.
- [41] F. A. Himmelstoss and K. H. Edelmoser, "High dynamic class-D power amplifier," *IEEE Transactions on Consumer Electronics*, vol. 44, no. 4, pp. 1329–1333, Nov 1998.
- [42] A. J. Wilkinson and J. K. A. Everard, "Transmission-line load-network topology for class-E power amplifiers," *IEEE Transactions on Microwave Theory and Techniques*, vol. 49, no. 6, pp. 1202–1210, June 2001.
- [43] M. A. Reece, C. White, J. Penn, B. Davis, M. J. Bayne, N. Richardson, W. I. I. Thompson, and L. Walker, "A Ka-band class F MMIC amplifier design utilizing adaptable knowledge-based neural network modeling techniques," in *IEEE MTT-S International Microwave Symposium Digest, 2003*, vol. 1, June 2003, pp. 615–618 vol.1.
- [44] W. Bosch and G. Gatti, "Measurement and simulation of memory effects in predistortion linearizers," *IEEE Transactions on Microwave Theory and Techniques*, vol. 37, no. 12, pp. 1885–1890, Dec 1989.
- [45] X. T. Vuong and A. F. Guibord, "Modelling of nonlinear elements exhibiting frequency-dependent AM/AM and AM/PM transfer characteristics," *Canadian Electrical Engineering Journal*, vol. 9, no. 3, pp. 112–116, July 1984.
- [46] J. Staudinger, J. Nanan, and J. Wood, "Memory fading Volterra series model for high power infrastructure amplifiers," in *2010 IEEE Radio and Wireless Symposium (RWS)*, Jan 2010, pp. 184–187.
- [47] H. Ku, M. D. McKinley, and J. S. Kenney, "Quantifying memory effects in RF power amplifiers," *IEEE Transactions on Microwave Theory and Techniques*, vol. 50, no. 12, pp. 2843–2849, Dec 2002.
- [48] J. Chani-Cahuana, P. N. Landin, C. Fager, and T. Eriksson, "Structured digital predistorter model derivation based on iterative learning control," in *2016 46th European Microwave Conference (EuMC)*, Oct 2016, pp. 178–181.
- [49] M. Schetzen, "Nonlinear system modeling based on the Wiener theory," *Proceedings of the IEEE*, vol. 69, no. 12, pp. 1557–1573, Dec 1981.

-
- [50] E. Schurack, W. Rupp, T. Latzel, and A. Gottwald, "Analysis and measurement of nonlinear effects in power amplifiers caused by thermal power feedback," in *[Proceedings] 1992 IEEE International Symposium on Circuits and Systems*, vol. 2, May 1992, pp. 758–761 vol.2.
- [51] M. Schetzen, *The Volterra and Wiener Theories of Nonlinear Systems*. Melbourne, FL, USA: Krieger Publishing Co., Inc., 2006.
- [52] D. R. Morgan, Z. Ma, J. Kim, M. G. Zierdt, and J. Pastalan, "A generalized memory polynomial model for digital predistortion of RF power amplifiers," *IEEE Transactions on Signal Processing*, vol. 54, no. 10, pp. 3852–3860, Oct 2006.
- [53] P. M. Suryasarman and A. Springer, "A comparative analysis of adaptive digital predistortion algorithms for multiple antenna transmitters," *IEEE Transactions on Circuits and Systems I: Regular Papers*, vol. 62, no. 5, pp. 1412–1420, May 2015.
- [54] F. Zhang, Y. Wang, and B. Ai, "Variable step-size MLMS algorithm for digital predistortion in wideband OFDM systems," *IEEE Transactions on Consumer Electronics*, vol. 61, no. 1, pp. 10–15, February 2015.
- [55] Lei Ding, Zhengxiang Ma, D. R. Morgan, M. Zierdt, and J. Pastalan, "A least-squares/Newton method for digital predistortion of wideband signals," *IEEE Transactions on Communications*, vol. 54, no. 5, pp. 833–840, May 2006.
- [56] L. Guan and A. Zhu, "Optimized low-complexity implementation of least squares based model extraction for digital predistortion of rf power amplifiers," *IEEE Transactions on Microwave Theory and Techniques*, vol. 60, no. 3, pp. 594–603, March 2012.
- [57] A. Molina, K. Rajamani, and K. Azadet, "Digital predistortion using lookup tables with linear interpolation and extrapolation: Direct least squares coefficient adaptation," *IEEE Transactions on Microwave Theory and Techniques*, vol. 65, no. 3, pp. 980–987, March 2017.
- [58] Wei Jian, Chongxiu Yu, Jianxin Wang, Jianguo Yu, and Lin Wang, "OFDM adaptive digital predistortion method combines RLS and LMS algorithm," in *2009 4th IEEE Conference on Industrial Electronics and Applications*, May 2009, pp. 3900–3903.
- [59] E. Moore, "On the reciprocal of the general algebraic matrix," *Bulletin of American Mathematical Society*, vol. 26, pp. 394–395, 1920.
- [60] R. Penrose, "A generalized inverse for matrices," *Mathematical Proceedings of the Cambridge Philosophical Society*, vol. 51, no. 3, p. 406–413, 1955.
- [61] J. Stoer, R. Bartels, W. Gautschi, R. Bulirsch, and C. Witzgall, *Introduction to Numerical Analysis*, ser. Texts in Applied Mathematics. Springer New York, 2013. [Online]. Available: <https://books.google.ie/books?id=YJPkBwAAQBAJ>

References

- [62] M. Isaksson, D. Wisell, and D. Ronnow, “A comparative analysis of behavioral models for RF power amplifiers,” *IEEE Transactions on Microwave Theory and Techniques*, vol. 54, no. 1, pp. 348–359, Jan 2006.
- [63] Changsoo Eun and E. J. Powers, “A new Volterra predistorter based on the indirect learning architecture,” *IEEE Transactions on Signal Processing*, vol. 45, no. 1, pp. 223–227, Jan 1997.
- [64] Lei Ding, G. T. Zhou, D. R. Morgan, Zhengxiang Ma, J. S. Kenney, Jaehyeong Kim, and C. R. Giardina, “A robust digital baseband predistorter constructed using memory polynomials,” *IEEE Transactions on Communications*, vol. 52, no. 1, pp. 159–165, Jan 2004.
- [65] A. Zhu, P. J. Draxler, J. J. Yan, T. J. Brazil, D. F. Kimball, and P. M. Asbeck, “Open-loop digital predistorter for RF power amplifiers using dynamic deviation reduction-based Volterra series,” *IEEE Transactions on Microwave Theory and Techniques*, vol. 56, no. 7, pp. 1524–1534, July 2008.
- [66] C. Yu, L. Guan, E. Zhu, and A. Zhu, “Band-limited volterra series-based digital predistortion for wideband RF power amplifiers,” *IEEE Transactions on Microwave Theory and Techniques*, vol. 60, no. 12, pp. 4198–4208, Dec 2012.
- [67] D. Zhou and V. E. DeBrunner, “Novel adaptive nonlinear predistorters based on the direct learning algorithm,” *IEEE Transactions on Signal Processing*, vol. 55, no. 1, pp. 120–133, Jan 2007.
- [68] P. L. Gilabert, G. Montoro, D. López, N. Bartzoudis, E. Bertran, M. Payaró, and A. Hourtane, “Order reduction of wideband digital predistorters using principal component analysis,” in *2013 IEEE MTT-S International Microwave Symposium Digest (MTT)*, June 2013, pp. 1–7.
- [69] L. Ding, F. Mujica, and Z. Yang, “Digital predistortion using direct learning with reduced bandwidth feedback,” in *2013 IEEE MTT-S International Microwave Symposium Digest (MTT)*, June 2013, pp. 1–3.
- [70] R. N. Braithwaite, “A comparison of indirect learning and closed loop estimators used in digital predistortion of power amplifiers,” in *2015 IEEE MTT-S International Microwave Symposium*, May 2015, pp. 1–4.
- [71] S. Amin, E. Zenteno, P. N. Landin, D. Rönnow, M. Isaksson, and P. Händel, “Noise impact on the identification of digital predistorter parameters in the indirect learning architecture,” in *2012 Swedish Communication Technologies Workshop (Swe-CTW)*, Oct 2012, pp. 36–39.
- [72] P. N. Landin, A. E. Mayer, and T. Eriksson, “Mila - a noise mitigation technique for rf power amplifier linearization,” in *2014 IEEE 11th International Multi-Conference on Systems, Signals Devices (SSD14)*, Feb 2014, pp. 1–4.
- [73] J. Chani-Cahuana, C. Fager, and T. Eriksson, “A new variant of the indirect learning architecture for the linearization of power amplifiers,” in *2015 10th European Microwave Integrated Circuits Conference (EuMIC)*, Sep. 2015, pp. 444–447.

-
- [74] T. L. Marzetta, “Noncooperative cellular wireless with unlimited numbers of base station antennas,” *IEEE Transactions on Wireless Communications*, vol. 9, no. 11, pp. 3590–3600, November 2010.
- [75] E. Björnson, E. G. Larsson, and T. L. Marzetta, “Massive mimo: ten myths and one critical question,” *IEEE Communications Magazine*, vol. 54, no. 2, pp. 114–123, February 2016.
- [76] J. Flordelis, F. Rusek, F. Tufvesson, E. G. Larsson, and O. Edfors, “Massive mimo performance—tdd versus fdd: What do measurements say?” *IEEE Transactions on Wireless Communications*, vol. 17, no. 4, pp. 2247–2261, April 2018.
- [77] S. A. Bassam, M. Helaoui, and F. M. Ghannouchi, “Crossover digital predistorter for the compensation of crosstalk and nonlinearity in mimo transmitters,” *IEEE Transactions on Microwave Theory and Techniques*, vol. 57, no. 5, pp. 1119–1128, May 2009.
- [78] D. Saffar, N. Boulejfen, F. M. Ghannouchi, A. Gharsallah, and M. Helaoui, “Behavioral modeling of mimo nonlinear systems with multivariable polynomials,” *IEEE Transactions on Microwave Theory and Techniques*, vol. 59, no. 11, pp. 2994–3003, Nov 2011.
- [79] B. Razavi, T. Aytur, C. Lam, Fei-Ran Yang, Kuang-Yu Li, Ran-Hong Yan, Han-Chang Kang, Cheng-Chung Hsu, and Chao-Cheng Lee, “A uwb cmos transceiver,” *IEEE Journal of Solid-State Circuits*, vol. 40, no. 12, pp. 2555–2562, Dec 2005.
- [80] J. Qi and S. Aissa, “Analysis and compensation of power amplifier nonlinearity in mimo transmit diversity systems,” *IEEE Transactions on Vehicular Technology*, vol. 59, no. 6, pp. 2921–2931, July 2010.
- [81] M. Romier, A. Barka, H. Aubert, J. . Martinaud, and M. Soiron, “Load-pull effect on radiation characteristics of active antennas,” *IEEE Antennas and Wireless Propagation Letters*, vol. 7, pp. 550–552, 2008.
- [82] S. Lee, M. Kim, Y. Sirl, E. Jeong, S. Hong, S. Kim, and Y. H. Lee, “Digital predistortion for power amplifiers in hybrid MIMO systems with antenna subarrays,” in *Proc. IEEE 81st Veh Technol. Conf. (VTC Spring)*, May 2015, pp. 1–5.
- [83] X. Liu, Q. Zhang, W. Chen, H. Feng, L. Chen, F. M. Ghannouchi, and Z. Feng, “Beam-oriented digital predistortion for 5G massive MIMO hybrid beamforming transmitters,” *IEEE Trans. Microw. Theory Techn.*, vol. 66, no. 7, pp. 3419–3432, July 2018.
- [84] A. Prata, J. Sveshtarov, S. C. Pires, A. S. R. Oliveira, and N. B. Carvalho, “Optimized DPD feedback loop for m-MIMO sub-6GHz systems,” in *Proc. IEEE/MTT-S Int. Microw. Symp. (IMS)*, June 2018, pp. 485–488.

References

- [85] X. Liu, W. Chen, L. Chen, and Z. Feng, “Beam-oriented digital predistortion for hybrid beamforming array utilizing over-the-air diversity feedbacks,” in *2019 IEEE MTT-S International Microwave Symposium (IMS)*, June 2019, pp. 987–990.
- [86] E. Ng, Y. Beltagy, P. Mitran, and S. Boumaiza, “Single-input single-output digital predistortion of power amplifier arrays in millimeter wave RF beamforming transmitters,” in *Proc. IEEE/MTT-S Int. Microw. Symp. (IMS)*, June 2018, pp. 481–484.
- [87] E. Ng, Y. Beltagy, G. Scarlato, A. B. Ayed, P. Mitran, and S. Boumaiza, “Digital predistortion of millimeter-wave rf beamforming arrays using low number of steering angle-dependent coefficient sets,” *IEEE Trans. Microw. Theory Techn.*, pp. 1–14, July 2019.
- [88] S. Hesami, S. R. Aghdam, C. Fager, T. Eriksson, R. Farrell, and J. Dooley, “Single digital predistortion technique for phased array linearization,” in *2019 IEEE International Symposium on Circuits and Systems (ISCAS)*, May 2019, pp. 1–5.
- [89] K. Hausmair, U. Gustavsson, C. Fager, and T. Eriksson, “Modeling and linearization of multi-antenna transmitters using over-the-air measurements,” in *2018 IEEE International Symposium on Circuits and Systems (ISCAS)*, May 2018, pp. 1–4.
- [90] S. Lee, M. Kim, Y. Sirl, E. Jeong, S. Hong, S. Kim, and Y. H. Lee, “Digital predistortion for power amplifiers in hybrid MIMO systems with antenna subarrays,” in *IEEE 81st Vehicular Technology Conference (VTC Spring)*, May 2015, pp. 1–5.
- [91] W. Chen, G. Lv, X. Liu, and Z. Feng, “Energy-efficient doherty power amplifier MMIC and beamforming-oriented digital predistortion for 5G massive MIMO application,” in *2017 IEEE Asia Pacific Microwave Conference (APMC)*, Nov 2017, pp. 391–394.
- [92] N. Tervo, J. Aikio, T. Tuovinen, T. Rahkonen, and A. Parssinen, “Digital predistortion of amplitude varying phased array utilising over-the-air combining,” in *IEEE MTT-S Int. Microwave Symposium (IMS)*, Jun 2017, pp. 1165–1168.
- [93] M. Abdelaziz, L. Anttila, A. Brihuega, F. Tufvesson, and M. Valkama, “Digital predistortion for hybrid MIMO transmitters,” *IEEE J. Sel. Topics Signal Process.*, vol. 12, no. 3, pp. 445–454, Jun 2018.
- [94] X. Liu, Q. Zhang, W. Chen, H. Feng, L. Chen, F. M. Ghannouchi, and Z. Feng, “Beam-oriented digital predistortion for 5G massive MIMO hybrid beamforming transmitters,” *IEEE Trans. Microw. Theory Techn.*, vol. 66, no. 7, pp. 3419–3432, Jul 2018.
- [95] K. Hausmair, S. Gustafsson, C. Sánchez-Pérez, P. N. Landin, U. Gustavsson, T. Eriksson, and C. Fager, “Prediction of nonlinear distortion in wideband active antenna arrays,” *IEEE Trans. Microw. Theory Techn.*, vol. 65, no. 11, pp. 4550–4563, Nov 2017.

-
- [96] H. Zargar, A. Banai, and J. C. Pedro, “A new double input-double output complex envelope amplifier behavioral model taking into account source and load mismatch effects,” *IEEE Transactions on Microwave Theory and Techniques*, vol. 63, no. 2, pp. 766–774, Feb 2015.
- [97] C. Fager, X. Bland, K. Hausmair, J. C. Cahuana, and T. Eriksson, “Prediction of smart antenna transmitter characteristics using a new behavioral modeling approach,” in *Proc. IEEE/MTT-S Int. Microw. Symp. (IMS)*, June 2014, pp. 1–4.
- [98] M. Schetzen, *The Volterra and Wiener Theories of Nonlinear Systems*. Melbourne, FL, USA: Krieger Publishing Co., Inc., 2006.
- [99] K. Hausmair, P. N. Landin, U. Gustavsson, C. Fager, and T. Eriksson, “Digital predistortion for multi-antenna transmitters affected by antenna crosstalk,” *IEEE Trans. Microw. Theory Techn.*, vol. 66, no. 3, pp. 1524–1535, Mar 2018.
- [100] J. Kim and K. Konstantinou, “Digital predistortion of wideband signals based on power amplifier model with memory,” *Electron. Lett.*, vol. 37, no. 23, pp. 1417–1418, Nov 2001.
- [101] G. Z. El Nashef, F. Torrès, S. Mons, T. Reveyrand, T. Monédière, E. N’Goya, and R. Quéré, “Second order extension of power amplifiers behavioral models for accuracy improvements,” in *Proc. Eur. Microw. Conf. (EuMC)*, Sep. 2010, pp. 1030–1033.
- [102] M. Joham, W. Utschick, and J. A. Nossek, “Linear transmit processing in mimo communications systems,” *IEEE Transactions on Signal Processing*, vol. 53, no. 8, pp. 2700–2712, Aug 2005.
- [103] F. Rusek, D. Persson, B. K. Lau, E. G. Larsson, T. L. Marzetta, O. Edfors, and F. Tufvesson, “Scaling up mimo: Opportunities and challenges with very large arrays,” *IEEE Signal Processing Magazine*, vol. 30, no. 1, pp. 40–60, Jan 2013.
- [104] H. Q. Ngo, E. G. Larsson, and T. L. Marzetta, “Energy and spectral efficiency of very large multiuser mimo systems,” *IEEE Transactions on Communications*, vol. 61, no. 4, pp. 1436–1449, April 2013.
- [105] S. Hesami, J. Dooley, Ziming, Wang, and R. Farrell, “Digital predistorter in crosstalk compensation of mimo transmitters,” in *2016 27th Irish Signals and Systems Conference (ISSC)*, 2016, pp. 1–5.
- [106] T. Oh and R. Harjani, “A 6-gb/s mimo crosstalk cancellation scheme for high-speed i/os,” *IEEE Journal of Solid-State Circuits*, vol. 46, no. 8, pp. 1843–1856, Aug 2011.
- [107] S. Amin, P. N. Landin, P. Händel, and D. Rönnow, “Behavioral modeling and linearization of crosstalk and memory effects in rf mimo transmitters,” *IEEE Transactions on Microwave Theory and Techniques*, vol. 62, no. 4, pp. 810–823, April 2014.

References

- [108] Y. Liu, W. Chen, J. Zhou, B. Zhou, and F. M. Ghannouchi, “Digital pre-distortion for concurrent dual-band transmitters using 2-d modified memory polynomials,” *IEEE Transactions on Microwave Theory and Techniques*, vol. 61, no. 1, pp. 281–290, Jan 2013.
- [109] H. Paaso and A. Mammela, “Comparison of direct learning and indirect learning predistortion architectures,” in *2008 IEEE International Symposium on Wireless Communication Systems*, Oct 2008, pp. 309–313.
- [110] Proakis, *Digital Communications 5th Edition*. McGraw Hill, 2007.
- [111] S. Hesami, S. R. Aghdam, C. Fager, T. Eriksson, R. Farrell, and J. Dooley, “Intra-array coupling estimation for MIMO transceivers utilizing blind over-the-air measurements,” in *Proc. IEEE/MTT-S Int. Microw. Symp. (IMS)*, June 2019, pp. 468–471.
- [112] F. M. Barradas, P. M. Tomé, J. M. Gomes, T. R. Cunha, P. M. Cabral, and J. C. Pedro, “Power, linearity, and efficiency prediction for mimo arrays with antenna coupling,” *IEEE Transactions on Microwave Theory and Techniques*, vol. 65, no. 12, pp. 5284–5297, Dec 2017.
- [113] J. Wood, “System-level design considerations for digital pre-distortion of wireless base station transmitters,” *IEEE Trans. Microw. Theory Techn.*, vol. 65, no. 5, pp. 1880–1890, May 2017.
- [114] J. Vieira, F. Rusek, O. Edfors, S. Malkowsky, L. Liu, and F. Tufvesson, “Reciprocity calibration for massive MIMO: Proposal, modeling, and validation,” *IEEE Trans. on Wireless Commun.*, vol. 16, no. 5, pp. 3042–3056, May 2017.
- [115] Q. Gu, *RF System Design of Transceivers for Wireless Communications*, 1st ed. Springer Publishing Company, Incorporated, 2010.
- [116] A. Hjørungnes and D. Gesbert, “Complex-valued matrix differentiation: Techniques and key results,” *IEEE Trans. Signal Process.*, vol. 55, no. 6, pp. 2740–2746, June 2007.
- [117] L. M. Correia, D. Zeller, O. Blume, D. Ferling, Y. Jading, I. Gódor, G. Auer, and L. V. Der Perre, “Challenges and enabling technologies for energy aware mobile radio networks,” *IEEE Commun. Mag.*, vol. 48, no. 11, pp. 66–72, November 2010.
- [118] S. Hesami, P. Ramabadran and S. Rezaei Aghdam, K. Hausmair, C. Fager, T. Eriksson, R. Farrell, and J. Dooley, “Ota-based mimo transceiver modeling and linearization using effective coupling estimation,” *Submitted to IEEE Transactions on Microwave Theory and Techniques*, 2020.
- [119] E. Björnson, E. G. Larsson, and T. L. Marzetta, “Massive mimo: ten myths and one critical question,” *IEEE Commun. Mag.*, vol. 54, no. 2, pp. 114–123, Feb 2016.
- [120] S. Choi and E. Jeong, “Digital predistortion based on combined feedback in MIMO transmitters,” *IEEE Commun. Lett.*, vol. 16, no. 10, pp. 1572–1575, Oct 2012.

-
- [121] P. N. Landin, A. E. Mayer, and T. Eriksson, “MILA - A noise mitigation technique for rf power amplifier linearization,” in *Proc. IEEE 11th Int. Multi-Conf. on Systems, Signals Devices (SSD14)*, February 2014, pp. 1–4.
- [122] M. Isaksson, D. Wisell, and D. Ronnow, “A comparative analysis of behavioral models for RF power amplifiers,” *IEEE Trans. Microw. Theory Techn.*, vol. 54, no. 1, pp. 348–359, Jan 2006.
- [123] S. Hesami, S. Rezaei Aghdam, J. Dooley, T. Eriksson, and C. Fager, “Amplitude varying phased array linearization,” in *2020 50th European Microwave Conference (EuMC)*, Jul 2020.
- [124] L. Ding, G. T. Zhou, D. R. Morgan, Z. Ma, J. S. Kenney, J. Kim, and C. R. Giardina, “A robust digital baseband predistorter constructed using memory polynomials,” *IEEE Trans. Commun. Technol.*, vol. 52, no. 1, pp. 159–165, Jan 2004.
- [125] A. S. Tehrani, H. Cao, S. Afsardoost, T. Eriksson, M. Isaksson, and C. Fager, “A comparative analysis of the complexity/accuracy tradeoff in power amplifier behavioral models,” *IEEE Trans. Microw. Theory Techn.*, vol. 58, no. 6, pp. 1510–1520, Jun 2010.
- [126] R. N. Braithwaite, “A comparison of indirect learning and closed loop estimators used in digital predistortion of power amplifiers,” in *2015 IEEE MTT-S International Microwave Symposium*, May 2015, pp. 1–4.
- [127] C. Mollen, E. G. Larsson, U. Gustavsson, T. Eriksson, and R. W. Heath, “Out-of-band radiation from large antenna arrays,” *IEEE Commun. Mag.*, vol. 56, no. 4, pp. 196–203, Apr 2018.
- [128] N. D. Sidiropoulos, T. N. Davidson, and Z.-Q. Luo, “Transmit beamforming for physical-layer multicasting,” *IEEE Trans. Signal Process.*, vol. 54, no. 6, pp. 2239–2251, Jun 2006.
- [129] M. Grant and S. Boyd, “CVX: Matlab software for disciplined convex programming, version 2.1,” <http://cvxr.com/cvx>, Mar. 2014.
- [130] —, “Graph implementations for nonsmooth convex programs,” in *Recent Advances in Learning and Control*, ser. Lecture Notes in Control and Information Sciences, V. Blondel, S. Boyd, and H. Kimura, Eds. Springer-Verlag Limited, 2008, pp. 95–110, http://stanford.edu/~boyd/graph_dcp.html.